

# Chemical equilibrium in AGB atmospheres: Successes, failures, and prospects for small molecules, clusters, and condensates

M. Agúndez<sup>1</sup>, J. I. Martínez<sup>2</sup>, P. L. de Andres<sup>2</sup>, J. Cernicharo<sup>1</sup>, and J. A. Martín-Gago<sup>2</sup>

<sup>1</sup> Instituto de Física Fundamental, CSIC, C/ Serrano 123, 28006 Madrid, Spain

<sup>2</sup> Instituto de Ciencia de Materiales de Madrid, CSIC, C/ Sor Juana Inés de la Cruz 3, 28049 Cantoblanco, Spain

Received; accepted

## ABSTRACT

Chemical equilibrium has proven extremely useful for predicting the chemical composition of AGB atmospheres. Here we use a recently developed code and an updated thermochemical database that includes gaseous and condensed species involving 34 elements to compute the chemical equilibrium composition of AGB atmospheres of M-, S-, and C-type stars. We include for the first time  $Ti_xC_y$  clusters, with  $x = 1-4$  and  $y = 1-4$ , and selected larger clusters ranging up to  $Ti_{13}C_{22}$ , for which thermochemical data are obtained from quantum-chemical calculations. Our main aims are to systematically survey the main reservoirs of each element in AGB atmospheres, review the successes and failures of chemical equilibrium by comparing it with the latest observational data, identify potentially detectable molecules that have not yet been observed, and diagnose the most likely gas-phase precursors of dust and determine which clusters might act as building blocks of dust grains. We find that in general, chemical equilibrium reproduces the observed abundances of parent molecules in circumstellar envelopes of AGB stars well. There are, however, severe discrepancies of several orders of magnitude for some parent molecules that are observed to be anomalously overabundant with respect to the predictions of chemical equilibrium. These are HCN, CS,  $NH_3$ , and  $SO_2$  in M-type stars,  $H_2O$  and  $NH_3$  in S-type stars, and the hydrides  $H_2O$ ,  $NH_3$ ,  $SiH_4$ , and  $PH_3$  in C-type stars. Several molecules have not yet been observed in AGB atmospheres but are predicted with non-negligible abundances and are good candidates for detection with observatories such as ALMA. The most interesting ones are  $SiC_5$ ,  $SiNH$ ,  $SiCl$ , PS, HBO, and the metal-containing molecules MgS, CaS, CaOH, CaCl, CaF, ScO, ZrO, VO, FeS, CoH, and NiS. In agreement with previous studies, the first condensates predicted to appear in C-rich atmospheres are found to be carbon, TiC, and SiC, while  $Al_2O_3$  is the first major condensate expected in O-rich outflows. According to our chemical equilibrium calculations, the gas-phase precursors of carbon dust are probably acetylene, atomic carbon, and/or  $C_3$ , while for silicon carbide dust, the most likely precursors are the molecules  $SiC_2$  and  $Si_2C$ . In the case of titanium carbide dust, atomic Ti is the major reservoir of this element in the inner regions of AGB atmospheres, and therefore it is probably the main supplier of titanium during the formation of TiC dust. However, chemical equilibrium predicts that large titanium-carbon clusters such as  $Ti_8C_{12}$  and  $Ti_{13}C_{22}$  become the major reservoirs of titanium at the expense of atomic Ti in the region where condensation of TiC is expected to occur. This suggests that the assembly of large  $Ti_xC_y$  clusters might be related to the formation of the first condensation nuclei of TiC. In the case of  $Al_2O_3$  dust, chemical equilibrium indicates that atomic Al and the carriers of Al-O bonds AlOH, AlO, and  $Al_2O$  are the most likely gas-phase precursors.

**Key words.** astrochemistry – molecular data – stars: AGB and post-AGB – stars: atmospheres – stars: circumstellar matter

## 1. Introduction

During their late evolutionary stages, low- and intermediate-mass stars ( $< 8 M_\odot$ ) become red giants, increasing their radius by 2-3 orders of magnitude and decreasing their surface temperature to 2000-3000 K. At these temperatures, the material is essentially molecular. When these stars enter the so-called asymptotic giant branch (AGB) phase, they start to lose mass through nearly isotropic winds that give rise to circumstellar envelopes that are mainly composed of gaseous molecules and dust grains (Höfner & Olofsson 2018).

Thermochemical equilibrium provides a simple but incredibly useful starting point to describe the chemical composition of matter in the atmospheres of AGB stars. For example, chemical equilibrium has provided an elegant explanation of the marked chemical differentiation between oxygen-rich and carbon-rich AGB stars based on the high bond energy of carbon monoxide (Russell 1934). The high abundance of CO causes it to trap most of the limiting element and allows the element in excess to form either oxygen-bearing molecules when  $C/O < 1$  or carbon-bearing molecules when  $C/O > 1$ . Moreover, the discovery of

many molecules in envelopes around evolved stars, such as HCP, PO, AlOH, or TiO (Agúndez et al. 2007; Tenenbaum et al. 2007; Tenenbaum & Ziurys 2010; Kamiński et al. 2013), has largely been inspired by the predictions of chemical equilibrium calculations such as those of Tsuji (1964, 1973). During the past decades, however, observations have shown a significant number of discrepancies with the scenario depicted by chemical equilibrium such as the discovery of warm water vapor in carbon stars (Decin et al. 2010), which indicate that nonequilibrium processes are at work in AGB atmospheres.

Chemical equilibrium is also very useful for studying the types of dust that are formed in AGB ejecta. We know that AGB stars are the main sources of dust in the Galaxy (Gehrz 1989), but identifying the chemical nature of the dust is difficult. Only a handful of solid materials have been identified so far in circumstellar envelopes of AGB stars (e.g., Waters 2011), while some information is also available from the analysis of presolar material in meteorites (Lodders & Amari 2005). Chemical equilibrium can provide the basic theoretical scenario with the types of condensates that are thermodynamically favored and their condensation temperatures, which determine the sequence in which

they are expected to appear as matter flows from the AGB star and cools (Sharp et al. 1995; Lodders & Fegley 1997, 1999; Gail & Sedlmayr 2013).

Although the formation of dust in AGB outflows is a complex process that is likely governed by chemical kinetics, as indicated by the extensive theoretical work of Gail & Sedlmayr (see, e.g., Gail & Sedlmayr 2013), chemical equilibrium can provide clues on the sequence of clustering that initiates the formation of the first solid materials from a gas of atoms and small molecules. The identification of the most thermodynamically favored intermediate clusters is an important piece of information. Several works have studied from the point of view of chemical equilibrium the clustering process that initiates the formation of some of the condensates that are predicted to appear earlier in AGB winds, such as MgO (Köhler et al. 1997), SiC (Yasuda & Kozasa 2012; Gobrecht et al. 2017), silicates (Goumans & Bromley 2012, 2013), and Al<sub>2</sub>O<sub>3</sub> (Álvarez-Barcia & Flores 2016; Gobrecht et al. 2016; Boulanger et al. 2019). Today, the unprecedented angular resolution and sensitivity of observatories such as ALMA have the potential of identifying the building blocks of dust in the atmospheres of AGB stars, providing constraints on the clustering process based on their abundances and spatial distributions (see, e.g., Kamiński et al. 2017; Decin et al. 2017; McCarthy et al. 2019).

In this study, we revisit thermochemical equilibrium in AGB atmospheres with different C-to-O ratios (M, S, and C stars) using the latest thermochemical data to compare the predictions of chemical equilibrium with the current observational situation. Our main motivations are threefold. (1) We review the successes of chemical equilibrium in explaining the observed abundances of parent molecules in AGB envelopes and identify the main failures, all of which must be accounted for by any nonequilibrium scenario that is proposed for the atmospheres of AGB stars. (2) We identify potentially detectable molecules that have not yet been observed in AGB atmospheres. (3) We compute the condensation sequence of solid materials in the atmospheres of M, S, and C stars and evaluate the most likely gas-phase precursors of different condensates. We also determine which thermodynamically favorable clusters<sup>1</sup> might play a role as intermediate species in the clustering process. In particular, we have computed thermochemical properties for various Ti<sub>x</sub>C<sub>y</sub> clusters to evaluate their abundances and role in the formation of titanium carbide dust in the atmospheres of C-type stars.

## 2. Thermochemical equilibrium calculations

### 2.1. Method of computation

The composition of a mixture of gases and condensates at thermochemical equilibrium is determined by the minimization of the Gibbs free energy of the system, and it only depends on three input parameters: pressure, temperature, and relative abundances of the elements. The calculations need to be fed with thermochemical data of the included species. Many programs based on different algorithms have been developed to compute chemical equilibrium in the atmospheres of cool stars, brown dwarfs, and planets. We can distinguish between two groups of methods: those based on equilibrium constants, and those that minimize the total Gibbs free energy of the system.

In the first group, the mathematical problem consists of a set of equations of conservation of each element, in which the partial pressure of each molecule is expressed in terms of the partial

pressures of the constituent atoms by the equilibrium constant of atomization. In a first step, the system is solved only for the most abundant elements, and then the whole system including all trace elements is solved iteratively using the Newton-Raphson method or similar methods. The Newton-Raphson method, originally developed by Russell (1934) for diatomic molecules and generalized by Brinkley (1947), was later applied by Tsuji (1973) to atmospheres of cool stars. The method has been implemented with different refinements by Tejero & Cernicharo (1991) and by codes such as CONDOR (Lodders & Fegley 1993), GGChem (Woitke et al. 2018), and FastChem (Stock et al. 2018).

The second type of methods was introduced by White et al. (1958) and solves the problem of minimizing the total Gibbs energy of a mixture of species subject to the conservation of each element. This method is more general in that it makes no distinction between atoms, molecules, and condensates because all them are simply constituent species of the mixture. The method is widely used by different programs, for instance, by SOLGAS (Eriksson 1971), NASA/CEA (Gordon & McBride 1994), and more recently, TEA (Blecic et al. 2016).

Zelevnik & Gordon (1960) demonstrated that the methods of equilibrium constants and Gibbs minimization are computationally identical, and therefore the various existing programs are expected to converge to the same equilibrium composition regardless of the method used. Important differences can appear, however, when the included species are not the same or when the adopted thermochemical data are different. The precision of chemical equilibrium calculations is essentially limited by the completeness of the included species and by the availability of accurate thermochemical data.

Our chemical equilibrium code uses the Gibbs minimization method and is based on the algorithm implemented in the NASA/CEA program (Gordon & McBride 1994). The code has been developed in recent years and has been applied to describe the chemical composition of hot-Jupiter atmospheres by Agúndez et al. (2014a).

### 2.2. Thermochemical data

To solve chemical equilibrium by minimizing the Gibbs free energy of a system, the basic thermodynamic quantity needed is the free energy of each species as a function of temperature  $g^0(T)$ . This quantity, also known as standard-state chemical potential, can be expressed as

$$g^0(T) = H^0(T) - TS^0(T), \quad (1)$$

where  $H^0(T)$  and  $S^0(T)$  are the standard-state enthalpy and entropy, respectively, of the species, and standard-state refers to a standard pressure of 1 bar. These thermochemical properties are either given directly in compilations such as NIST-JANAF (Chase 1998)<sup>2</sup> or are found parameterized as a function of temperature through NASA polynomial coefficients (see, e.g., McBride et al. 2002) in databases such as NASA/CEA (McBride et al. 2002)<sup>3</sup> or the Third Millennium Thermochemical Database (Goos, Burcat, & Ruscic)<sup>4</sup>.

We here considered 919 gaseous species and 185 condensed species involving up to 34 elements. Thermochemical data were mostly taken from the library of NASA/CEA (McBride et al. 2002) and from the Third Millennium Thermochemical Database (Goos, Burcat, & Ruscic). The NASA/CEA data are mostly

<sup>2</sup> <https://janaf.nist.gov/>

<sup>3</sup> See <https://www.grc.nasa.gov/WWW/CEAWeb>

<sup>4</sup> <https://burcat.technion.ac.il/>

<sup>1</sup> In this work we use the term cluster to refer to large molecules, mostly large Ti<sub>x</sub>C<sub>y</sub> and Si<sub>x</sub>C<sub>y</sub> molecules.

based on the work carried out at the NASA Glenn Research Center until 2002 and in classical compilations such as Gurvich et al. (1989) and NIST-JANAF (Chase 1998). The Third Millennium Thermochemical Database includes data from the NASA/CEA compilation, although it is larger and is continuously updated with data from dedicated ab initio calculations, the Active Thermochemical Tables (Ruscic et al. 2014), and from the recent literature. We note that the  $\text{FeCl}_3$  data in the NASA/CEA library are incorrect because a formation enthalpy of  $-1059 \text{ kJ mol}^{-1}$  is assumed, while the value reported in the literature (e.g., NIST-JANAF; Chase 1998) is  $-253 \text{ kJ mol}^{-1}$ . The use of the incorrect data results in an overestimation of the  $\text{FeCl}_3$  abundance, with important implications for the overall chlorine budget. For this species we therefore adopted the data from the Third Millennium Thermochemical Database.

In addition to these two large compilations, the NASA/CEA and Third Millennium Thermochemical Database, we also used thermochemical data from different literature sources either because the species was not included in the other two compilations or because more accurate data were available. For several molecules involving Li, Na, Mg, Ti, Fe, and Co, we took the data directly from the NIST-JANAF Thermochemical Tables (Chase 1998) because they are not included in the NASA/CEA library or in the Third Millennium Thermochemical Database. For  $\text{PH}_3$ ,  $\text{PH}$ ,  $\text{PN}$ ,  $\text{SH}$ ,  $\text{S}_2\text{O}$ ,  $\text{NS}$ , and  $\text{PS}$ , we adopted the thermochemical data revised by Lodders (1999, 2004). We also included some metal-containing diatomic molecules with thermochemical data from Barklem & Collet (2016), while for  $\text{V}_2\text{O}_4$ , we used data from Balducci et al. (1983). Thermochemical data for the two silicon-containing molecules  $\text{SiCH}$  and  $\text{SiNH}$  were taken from the Chemkin Thermodynamic Database (Kee et al. 2000). Data for  $\text{Si}_x\text{C}_y$  clusters were taken from Deng et al. (2008), while the thermochemical properties of  $\text{Ti}_x\text{C}_y$  clusters were calculated in this work and are described in detail in Appendix B. Concretely, we include all  $\text{Ti}_x\text{C}_y$  clusters with  $x = 1-4$  and  $y = 1-4$  and the large stable clusters  $\text{Ti}_3\text{C}_8$ ,  $\text{Ti}_4\text{C}_8$ ,  $\text{Ti}_6\text{C}_{13}$ ,  $\text{Ti}_7\text{C}_{13}$ ,  $\text{Ti}_8\text{C}_{12}$ ,  $\text{Ti}_9\text{C}_{15}$ , and  $\text{Ti}_{13}\text{C}_{22}$ . For the condensates  $\text{CaTiO}_3$ ,  $\text{NaAlSi}_3\text{O}_8$ ,  $\text{KAlSi}_3\text{O}_8$ ,  $\text{Fe}_3\text{C}$ ,  $\text{CaMgSi}_2\text{O}_6$ ,  $\text{CaAl}_2\text{Si}_2\text{O}_8$ , and  $\text{Ca}_2\text{Al}_2\text{SiO}_7$  we used thermochemical data from Robie et al. (1979), while for  $\text{CaAl}_4\text{O}_7$  and  $\text{CaAl}_{12}\text{O}_{19}$ , data were taken from Allibert et al. (1981) and Geiger et al. (1988).

### 2.3. Elemental composition

Optical and infrared observations of AGB stars have found that the atmospheric elemental composition is nearly solar, with the exception of carbon and  $s$ -process elements, which are significantly enhanced in carbon stars because they are brought out to the surface by dredge-up processes. Determination of the abundances of C, N, and O in AGB stars indicates that these elements have essentially solar abundances, except for carbon, which in S- and C-type stars is enhanced, which results in C/O of  $\sim 1$  and  $> 1$ , respectively (Smith & Lambert 1985, 1986; Lambert et al. 1986). In our calculations we consider C/O of 0.54 (solar), 1.00, and 1.40 for M-, S-, and C-type stars, respectively. Elements produced through neutron capture in the  $s$ -process such as Sr, Zr, and Ba are found to have moderate abundance enhancements in carbon stars (Abia et al. 2002). Other elements for which significant deviations from the solar abundances are expected in AGB stars are fluorine and lithium. In the case of fluorine, however, recent observational studies find only mild enhancements and point to abundances very close to the solar value (Abia et al. 2015, 2019). Although a few super-rich lithium stars ( $\log \epsilon > 4$ ) exist, the abundance of lithium in Galactic carbon stars is found

**Table 1.** Thirty-four elements included and their abundances.

Element	$\log \epsilon^a$	Element	$\log \epsilon^a$	Element	$\log \epsilon^a$
H	12.00	Al	6.45	Mn	5.43
He	10.93	Si	7.51	Fe	7.50
Li	$-0.30^b$	P	5.41	Co	4.99
Be	1.38	S	7.12	Ni	6.22
B	2.70	Cl	5.50	Cu	4.19
C	$8.43^c$	Ar	6.40	Zn	4.56
N	7.83	K	5.03	Rb	$2.52^e$
O	8.69	Ca	6.34	Sr	$2.87^e$
F	$4.48^d$	Sc	3.15	Zr	$2.58^e$
Ne	7.93	Ti	4.95	Ba	$2.18^e$
Na	6.24	V	3.93		
Mg	7.60	Cr	5.64		

<sup>a</sup> Abundance defined as  $\log \epsilon(X) = 12 + \log(X/H)$ . Abundances are solar from Asplund et al. (2009) unless otherwise stated. <sup>b</sup> Abia et al. (1993). <sup>c</sup> The abundance of C in S-type and carbon stars is increased over the solar value to have C/O of 1.0 and 1.4, respectively. <sup>d</sup> Abia et al. (2015). <sup>e</sup> The abundances of the  $s$ -process elements Rb, Sr, Zr, and Ba are increased over the solar values by 0.36, 1.01, 0.88, and 0.89 dex, respectively, in S-type stars (Abia & Wallerstein 1998) and by 0.26, 0.46, 0.67, and 0.51 dex, respectively, in carbon stars (Abia et al. 2002).

to be below that in the Sun (Abia et al. 1993). The abundances adopted for the 34 elements we included in the chemical equilibrium calculations are given in Table 1.

### 2.4. Radial profiles of temperature and pressure

The winds associated with AGB stars cause them to have extended atmospheres, in which the gas cools and the density of particles drops as it moves away from the star. The temperatures and pressures in this extended atmosphere are critical for establishing the chemical equilibrium composition. For example, high temperatures favor an atomic composition, while low temperatures favor a molecular gas. It is therefore very important to have a realistic description of how the gas temperature and pressure vary with radius.

The situation becomes complicated by two facts. First, the atmospheres of AGB stars are not static, but are affected by dynamical processes that are ultimately driven by the pulsation of the star. Variability of the infrared flux has been observationally characterized for a long time, and it is interpreted as a consequence of the stellar pulsation, during which the size and effective temperature of the star experience important changes (Le Bertre 1988; Suh 2004). Second, the low gravity of AGB stars causes the extended atmosphere to be affected by convective processes that lead to asymmetric structures, hot spots, and high-density clumps. This complex morphology is predicted by 3D hydrodynamical simulations (Freitag et al. 2017) and is starting to be characterized in detail with high angular resolution observations at infrared and (sub-)millimeter wavelengths (e.g., Khouri et al. 2016; Vlemmings et al. 2017; Fonfría et al. 2019).

Despite the complications related to the variation with time and the complex morphology, we adopted for our chemical equilibrium calculations a simple scenario that is representative of a generic AGB star in which the atmosphere is spherically symmetric and temperature and pressure vary smoothly with radius. Effective temperatures of AGB stars are usually in the range 2000-3000 K (Bergeat et al. 2001). Here we adopt an effective temperature of 2500 K. The temperature gradient throughout the extended atmosphere can be usually well accounted for using a power law, that is,  $T(r) \propto r^{-\alpha}$ , with values of  $\alpha$  in the range 0.5-

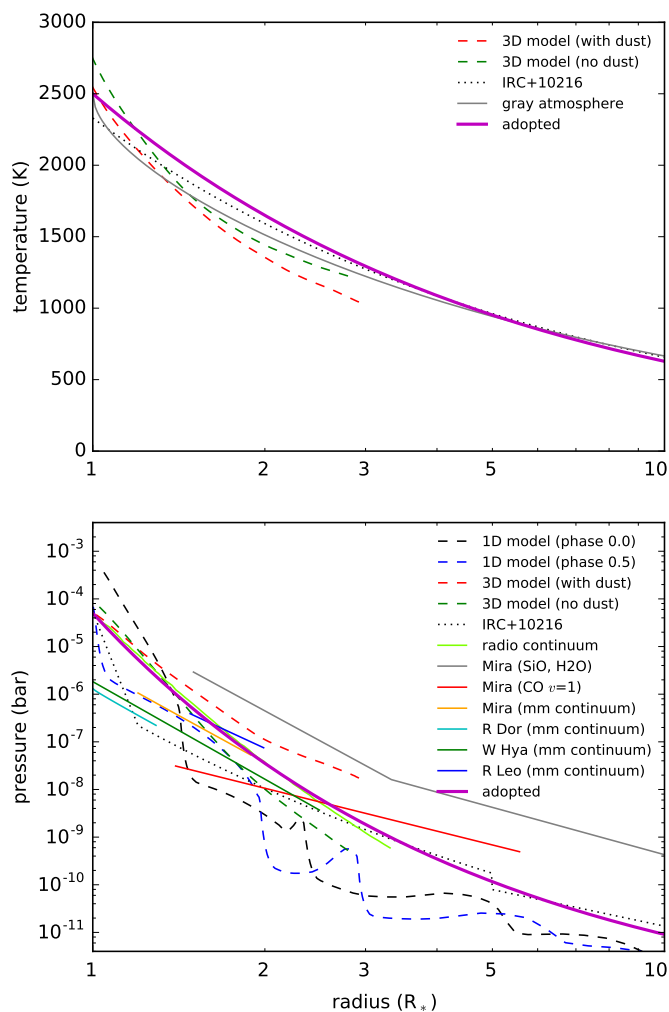


**Fig. 1.** Radial temperature (top panel) and pressure (bottom panel) profiles in the extended atmosphere of an AGB star. The black and blue dashed curves correspond to a 1D model of an AGB atmosphere at phases 0.0 and 0.5 (see Figure 1 of Bladh et al. 2019). The green and blue dashed curves show the profiles resulting from a 3D model of an AGB atmosphere with and without radiation pressure on dust (models st28gm06n06 and st28gm06n26 from Freytag et al. 2017, where profiles are averaged over spherical shells and time). The black dotted line shows the empirical profile derived for the carbon star IRC +10216 (Agúndez et al. 2012). In the bottom panel we also show as thin solid lines several radial pressure profiles derived from high angular resolution observations of the radio continuum of several AGB stars (Reid & Menten 1997), of Mira from ALMA observations of SiO and H<sub>2</sub>O (Wong et al. 2016) and of CO  $v = 1$  (Khouri et al. 2018), and of Mira, R Leo, W Hya, and R Dor from ALMA observations of the (sub)millimeter continuum (Vlemmings et al. 2019). The radial temperature and pressure profiles adopted in this study as representative of an AGB atmosphere are shown as thick magenta curves.

1.0. For example, a gray atmosphere, in which  $\alpha$  approaches 0.5 for  $r > R_*$ , has been adopted to model high angular resolution observations of continuum emission at radio and (sub)millimeter wavelengths (Reid & Menten 1997; Vlemmings et al. 2019). Several works have modeled molecular lines arising from the inner envelope around the carbon star IRC +10216, finding values of  $\alpha$  in the range 0.55-0.58 (Fonfría et al. 2008; De Beck et al. 2012; Agúndez et al. 2012). The 3D hydrodynamic models of Freytag et al. (2017) result in steeper radial temperature profiles close to the star, with a power-law index of 0.8-0.9 inside

$2 R_*$ , and more shallow in the  $2-3 R_*$  region. For our chemical equilibrium calculations, we adopted a power law for the radial temperature profile with an index of 0.6 (see the thick magenta line in the upper panel of Fig. 1), which results in a temperature profile similar to that derived for IRC +10216 and those resulting from 3D hydrodynamic models. In our adopted profile, the gas temperature decreases from 2500 K at the stellar surface down to  $\sim 630$  K at  $10 R_*$ .

The radial pressure profile is expected to be given by hydrostatic equilibrium at the stellar surface, while in the outer parts of the circumstellar envelope, where the gas has reached the terminal expansion velocity, mass conservation implies that the gas density varies with radius as a power law,  $n(r) \propto r^{-\beta}$ , with  $\beta = 2$ . The region in between these two parts, the extended atmosphere, is a complex environment where the gas is accelerated and the radial density profile is expected to be shallower than at hydrostatic equilibrium but steeper than the  $r^{-2}$  power law. In general, this behavior is supported by models and observations, although estimated densities can easily differ by several orders of magnitude in different studies. For example, hydrodynamic models that explain the formation of AGB winds through a combination of stellar pulsation plus radiation pressure on dust grains can provide estimates of the gas density in the extended atmosphere (Höfner & Olofsson 2018). These models can result in very different densities depending on the adopted parameters and the included processes, however. For example, we compare in the lower panel of Fig. 1 the various dashed curves, which correspond to a 1D model by Bladh et al. (2019) at two different phases and to two 3D models from Freytag et al. (2017). High angular resolution observations from radio to infrared wavelengths can provide constraints on the densities in the extended atmosphere of AGB stars (see the thin solid curves in the lower panel of Fig. 1). Infrared observations of R Dor, W Hya, and IK Tau indicate  $\beta$  values between 2.7 and 4.5 in regions that extend to a few stellar radii (Khouri et al. 2016; Ohnaka et al. 2017; Adam & Ohnaka 2019). From ALMA (sub)millimeter continuum observations of the low-mass loss-rate objects Mira (*o* Cet), R Dor, W Hya, and R Leo, Vlemmings et al. (2019) derived values of  $\beta$  in the range 5-6 for the  $1-3 R_*$  region. An even steeper radial density profile is obtained for the same  $1-3 R_*$  region from high angular resolution observations of radio continuum emission from various AGB stars (Reid & Menten 1997) and from 3D hydrodynamic models (Freytag et al. 2017).

As an illustration of the differences found in the literature, we show in the lower panel of Fig. 1 three radial density profiles derived from ALMA data of the star Mira, using SiO and H<sub>2</sub>O (Wong et al. 2016), CO  $v = 1$   $J = 3-2$  (Khouri et al. 2018), and (sub)millimeter continuum (Vlemmings et al. 2019). Although the derived slopes are similar, the absolute densities differ by as much as two orders of magnitude. The most striking feature is that when SiO and H<sub>2</sub>O data are used, the densities needed to properly excite the observed lines are significantly higher than those derived from vibrationally excited CO or (sub)millimeter continuum. It is clear that further observational studies are needed to determine the best density tracers and to converge in the density estimates.

It seems that a single power law cannot adequately reproduce the variation of density through the whole extended atmosphere. It is likely that the radial density profile becomes progressively flatter away from the star until a power law with  $\beta = 2$  is reached outside the acceleration region. The radial pressure profile adopted for the chemical equilibrium calculations catches this idea and is shown as the thick magenta line in the lower panel of Fig. 1. With this prescription, the pressure at the stellar

surface is  $5 \times 10^{-5}$  bar, which agrees with typical values from hydrodynamical models. Then, pressure decreases to a few  $10^{-8}$  bar at  $2 R_*$ , which is in between the values derived from high angular resolution observations, and it finally becomes  $\sim 10^{-11}$  bar at  $10 R_*$ , which is in the range of values expected for a high mass-loss rate of  $\sim 10^{-5} M_{\odot} \text{ yr}^{-1}$ , as is the case of IRC +10216.

### 3. Parent molecules: successes and failures of chemical equilibrium

#### 3.1. Successes

Thermochemical equilibrium has been remarkably successful at explaining the molecular composition of circumstellar envelopes around AGB stars (e.g., Tsuji 1964, 1973). A major success is that chemical equilibrium has provided the theoretical framework for understanding the chemical differentiation between envelopes around M-, S-, and C-type AGB stars according to the elemental C/O at the star surface. In this scenario, CO is the most abundant molecule after  $H_2$  and it locks most of the carbon or oxygen depending on whether the C/O is lower or higher than one. This basic fact is at the heart of the most widely used method for determining mass-loss rates from AGB stars from observations of circumstellar emission in rotational lines of CO (Höfner & Olofsson 2018).

Predictions of chemical equilibrium for the budget of major elements have in the main been confirmed by observations. In Table 2 we list the parent molecules that have been observed in envelopes around AGB stars of M-, S-, and C-type and the derived abundance ranges. We refer to molecules that are formed in the inner regions of AGB envelopes as parent molecules, as opposed to daughter molecules that are formed in the external layers of the envelope. The parent character of the molecule has been confirmed for most by observation of high-energy lines or through interferometric maps. For a few, the information of their spatial distribution is not conclusive, although formation in the inner envelope is the most likely origin. The observed abundances are compared in Fig. 2 with the results from the chemical equilibrium calculations performed in this study for a standard AGB atmosphere, that is, using the elemental composition given in Table 1 and the pressure-temperature profile discussed in Sec. 2.4. Only gaseous species are included in the calculations presented in Fig. 2.

Calculated abundances are expressed here as mole fractions, while observed abundances are usually given in the literature relative to  $H_2$  (where it is implicitly assumed that most hydrogen is molecular). These two quantities are identical throughout most of the atmosphere. Only in the hot innermost regions, where atomic hydrogen may become more abundant than  $H_2$  (inner to  $\sim 2 R_*$  for our adopted radial profiles of pressure and temperature), can the two abundance measures differ by as much as a factor of two. For our purposes, this is not very important because calculated and observed abundances are compared at an order-of-magnitude level.

Chemical equilibrium calculations (e.g., Tsuji 1964, 1973) make clear predictions for the main reservoirs of C, N, and O in AGB atmospheres. The main carrier of oxygen (except for CO) in envelopes around oxygen-rich AGB stars is predicted to be  $H_2O$ . This has been verified by observations (González-Alfonso & Cernicharo 1999; Maercker et al. 2016). In carbon-rich AGB atmospheres, the main carriers of carbon (except for CO) are predicted to be  $C_2H_2$  and HCN, which is also supported observationally (Fonfría et al. 2008; Schöier et al. 2013). Molecular nitrogen is predicted to be the main carrier of nitrogen re-

gardless of the C/O, although this has never been confirmed by observations because it is difficult to detect  $N_2$ . Hydrocarbons such as  $CH_4$  and  $C_2H_4$  are calculated to be quite abundant at  $10 R_*$  in C-type atmospheres (see Fig. 2) and have been observed in IRC +10216 with abundances of about the predicted ones (Keady & Ridgway 1993; Fonfría et al. 2017). Furthermore, carbon dioxide is calculated with a mole fraction in the range  $10^{-8}$ - $10^{-6}$  in M-type atmospheres (see Fig. 2), and it is observed with an abundance relative to  $H_2$  of  $3 \times 10^{-7}$  in SW Vir (Tsuji et al. 1997).

Sulfur is predicted to be largely in the form of molecules such as CS and SiS in C-rich atmospheres, SiS in S-type stars, and  $H_2S$  in O-rich atmospheres (see Fig. 2), which essentially agrees with observations (Danilovich et al. 2017, 2018; Massalkhi et al. 2019). Other S-bearing molecules that are predicted to be abundant in M-type atmospheres are SO and SiS, and these species are indeed observed with relatively high abundances in some O-rich envelopes (Bujarrabal et al. 1994; Schöier et al. 2007; Danilovich et al. 2016; Massalkhi et al. 2020). The radical SH is predicted to be relatively abundant in the hot inner regions of AGB atmospheres and has been observed through infrared observations in the atmosphere of the S-type star R And (Yamamura et al. 2000).

Silicon monoxide (SiO) is predicted to be the most abundant Si-bearing molecule in the entire  $1$ - $10 R_*$  range in the atmospheres of M stars. In S-type atmospheres, the calculated abundance of SiO decreases by two orders of magnitude in the  $1$ - $5 R_*$  but retains a very high abundance beyond, and the same occurs in C-rich atmospheres, although in this case, the abundance drop in the  $1$ - $5 R_*$  is even more pronounced (see Fig. 2; see also Agúndez & Cernicharo 2006). Observations indicate that the abundance of SiO does not differ significantly between envelopes around M-, S-, and C-type stars, although in all them the SiO abundance decreases with increasing mass-loss rate (González Delgado et al. 2003; Schöier et al. 2006; Ramstedt et al. 2009; Massalkhi et al. 2019, 2020). This decline in the SiO abundance with increasing envelope density is not a consequence of chemical equilibrium (Massalkhi et al. 2019), but has been interpreted as evidence that SiO disappears from the gas phase at high densities to be incorporated into dust grains (González Delgado et al. 2003; Schöier et al. 2006; Ramstedt et al. 2009; Massalkhi et al. 2019, 2020). It therefore appears that the gradual abundance decline calculated for SiO in the  $1$ - $5 R_*$  region from stellar type in the sense  $M \rightarrow S \rightarrow C$  does not have a direct consequence in the SiO abundance that is injected into the expanding wind. However, this behavior predicted by chemical equilibrium probably explains why SiO masers are observed in M-type stars but not toward carbon stars (e.g., Pardo et al. 2004). Except for these details, chemical equilibrium and observations agree in the fact that SiO is one of the most abundant carriers of silicon in the atmospheres of M-, S-, and C-type stars. Calculations and observations also agree for SiS in that it is an abundant molecule regardless of the C/O. However, observations indicate a differentiation between C- and O-rich envelopes, with SiS being on average one order of magnitude more abundant in carbon-rich sources (Schöier et al. 2007; Danilovich et al. 2018; Massalkhi et al. 2019, 2020). Moreover, in some oxygen-rich envelopes, the fractional abundance of SiS relative to  $H_2$  is as low as  $\sim 10^{-8}$ , which is well below the predictions of chemical equilibrium (Danilovich et al. 2019; Massalkhi et al. 2020).

Two silicon-bearing molecules,  $SiC_2$  and  $Si_2C$ , become quite abundant in C-rich atmospheres according to chemical equilibrium (Tejero & Cernicharo 1991; Takano et al. 1992; Yasuda & Kozasa 2012), and somewhat less abundant in S-type atmo-

**Table 2.** Abundances (relative to H<sub>2</sub>) of parent molecules other than H<sub>2</sub> and CO derived from observations of M, S, and C stars.

Molecule	M stars		S stars		C stars	
<b>H<sub>2</sub>O</b>	$(0.3 - 4) \times 10^{-4}$	4 stars <sup>(1)</sup>	$(1.2 - 1.5) \times 10^{-5}$	2 stars <sup>(2,3)</sup>	$(0.1 - 5) \times 10^{-6}$	2 stars <sup>(4,5)</sup>
C <sub>2</sub> H <sub>2</sub>	–	–	–	–	$(0.75 - 8) \times 10^{-5}$	IRC +10216 <sup>(6)</sup>
<b>HCN</b>	$(0.18 - 5) \times 10^{-7}$	25 stars <sup>(7)</sup>	$(0.06 - 4.5) \times 10^{-6}$	18 stars <sup>(7)</sup>	$(0.17 - 8) \times 10^{-5}$	26 stars <sup>(7)</sup>
CO <sub>2</sub>	$3 \times 10^{-7}$	SW Vir <sup>(8)</sup>	–	–	–	–
CH <sub>4</sub>	–	–	–	–	$3.5 \times 10^{-6}$	IRC +10216 <sup>(9)</sup>
<b>NH<sub>3</sub></b>	$(0.25 - 1) \times 10^{-6}$	3 stars <sup>(10)</sup>	$1.7 \times 10^{-5}$	W Aql <sup>(3)</sup>	$6 \times 10^{-8}$	IRC +10216 <sup>(11)</sup>
C <sub>2</sub> H <sub>4</sub>	–	–	–	–	$6.9 \times 10^{-8}$	IRC +10216 <sup>(12)</sup>
SO	$(0.12 - 6.0) \times 10^{-6}$	30 stars <sup>(13)</sup>	–	–	–	–
<b>CS</b>	$(0.014 - 1.1) \times 10^{-7}$	30 stars <sup>(13)</sup>	$(0.1 - 8.2) \times 10^{-6}$	6 stars <sup>(14)</sup>	$(0.027 - 2.1) \times 10^{-5}$	25 stars <sup>(15)</sup>
H <sub>2</sub> S	$(0.05 - 3) \times 10^{-5}$	5 stars <sup>(16)</sup>	–	–	$4 \times 10^{-9}$	IRC +10216 <sup>(17)</sup>
SH	–	–	$2 \times 10^{-7}$	R And <sup>(18)</sup>	–	–
<b>SO<sub>2</sub></b>	$(0.04 - 7.4) \times 10^{-6}$	30 stars <sup>(13)</sup>	–	–	–	–
SiO	$(0.02 - 5.4) \times 10^{-5}$	45 stars <sup>(19)</sup>	$(0.04 - 6.8) \times 10^{-5}$	25 stars <sup>(20)</sup>	$(0.003 - 1) \times 10^{-5}$	25 stars <sup>(15)</sup>
SiS	$(0.0062 - 1.9) \times 10^{-6}$	30 stars <sup>(13)</sup>	$(0.18 - 1.5) \times 10^{-6}$	5 stars <sup>(14)</sup>	$(0.096 - 1.1) \times 10^{-5}$	25 stars <sup>(15)</sup>
SiC <sub>2</sub>	–	–	–	–	$(0.037 - 3.7) \times 10^{-5}$	25 stars <sup>(21)</sup>
Si <sub>2</sub> C	–	–	–	–	$(0.4 - 2) \times 10^{-7}$	IRC +10216 <sup>(22)</sup>
<b>SiH<sub>4</sub></b>	–	–	–	–	$2.2 \times 10^{-7}$	IRC +10216 <sup>(9)</sup>
HCP	–	–	–	–	$2.5 \times 10^{-8}$	IRC +10216 <sup>(17,23)</sup>
PO	$(0.55 - 1) \times 10^{-7}$	3 stars <sup>(24)</sup>	–	–	–	–
PN	$(1 - 2) \times 10^{-8}$	3 stars <sup>(24)</sup>	–	–	$3 \times 10^{-10}$	IRC +10216 <sup>(25)</sup>
<b>PH<sub>3</sub></b>	–	–	–	–	$1 \times 10^{-8}$	IRC +10216 <sup>(26)</sup>
HF	–	–	–	–	$8 \times 10^{-9}$	IRC +10216 <sup>(27)</sup>
HCl	–	–	$1.5 \times 10^{-8}$	R And <sup>(18)</sup>	$1 \times 10^{-7}$	IRC +10216 <sup>(27)</sup>
NaCl	$4 \times 10^{-9}$	IK Tau <sup>(28)</sup>	–	–	$1.8 \times 10^{-9}$	IRC +10216 <sup>(17,29)</sup>
KCl	–	–	–	–	$5 \times 10^{-10}$	IRC +10216 <sup>(17)</sup>
AlCl	$(0.09 - 2.5) \times 10^{-8}$	2 stars <sup>(30)</sup>	–	–	$7 \times 10^{-8}$	IRC +10216 <sup>(17)</sup>
AlF	–	–	–	–	$1 \times 10^{-8}$	IRC +10216 <sup>(17)</sup>
AlO	$(0.1 - 9.5) \times 10^{-8}$	3 stars <sup>(30,31)</sup>	–	–	–	–
AlOH	$(1.4 - 4.4) \times 10^{-9}$	2 stars <sup>(30)</sup>	–	–	–	–
TiO	$(0.1 - 1.0) \times 10^{-7}$	<i>o</i> Cet <sup>(32)</sup>	–	–	–	–
TiO <sub>2</sub>	$(0.1 - 1.0) \times 10^{-7}$	<i>o</i> Cet <sup>(32)</sup>	–	–	–	–
NaCN	–	–	–	–	$3 \times 10^{-9}$	IRC +10216 <sup>(17,33)</sup>
KCN	–	–	–	–	$6 \times 10^{-10}$	IRC +10216 <sup>(34)</sup>

Note: The cases in which observed abundances are much higher than expected from chemical equilibrium are highlighted in blue.

References: (1) Maercker et al. (2016). (2) Schöier et al. (2011). (3) Danilovich et al. (2014). (4) Decin et al. (2010). (5) Neufeld et al. (2010). (6) Fonfría et al. (2008). (7) Schöier et al. (2013). (8) Tsuji et al. (1997). (9) Keady & Ridgway (1993). (10) Wong et al. (2018). (11) Schmidt et al. (2016). (12) Fonfría et al. (2017). (13) Massalkhi et al. (2020). (14) Danilovich et al. (2018). (15) Massalkhi et al. (2019). (16) Danilovich et al. (2017). (17) Agúndez et al. (2012). (18) Yamamura et al. (2000). (19) González Delgado et al. (2003). (20) Ramstedt et al. (2009), V386 Cep removed. (21) Massalkhi et al. (2018). (22) Cernicharo et al. (2015). (23) Agúndez et al. (2007). (24) Ziurys et al. (2018). (25) Milam et al. (2008). (26) Agúndez et al. (2014b). (27) Agúndez et al. (2011). (28) Milam et al. (2007). (29) Quintana-Lacaci et al. (2016). (30) Decin et al. (2017). (31) Kamiński et al. (2016). (32) Kamiński et al. (2017). (33) Quintana-Lacaci et al. (2017). (34) Pulliam et al. (2010).

spheres (see Fig. 2). The two molecules are observed to be abundant in the carbon star IRC +10216, as reported by Cernicharo et al. (2010, 2015), although Massalkhi et al. (2018) found that the abundance of SiC<sub>2</sub> is not uniform in C-rich envelopes, but that, similarly to the case of SiO, it decreases with increasing mass-loss rate. As Massalkhi et al. (2018) pointed out, this behavior does not arise from chemical equilibrium, but indicates that SiC<sub>2</sub> is a potential gas-phase precursor of SiC dust.

For phosphorus, chemical equilibrium predicts that HCP is a main carrier in C-type atmospheres, while PO dominates to a large extent in M-type stars (Agúndez et al. 2007; Milam et al. 2008). The two molecules have been detected in the corresponding environments, which confirms this point (Agúndez et al. 2007; Ziurys et al. 2018). Calculations also predict a relative abundance of about  $10^{-10}$  for PN in C-rich atmospheres. This value agrees with the abundance derived in the C-star envelope IRC +10216 (Milam et al. 2008).

The halogen elements fluorine and chlorine are predicted to be largely in the form of HF and HCl in the inner regions of AGB atmospheres, regardless of the C/O (see Fig. 2). The fact that most F is predicted to be in the form of HF has been used

to derive fluorine abundances in carbon stars by observing the  $\nu = 1-0$  vibrational band of HF (Abia et al. 2010). An independent measurement of the abundance of HF was provided by the detection of the  $J = 1-0$  rotational transition in the C-rich envelope IRC +10216 (Agúndez et al. 2011). The abundance derived in this study was found to be  $\sim 10\%$  of the value expected if fluorine were mostly in the form of HF with a solar abundance, which was interpreted in terms of depletion onto dust grains. Agúndez et al. (2011) also reported observations of low- $J$  transitions of HCl in IRC +10216 and derived an abundance for HCl of 15% of the solar abundance of chlorine, while Yamamura et al. (2000) derived an even lower abundance for HCl in the S-type star R And from observations of ro-vibrational lines. The missing chlorine might be depleted onto dust grains or in atomic form. Given the variation in chemical equilibrium abundances of HF and HCl with radius (see Fig. 2) and the uncertainties in the abundances derived from observations, we can consider that calculations and observations agree that HF and HCl are important carriers of fluorine and chlorine, respectively, in AGB atmospheres. However, observations of these two molecules in

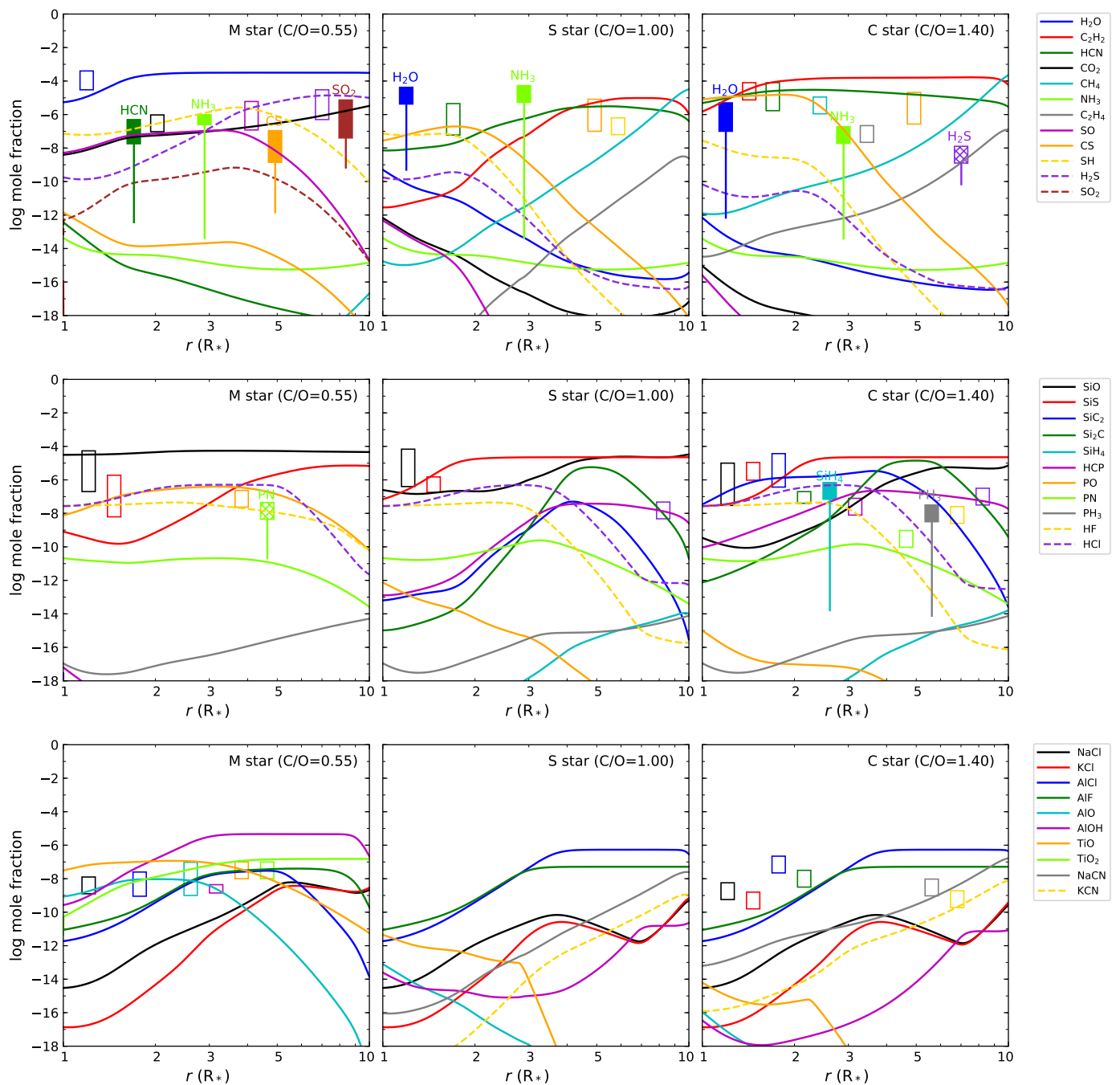


**Fig. 2.** Calculated chemical equilibrium abundances of parent molecules in M-, S-, and C-type AGB atmospheres are shown as a function of radius and are compared with abundances derived from observations. Chemical equilibrium calculations include only gaseous species. Observed abundances are indicated by rectangles, whose vertical extent corresponds to the range of observed abundances given in Table 2. Rectangles are located at different radii to facilitate visualization. Empty rectangles correspond to cases in which observed abundances agree with any of the abundances calculated by chemical equilibrium in the 1-10  $R_*$  range (usually the maximum abundance). Filled rectangles are used to indicate cases with a severe disagreement (by several orders of magnitude) between observed and calculated abundances, while we use hatched rectangles to indicate a significant disagreement (by more than one order of magnitude). The level of disagreement between the observed and maximum calculated abundance is indicated by a vertical line.

more sources is needed to understand the chemistry of halogens in AGB atmospheres better.

Unlike in interstellar clouds, where metals largely form part of dust grains, a wide variety of metal-bearing molecules are observed in the envelopes around AGB stars. Many of them are in fact formed in the hot stellar atmosphere, where they are relatively abundant according to chemical equilibrium, and are later incorporated into the expanding envelope. Early observations

of metal-containing molecules revealed the metal halides NaCl, KCl, AlCl, and AlF (Cernicharo & Guélin 1987), while the metal cyanides NaCN and KCN were detected later (Turner et al. 1994; Pulliam et al. 2010). All these molecules were discovered in the C-star envelope IRC+10216, and some of them have been observed exclusively in this source. Other metal cyanides such as MgNC or CaNC are observed in IRC+10216 (Kawaguchi et al. 1993; Guélin et al. 1993; Cernicharo et al. 2019a), al-

though they are formed in the outer envelope and thus are not parent molecules. The parent character of NaCN has been confirmed through interferometric observations (Quintana-Lacaci et al. 2017), while in the case of KCN, the parent character is merely suggested by chemical equilibrium, which predicts a similar behavior as for NaCN in C-star atmospheres (see Fig. 2). In general, the abundances derived for NaCl, KCl, AlCl, AlF, NaCN, and KCN in IRC +10216 (Pulliam et al. 2010; Agúndez et al. 2012) are consistent with the expectations from chemical equilibrium calculations of C-rich AGB atmospheres. The metal halides NaCl and AlCl have also been observed in a few O-rich envelopes (Milam et al. 2007; Decin et al. 2017) with abundances that agree with chemical equilibrium calculations.

Some metal oxides have long been observed at optical and near-infrared wavelengths in the spectra of AGB stars. For example, TiO and VO are detected toward M- and S-type stars (Joyce et al. 1998), and the oxides of *s*-process elements ZrO, YO, and LaO are conspicuous in S-type stars (Keenan 1954). More recently, metal oxides such as AlO, AlOH, TiO, and TiO<sub>2</sub> have been detected toward M-type AGB stars through their rotational spectrum, which allows constraining their abundances (Kamiński et al. 2016, 2017; Decin et al. 2017). In general, the abundances derived for AlO, AlOH, TiO, and TiO<sub>2</sub> agree well with the values calculated by chemical equilibrium in O-rich AGB atmospheres (see Fig. 2). These molecules are clearly parent molecules, as confirmed by interferometric observations, and studying them is interesting because some of them may act as gas-phase precursors in the formation of dust around M stars.

### 3.2. Failures

In recent years, increasingly more observational discoveries of parent molecules in AGB envelopes have severely disagreed with the predictions of chemical equilibrium. Several molecules are observed in envelopes around AGB stars of certain chemical type with abundances well above (by several orders of magnitude) the expectations from chemical equilibrium calculations. It is interesting to note that the disagreement with chemical equilibrium always means anomalously overabundant molecules. That is, no molecule is predicted to be abundant that is observed to be much less abundant. These anomalously overabundant molecules are highlighted in blue in Table 2 and are also indicated by filled rectangles in Fig. 2, with a vertical line that shows the level of disagreement between observations and chemical equilibrium.

One of the most noticeable failures of chemical equilibrium concerns H<sub>2</sub>O. This molecule is predicted and observed to be very abundant in O-rich envelopes, but in S- and C-type stars, water is predicted to have a negligible abundance and is expected not to be observable, although it is detected with a relatively high abundance (see Fig. 2). The history of the problem of water started with the detection of the low-energy rotational line at 557 GHz in the carbon star IRC +10216 with the space telescopes Submillimeter Wave Astronomy Satellite (SWAS) and *Odin* (Melnick et al. 2001; Hasegawa et al. 2006). Different scenarios were offered to explain this unexpected discovery, and they included the sublimation of cometary ices from a putative Kuiper belt analog (Melnick et al. 2001; Ford & Neufeld 2001), Fischer-Tropsch catalysis on iron grains (Willacy 2004), and the formation in the outer envelope through the radiative association of H<sub>2</sub> and O (Agúndez & Cernicharo 2006). The subsequent detection with *Herschel* of many high-energy rotational lines of H<sub>2</sub>O in IRC +10216 ruled out the three previous scenarios and constrained the formation region of water to the very inner re-

gions of the envelope, within 5-10  $R_*$  (Decin et al. 2010). The presence of water in C-rich envelopes was found to be a common phenomenon and not restricted to IRC +10216 (Neufeld et al. 2011). Moreover, the problem of water in carbon stars has been extended to S-type AGB stars with the detection of abundant H<sub>2</sub>O in some sources (Schöier et al. 2011; Danilovich et al. 2014). As illustrated in Fig. 2, the problem of water is a problem of more than four to five orders of magnitude.

Ammonia is also a remarkable example of chemical equilibrium breakdown in AGB atmospheres. The chemical equilibrium abundance of NH<sub>3</sub> is vanishingly small regardless of the C/O (see Fig. 2). Nonetheless, infrared observations of ro-vibrational lines and *Herschel* observations of the low-energy rotational line at 572 GHz have outlined a scenario in which NH<sub>3</sub> is fairly abundant, with abundances relative to H<sub>2</sub> in the range 10<sup>-7</sup>-10<sup>-5</sup> in envelopes around M-, S-, and C-type AGB stars (Danilovich et al. 2014; Schmidt et al. 2016; Wong et al. 2018). The formation radius of NH<sub>3</sub> is constrained to be in the range 5-20  $R_*$  in the C-star envelope IRC +10216 (Keady & Ridgway 1993; Schmidt et al. 2016). For ammonia, the disagreement with chemical equilibrium is a problem of more than six orders of magnitude.

The carbon-bearing molecules HCN and CS are together with C<sub>2</sub>H<sub>2</sub> the main carriers of carbon in C-type atmospheres. HCN and CS are observed with high abundances in C-rich envelopes, which agrees with expectations from chemical equilibrium. In the atmospheres of S-type stars, the two molecules are also predicted to be relatively abundant, although with somewhat lower abundances than in C-type atmospheres. This has also been verified observationally (see Fig. 2). HCN and CS show a clear chemical differentiation depending on the C/O because observed abundances in oxygen-rich envelopes are systematically lower than in C-rich sources by about two orders of magnitude (Bujarrabal et al. 1994; Schöier et al. 2013; Danilovich et al. 2018; Massalkhi et al. 2019). Although the observed abundances of HCN and CS in O-rich envelopes are below those in C-rich envelopes, they are still much higher than expected from chemical equilibrium, which for C/O < 1 predicts negligible abundances for these two molecules. According to the interferometric observations by Decin et al. (2018a), HCN is formed at radii smaller than about 6  $R_*$  in R Dor, while in the case of CS, the abundance profiles derived for IK Tau, W Hya, and R Dor indicate a formation radius of a few stellar radii (Danilovich et al. 2019). The difference between observed abundances and the values calculated by chemical equilibrium is large, more than four orders of magnitude for CS and more than five orders of magnitude for HCN (see Fig. 2).

Sulfur dioxide (SO<sub>2</sub>) has been observed in oxygen-rich AGB envelopes for a long time (Omont et al. 1993). It was originally thought to be formed in the outer layers of the envelope, but infrared observations of the  $\nu_3$  band at 7.3  $\mu$ m by Yamamura et al. (1999) and observations of high-energy rotational lines (Danilovich et al. 2016; Velilla Prieto et al. 2017) indicated that in fact SO<sub>2</sub> originates in the inner regions of the envelope with abundances of about 10<sup>-6</sup> relative to H<sub>2</sub>. The result is striking because the chemical equilibrium abundance predicted for SO<sub>2</sub> in M-type atmospheres is lower by at least three to four orders of magnitude (see Fig. 2). Velilla Prieto et al. (2017) reported a formation radius for SO<sub>2</sub> in IK Tau in the range 1-8  $R_*$ , although interferometric observations would be desirable.

In addition to H<sub>2</sub>O and NH<sub>3</sub>, there are two other hydrides, silane (SiH<sub>4</sub>) and phosphine (PH<sub>3</sub>), that are observed in C-rich envelopes with abundances well above the prediction of chemical equilibrium. Silane was detected in the carbon star IRC +10216 through infrared observations of ro-vibrational

lines (Keady & Ridgway 1993), while phosphine has been observed toward the same carbon star from observations of low-energy rotational transitions (Agúndez et al. 2008, 2014b). The formation radii of SiH<sub>4</sub> and PH<sub>3</sub> in IRC +10216 are not well constrained, although Keady & Ridgway (1993) favored a distribution in which SiH<sub>4</sub> is present from  $\sim 40 R_*$ . Thus, silane can be considered a late parent species because of its large formation radius. The discrepancy between the abundances derived from observations and the values calculated with chemical equilibrium is  $> 6$  orders of magnitude for SiH<sub>4</sub> and PH<sub>3</sub>. It is curious to note that all the anomalously overabundant molecules in C-type AGB stars are hydrides. The same is not true for M-type AGB stars.

Several molecules show a large discrepancy between the abundances derived from observations and calculated by chemical equilibrium, although it is not as severe as for the molecules discussed above. We refer to PN in O-rich stars and H<sub>2</sub>S in C-rich stars, which are indicated by hatched rectangles in Fig. 2. For PN in O-rich AGB atmospheres, the disagreement between the observed abundances,  $(1-2)\times 10^{-8}$  (Ziurys et al. 2018), and the calculated maximum chemical equilibrium abundance is almost three orders of magnitude. However, uncertainties on the observational and theoretical sides mean that the true level of disagreement is unclear. For example, while Ziurys et al. (2018) derived a PN abundance of  $10^{-8}$  relative to H<sub>2</sub> in IK Tau, De Beck et al. (2013) and Velilla Prieto et al. (2017) derived higher abundances,  $(3-7)\times 10^{-7}$ , in this source. When we give preference to these latter abundances, the level of disagreement would be even higher. On the other hand, the formation enthalpy of PN is rather uncertain (see Lodders 1999), which directly translates into the calculated chemical equilibrium abundance. In this study we adopted the thermochemical data for PN from Lodders (1999), who gives preference to a formation enthalpy at 298.15 K of 171.5 kJ mol<sup>-1</sup>, while other compilations such as JANAF use lower values that would result in higher chemical equilibrium abundances for PN. This would reduce the level of disagreement. In the case of H<sub>2</sub>S in C-rich AGB stars, the calculated maximum chemical equilibrium abundance is  $7 \times 10^{-11}$ , while the value derived from observations is  $\sim 50$  times higher. In this case, the observed abundance is based on the detection of only one line in only one source (see Agúndez et al. 2012), and thus it has to be viewed with some caution. In summary, the main failures of chemical equilibrium to account for the observed abundances of parent molecules in circumstellar envelopes are NH<sub>3</sub>, HCN, CS, SO<sub>2</sub>, and possibly PN in M-type stars, H<sub>2</sub>O and NH<sub>3</sub> in S-type stars, and the hydrides H<sub>2</sub>O, NH<sub>3</sub>, SiH<sub>4</sub>, PH<sub>3</sub>, and perhaps H<sub>2</sub>S as well in C-type stars. The large discrepancies between the abundances derived from observations and those calculated with chemical equilibrium necessarily imply that nonequilibrium chemical processes must be at work in AGB atmospheres. Any invoked nonequilibrium scenario must account for all these anomalously overabundant molecules, but must also reproduce the remaining molecular abundances that are reasonably well explained by chemical equilibrium. No scenario currently provides a fully satisfactory agreement with observations, although two mechanisms that can drive the chemical composition out of equilibrium have been proposed.

The first scenario involves shocks that are produced in the extended atmosphere as a consequence of the pulsation of the AGB star. A model based on this scenario was originally developed to study the inner wind of the carbon star IRC +10216 (Willacy & Cherchneff 1998) and the oxygen-rich Mira star IK Tau (Duari et al. 1999), and was later generalized by Cherchneff (2006) to AGB winds with different C/O. The main successes of these

models were that they resulted in high abundances for HCN and CS in O-rich winds, although neither was H<sub>2</sub>O efficiently produced in C-rich winds nor NH<sub>3</sub> independently of the C/O. Subsequent models in which the chemical network was modified resulted in a relatively high abundance of H<sub>2</sub>O in C-rich AGB winds (Cherchneff 2011, 2012). In this new chemical network, however, rate constants of reverse reactions do not obey detailed balance, which may affect the predicted abundance of water. Similar models performed by Marigo et al. (2016) found that in O-rich atmospheres, HCN is only formed with abundances of about the observed ones when nearly isothermal shocks are considered.

A different scenario that consists of photochemistry driven by interstellar ultraviolet photons that would penetrate the inner envelope through the clumpy envelope was proposed by Decin et al. (2010) to explain the formation of water in the inner envelope of IRC +10216. The scenario was later generalized to AGB envelopes with different C-to-O ratios by Agúndez et al. (2010). In these models, warm photochemistry is able to efficiently form H<sub>2</sub>O, NH<sub>3</sub>, and H<sub>2</sub>S in the inner regions of C-rich envelopes, while NH<sub>3</sub>, HCN, and CS are synthesized in the inner layers of O-rich envelopes. Similar models based on a different formalism were carried out by Van de Sande et al. (2018), who found similar qualitative results. Van de Sande et al. (2019) then found that ultraviolet photons from the AGB star could also lead to some photochemistry for sufficiently high stellar temperatures and degree of clumpiness.

Although the two scenarios are promising in that they result in an enhancement of some of the anomalously overabundant parent molecules observed in AGB envelopes, the main problem with them is that they are quite parametric, that is, they depend on parameters such as the shock strength or the degree of clumpiness. These parameters are poorly constrained from observations.

### 3.3. S-type atmospheres: sensitivity to C/O

The chemical equilibrium calculations for an S-type atmosphere shown in Fig. 2 assume that the elemental C/O is exactly one. However, the C/O of S stars may range from slightly oxygen-rich to slightly carbon-rich. Because  $C/O < 1$  and  $C/O > 1$  imply a marked chemical differentiation, we here explore how sensitive molecular abundances are to slight changes in the C/O. This provides an idea of the diversity of the atmospheric composition between S stars with slightly different C-to-O ratios. In Fig. 3 we show the abundances of some important parent molecules as a function of radius for C-to-O ratios in the range 0.98-1.02. These calculations include only gaseous species. Over this narrow range of C-to-O ratios, some molecules experience large abundance variations (e.g., C<sub>2</sub>H<sub>2</sub> and SiC<sub>2</sub>), while other species remain almost insensitive to C/O (e.g., NH<sub>3</sub>, H<sub>2</sub>S, and SiS). The sensitivity to the C/O is more pronounced in the inner atmosphere, while at radii larger than  $\sim 5 R_*$ , molecules tend to show little abundance variation with C/O. If the abundances of the parent molecules are set by the chemical equilibrium values in the hot inner regions, we therefore expect large abundance variations from source to source that reflect the diversity of C-to-O ratios from slightly below one to slightly above one. This would be most noticeable for molecules such as C<sub>2</sub>H<sub>2</sub>, HCN, CS, SiO, and SiC<sub>2</sub>, for which the predicted abundances range from moderately high to very low, depending on whether the C/O is higher or lower than one. The severe disagreement that is found between chemical equilibrium and observations for H<sub>2</sub>O and NH<sub>3</sub> in S-

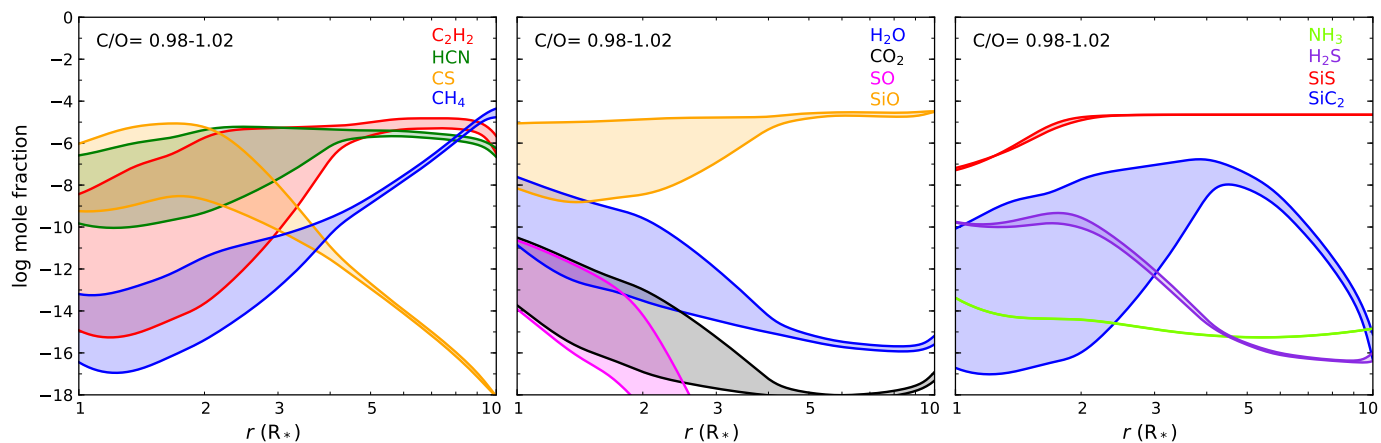


**Fig. 3.** Calculated chemical equilibrium abundances of selected parent molecules as a function of radius for an S-type atmosphere, where the shadowed regions correspond to calculated abundances adopting C/O in the range 0.98-1.02. Chemical equilibrium calculations include only gaseous species.

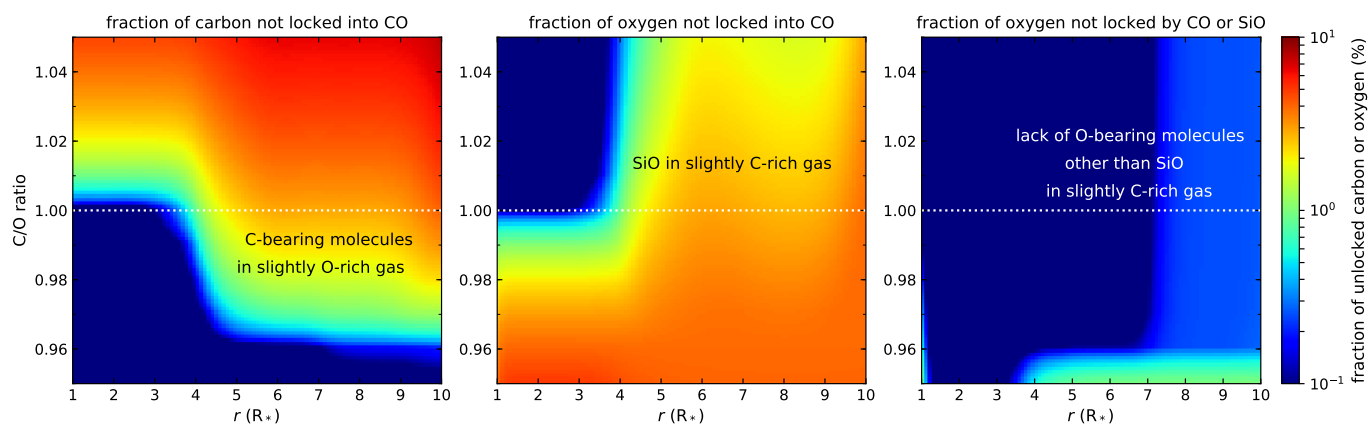


**Fig. 4.** Left and middle panels: Fractions of C and O that is not locked into CO as a function of radius and C/O, as calculated by gas-phase chemical equilibrium. To illustrate that the vast majority of oxygen that is not locked into CO is trapped by SiO for C-to-O ratios around one, we show in the right panel the fraction of oxygen that is not locked by CO or SiO. Chemical equilibrium calculations include only gaseous species.

type stars (see the discussion in Sec. 3.2) persists when the C/O is allowed to vary slightly around one.

In general, carbon-bearing molecules reach higher abundances than oxygen-bearing molecules for C-to-O ratios around one. For example, C-bearing molecules such as HCN, C<sub>2</sub>H<sub>2</sub>, and CH<sub>4</sub> maintain moderately high abundances over certain radii in slightly oxygen-rich conditions, while the only O-bearing molecule that is present with a non-negligible abundance under slightly carbon-rich conditions is SiO. Other O-bearing molecules such as H<sub>2</sub>O and SO need C-to-O ratios well lower than one to reach moderately high abundances. The reason for this behavior is illustrated in Fig. 4. For radii larger than  $\sim 4 R_*$ , when the gas is slightly O-rich (C/O in the range 0.96-1.00), a few percent of the carbon is not locked by CO and goes to C-bearing molecules such as C<sub>2</sub>H<sub>2</sub>, HCN, and CH<sub>4</sub>. When we now focus on slightly C-rich conditions, we see that for radii larger than  $\sim 4 R_*$ , a few percent of oxygen is not trapped by CO. However, in this case, the oxygen that is not locked by CO is mostly in the form of SiO. SiO even competes with CO for the oxygen over a wide range of C-to-O ratios, and this is the origin of the relatively high abundance of SiO in C-rich AGB atmospheres. Except for SiO, no other O-bearing molecule is predicted with a significant abundance under slightly C-rich conditions. In summary, C-bearing molecules compete more efficiently with CO

for the carbon than O-bearing molecules (other than SiO) for the oxygen. The consequence is that the chemical equilibrium composition of S-type atmospheres resembles that of carbon stars more closely than that of M-type stars.

#### 4. Potentially detectable molecules

The gas-phase budget of the different elements that are included in the chemical equilibrium calculations in M-, S-, and C-type atmospheres is discussed in detail in Appendix A. The most abundant molecular reservoirs of the nonmetal elements (C, O, N, Si, S, P, F, Cl, and B) are typically observed in AGB envelopes with abundances in agreement with predictions from chemical equilibrium. The only cases where major molecular reservoirs are not detected correspond to nonpolar molecules, such as N<sub>2</sub>, or molecules containing elements with a very low abundance, such as B. Several molecules that are predicted to be relatively abundant have not yet been detected, however, and observations can therefore still be used to test the predictions of chemical equilibrium.

In Table 3 we present a list of molecules that have not yet been observed in AGB atmospheres but are predicted with non-negligible abundances, and thus are potentially observable. We generally include molecules for which the maximum calculated mole fraction over the 1-10  $R_*$  range is  $\geq 10^{-10}$ . These chemical

**Table 3.** Potentially detectable molecules in AGB atmospheres.

Molecule	Prediction <sup>a</sup>	Electric dipole moment (D)	Rotational spectrum measured?
CH	$\sim 3 \times 10^{-7}$ C stars	1.46 (Phelps & Dalby 1966)	Yes (Martin-Drumel et al. 2011)
CH <sub>2</sub>	$\sim 1 \times 10^{-8}$ C stars	0.591 (Woon & Herbst 2009)	Yes (Brünken et al. 2005)
NH	$\sim 5 \times 10^{-10}$ M, S, C stars	1.389 (Scarl & Dalby 1974)	Yes (Klaus et al. 1997; Flores-Mijangos et al. 2004; Lewen et al. 2004)
SiH	$\sim 1 \times 10^{-8}$ S, C stars	0.097 (Yurchenko et al. 2018)	Yes <sup>b</sup> (Betrencourt et al. 1986; Ram et al. 1998). See CDMS <sup>c</sup> .
PH	$\sim 1 \times 10^{-10}$ M, S, C stars	0.396 (CDMS) <sup>c</sup>	Yes (Goto & Saito 1993; Klisch et al. 1998)
O <sub>2</sub>	$\sim 5 \times 10^{-8}$ M stars	0 <sup>b</sup>	Yes (Drouin et al. 2010)
Si <sub>3</sub> C	$\sim 1 \times 10^{-7}$ S, C stars	$\sim 0.1$ (Stanton et al. 2005)	No
Si <sub>5</sub> C	$\sim 3 \times 10^{-6}$ S, C stars	0.27 B3LYP/cc-pVTZ <sup>e</sup>	No
SiNH	$\sim 1 \times 10^{-8}$ S, C stars	0.34 (McCarthy et al. 2015)	Yes (Bogey et al. 1991; McCarthy et al. 2015)
SiF	$\sim 1 \times 10^{-10}$ S, C stars	1.126 (Karna & Grein 1987)	Yes (Tanimoto et al. 1983)
SiCl	$\sim 1 \times 10^{-9}$ S, C stars	1.53 (Gosavi & Strausz 1986)	Yes (Tanimoto et al. 1984)
PS	$\sim 1 \times 10^{-7}$ M stars	0.565 (Müller & Woon 2013)	Yes (Ohishi et al. 1988)
HPO <sub>2</sub>	$\sim 1 \times 10^{-7}$ M stars	1.61 B3LYP/cc-pVTZ <sup>e</sup>	Yes <sup>b</sup> (O'Sullivan et al. 2006)
BO	$\sim 5 \times 10^{-10}$ M stars	2.62 (CDMS) <sup>c</sup>	Yes (Tanimoto et al. 1986)
HBO	$\sim 1 \times 10^{-9}$ M, S, C stars	2.69 (DeYonker et al. 2005)	Yes (Kawashima et al. 1987)
HBO <sub>2</sub>	$\sim 1 \times 10^{-9}$ M stars	2.78 (Dewar et al. 1988)	No
BF	$\sim 1 \times 10^{-9}$ S, C stars	0.50 (Dewar et al. 1988)	No
AlH	$\sim 1 \times 10^{-8}$ S, C stars	0.30 (Matos et al. 1988)	Yes (Halfen & Ziurys 2004, 2016)
	$\sim 1 \times 10^{-9}$ M stars		
AlS	$\sim 1 \times 10^{-10}$ M stars	3.63 (Guichemerre & Chambaud 2000)	Yes (Takano et al. 1991; Breier et al. 2018)
AlOF	$\sim 1 \times 10^{-8}$ M stars	1.62 B3LYP/cc-pVTZ <sup>e</sup>	No
MgS	$\sim 4 \times 10^{-9}$ M stars	6.88 (Fowler & Sadlej 1991)	Yes (Takano et al. 1989; Walker & Gerry 1997)
MgO	$\sim 1 \times 10^{-10}$ M stars	6.2 (Büsener et al. 1987)	Yes (Törring & Hoefft 1986)
CaS	$\sim 4 \times 10^{-8}$ M stars	10.47 (CDMS) <sup>c</sup>	Yes (Takano et al. 1989)
CaOH	$\sim 1 \times 10^{-8}$ M stars	1.465 (Steimle et al. 1992)	Yes (Ziurys et al. 1992; Scurlock et al. 1993)
CaCl	$\sim 1 \times 10^{-8}$ M stars	4.257 (Ernst et al. 1984)	Yes (Möller et al. 1982; Ernst & Törring 1983)
	$\sim 3 \times 10^{-10}$ S, C stars		
CaF <sub>2</sub>	$\sim 1 \times 10^{-8}$ M stars	3.340 (Szentpály & Schwerdtfeger 1990)	No
CaF	$\sim 5 \times 10^{-9}$ M stars	3.07 (Childs et al. 1984)	Yes (Anderson et al. 1994)
BaO	$\sim 1 \times 10^{-10}$ M stars	7.955 (Wharton et al. 1962)	Yes (Tiemann et al. 1974; Hocking et al. 1978; Blom et al. 1992)
BaS	$\sim 1 \times 10^{-10}$ M stars	10.86 (Melendres et al. 1969)	Yes (Tiemann et al. 1976; Helms et al. 1980; Janczyk & Ziurys 2006)
ScO	$\sim 1 \times 10^{-9}$ M stars	4.55 (Shirley et al. 1990)	Yes (Halfen et al. 2017)
ScO <sub>2</sub>	$\sim 1 \times 10^{-9}$ M stars	5.29 (Gutsev et al. 2000)	No
Ti <sub>8</sub> C <sub>12</sub>	$\sim 1 \times 10^{-8}$ S, C stars	0.72 B3LYP/cc-pVTZ + PP for Ti <sup>e</sup>	No
ZrO	$\sim 1 \times 10^{-9}$ M, S, C stars	2.551 (Suenram et al. 1990)	Yes (Suenram et al. 1990; Beaton & Gerry 1999)
ZrO <sub>2</sub>	$\sim 1 \times 10^{-9}$ M stars	7.80 (Brugh et al. 1999)	Yes (Brugh et al. 1999)
VO	$\sim 5 \times 10^{-9}$ M stars	3.355 (Suenram et al. 1991)	Yes (Suenram et al. 1991; Flory & Ziurys 2008)
VO <sub>2</sub>	$\sim 1 \times 10^{-8}$ M stars	5.40 (Gutsev et al. 2000)	No
CrS	$\sim 1 \times 10^{-9}$ M stars	4.91 (Bauschlicher & Maitre 1995)	Yes (Pulliam & Ziurys 2010)
CrO	$\sim 1 \times 10^{-10}$ M stars	3.88 (Steimle et al. 1989)	Yes (Sheridan et al. 2002)
CrCl	$\sim 1 \times 10^{-10}$ M stars	6.42 (Harrison & Hutchison 1999)	Yes (Oike et al. 1998; Katoh et al. 2004)
MnH	$\sim 1 \times 10^{-10}$ M, S, C stars	10.65 (Koseki et al. 2006)	Yes (Halfen & Ziurys 2008)
FeS	$\sim 4 \times 10^{-8}$ M stars	6.46 (Sharkas et al. 2017)	Yes (Takano et al. 2004)
FeO	$\sim 3 \times 10^{-10}$ M stars	4.50 (Steimle et al. 2004)	Yes (Kröckertskothén et al. 1987; Allen et al. 1996)
CoH	$\sim 1 \times 10^{-7}$ M, S, C stars	1.88 (Wang et al. 2009)	No
NiS	$\sim 4 \times 10^{-7}$ M stars	5.38 (Sharkas et al. 2017)	Yes (Yamamoto et al. 2007)

Notes:

<sup>a</sup> Maximum calculated mole fraction in the 1-10 R<sub>\*</sub> range and type of AGB star in which the molecule is predicted to be abundant.

<sup>b</sup> Rotational spectrum has not been directly measured, but it can be predicted from rotationally resolved vibrational or electronic spectra.

<sup>c</sup> Cologne Database for Molecular Spectroscopy (Müller et al. 2005): <https://cdms.astro.uni-koeln.de>
<sup>d</sup> Rotational transitions radiatively allowed by the nonzero magnetic dipole moment.

<sup>e</sup> From quantum-chemical calculations carried out in this study.

equilibrium calculations include only gaseous species. We also list the electric dipole moment of each molecule and indicate whether the rotational spectrum has been measured in the laboratory. Some of these molecules are good targets for detection through high angular resolution and sensitive observations using observatories such as ALMA. Some molecules are more favorable for detection than others. Factors that play against detection are a low abundance, a low dipole moment, a complex rotational spectrum, which results in spectral dilution, and a low spatial extent restricted to the photosphere and near surroundings. The

latter may occur for some radicals that are only abundant in the very inner atmosphere and may be converted into more stable molecules at larger radii by nonequilibrium chemistry, and for metal-bearing molecules that can be severely depleted from the gas phase at relatively short radii because they are incorporated into condensates. Sensitive high angular resolution observations able to probe the very inner atmosphere are the best way to observe these molecules. For some molecules, the probabilities of detection are uncertain because they only reach high abundances

at large radii, close to  $10 R_*$ , where chemical equilibrium is less likely to hold because the temperatures and pressures are lower.

#### 4.1. Nonmetal molecules

The hydride radicals CH, CH<sub>2</sub>, and NH reach maximum abundance in the photosphere and show a marked abundance fall-off with increasing radius. The probabilities of detecting these species depend on whether the photospheric abundance can be maintained throughout the extended atmosphere and be injected into the expanding wind, or if these radicals are chemically processed and converted into more stable molecules such as methane and ammonia. If their presence is restricted to the innermost atmosphere, observations with a high angular resolution or in the infrared domain might allow probing them. The hydrides SiH and PH are also abundant in the photosphere, but have a more extended distribution than the above three radicals, which makes it more likely that they survive the travel through the extended atmosphere. Their detection is complicated because their dipole moment is low, however.

Molecular oxygen is listed in Table 3, although its detection appears difficult. It has a relatively low mole fraction ( $\sim 5 \times 10^{-8}$ ) over a narrow region in the very inner atmosphere, and more importantly, the rotational transitions have very low intrinsic line strengths because there is no electric dipole moment. Detection of O<sub>2</sub> in AGB envelopes must probably await sensitive observations by future space telescopes.

Two of the silicon-carbon clusters, except for the already known SiC<sub>2</sub> and Si<sub>2</sub>C (see Table 2), Si<sub>3</sub>C and Si<sub>5</sub>C, are predicted to form with high abundances in S- and C-type atmospheres (see Appendix A.4 and the bottom panel of Fig. A.2). The thermochemical data for these species are taken from Deng et al. (2008). The low-dipole moments calculated for Si<sub>3</sub>C and Si<sub>5</sub>C hinder their detection. The detection of these two molecules must await the characterization of their rotational spectrum in the laboratory. The silicon-carbon cluster Si<sub>2</sub>C<sub>2</sub> is also predicted with a non-negligible abundance in S- and C-type atmospheres. However, this molecule has a nonpolar rhombic structure in its ground state (Lammertsma & Güner 1988; Presilla-Márquez et al. 1995; Rintelman & Gordon 2001; Deng et al. 2008) and thus cannot be detected through its rotational spectrum.

The molecule iminosilylene (SiNH) is predicted to be relatively abundant (mole fraction of up to  $10^{-8}$ ) in atmospheres around S- and C-type stars. Thermochemical data for this species are taken from the Chemkin Thermodynamic Database (Kee et al. 2000), which assigns a formation enthalpy at 298.15 K of 160.6 kJ mol<sup>-1</sup> based on quantum calculations. An astronomical search is feasible because the rotational spectrum has been measured in the laboratory (McCarthy et al. 2015), although the calculated dipole moment is low (0.34 D; McCarthy et al. 2015). The silicon monohalides SiF and SiCl are also potentially detectable in AGB atmospheres. They are predicted with mole fractions up to  $10^{-10}$  and  $10^{-9}$ , respectively, in S- and C-type atmospheres. Although the predicted abundances are not very high, the dipole moments in excess of 1 D (see Table 3) may help in the detection.

Of the P-bearing molecules that are not yet observed in AGB atmospheres, PS has the highest probabilities of being detected. This molecule has been predicted to be the most abundant P-bearing molecule in O-rich atmospheres by Tsuji (1973), although searches for it have not been successful (Ohishi et al. 1988). According to our calculations, PS is predicted in oxygen-rich atmospheres with an abundance as high as that of PO (which has already been observed), with the main difference that PO

locks most of the phosphorus in the 1.5-4.5  $R_*$  region, while PS is the main reservoir of P somewhat farther away (in the 4.5-7  $R_*$ ), although still in the region of influence of chemical equilibrium. The dipole moment is not very high (0.565 D; Müller & Woon 2013), but the high predicted abundance should permit a detection. The P-bearing molecule HPO<sub>2</sub> is also predicted with a high abundance in O-rich atmospheres, although only in the outer regions ( $> 8 R_*$ ), where chemical equilibrium is less likely to hold. The most stable isomer of HPO<sub>2</sub> (*cis* HOPO) has been characterized spectroscopically in the laboratory (O'Sullivan et al. 2006), although the pure rotational spectrum has not been directly measured.

Several B-containing molecules are predicted to lock most of the boron, depending on the region of the atmosphere and the C/O. Concretely, BO, HBO, and HBO<sub>2</sub> are predicted to be main reservoirs of boron in O-rich atmospheres, while in S- and C-type atmospheres, HBO and BF are the main molecular carriers of this element. The main handicap in detecting them is the low elemental abundance of boron ( $5 \times 10^{-10}$  relative to H). Because these molecules are main reservoirs of boron and because their dipole moment is high (except for BF), however, observation of some of them is feasible, which would place some constraints on the so far unexplored chemistry of boron.

#### 4.2. Metal-bearing molecules

The observation of metal-containing molecules is complicated by several facts. First, many of the metals are present at a level of trace. Second, in many cases, the main gas-phase reservoir of the metal is atomic, and molecules are predicted at a lower level. Third, metals have a refractory character and thus high condensation temperatures, which cause them to easily leave the gas phase to form condensates. In spite of these difficulties, a variety of metal-bearing molecules have been detected with abundances in agreement with expectations from chemical equilibrium. Currently, constraints on the molecular budget of metals in the atmospheres of AGB stars are restricted to Na, K, Al, and Ti (see Table 2), although there is still some margin for a further characterization of the molecular reservoirs of other metals.

In addition the Al-bearing molecules known in AGB atmospheres (AlCl, AlF, AlO, and AlOH), some others could be detected. Aluminum monohydride (AlH) is predicted with a non-negligible abundance in M-, S-, and C-type atmospheres. This molecule has been detected in the O-rich star *o* Cet through optical observations (Kamiński et al. 2016), although no abundance was derived. The rotational spectrum of AlH is known from the laboratory (Halfen & Ziurys 2004, 2016), and thus it can be searched for at (sub-)millimeter wavelengths. However, the low dipole moment (0.30 D; Matos et al. 1988) and the fact that the two lowest rotational transitions cannot be observed from the ground because they lie close to water atmospheric lines play against its detection. The molecules AlS and AlOF are also potentially detectable in O-rich atmospheres because they are predicted with non-negligible abundances (mole fractions up to  $10^{-10}$  and  $10^{-8}$ , respectively). Other Al-bearing molecules are predicted to be quite abundant, such as Al<sub>2</sub>O, Al(OH)<sub>3</sub> in M stars and Al<sub>2</sub>C<sub>2</sub> in C stars (see the bottom panel of Fig. A.5). However, their structures are predicted to be highly symmetric with zero or very low dipole moment (Turney et al. 2005; Wang & Andrews 2007; Cannon et al. 2000; Naumkin 2008; Dong et al. 2010), which means that it is very unlikely if not impossible to detect them through their rotational spectrum.

Magnesium is predicted to be essentially in the form of neutral atoms in AGB atmospheres. Several Mg-bearing molecules

have been observed in the C-rich AGB envelope IRC +10216, however, such as MgNC, MgCN, HMgNC, MgC<sub>3</sub>N, MgC<sub>2</sub>H, and MgC<sub>4</sub>H (Kawaguchi et al. 1993; Guélin et al. 1993; Ziurys et al. 1995; Cabezas et al. 2013; Agúndez et al. 2014c; Cernicharo et al. 2019b), although they are formed in the outer envelope and thus are not parent molecules. The most promising candidate of the Mg-bearing parent molecules for detection are MgS and MgO, which are predicted with non-negligible abundances in O-rich atmospheres and have fairly high dipole moments (Fowler & Sadlej 1991; Büsener et al. 1987).

Neutral atoms are also the main reservoir in AGB atmospheres for calcium. However, some molecules are predicted to trap a fraction of Ca in the 3-10  $R_*$  range, reaching non-negligible abundances. This is the case of CaS, which is predicted to have a mole fraction as high as  $4 \times 10^{-8}$  in O-rich atmospheres. Its very high dipole moment (10.47 D; see Table 3) makes it a very interesting candidate for detection. The hydroxides CaOH and Ca(OH)<sub>2</sub> are also predicted to be abundant in the outer parts of O-rich atmospheres. While CaOH has a dipole moment of 1.465 D (Steimle et al. 1992), Ca(OH)<sub>2</sub> is predicted to be highly linear with a very low or zero dipole moment (Wang & Andrews 2005; Vasiliu et al. 2010). The calcium halides CaCl, CaCl<sub>2</sub>, CaF, and CaF<sub>2</sub> are also predicted with non-negligible abundances, especially in oxygen-rich atmospheres. Of these, CaCl, CaF, and CaF<sub>2</sub> have high dipole moments, but CaCl<sub>2</sub> is predicted to be linear and thus nonpolar (Vasiliu et al. 2010). Ziurys et al. (1994) searched without success for CaF toward the C-rich AGB star IRC +10216. Our chemical equilibrium calculations (see the third panel in Fig. A.7) indicate that CaF only reaches non-negligible abundances in O-rich atmospheres.

The trace metals Ba, Sc, Zr, and V form some molecules, mainly oxides, that might be detectable through their rotational spectrum in oxygen-rich atmospheres because they are predicted to have mole fractions in the range  $10^{-10}$ - $10^{-8}$  and have fairly high dipole moments. These molecules are BaO, BaS, ScO, ScO<sub>2</sub>, ZrO, ZrO<sub>2</sub>, VO, and VO<sub>2</sub>. Some of them, such as ZrO and VO, have long been known to be present in the atmospheres of S- and M-type AGB stars from observations at optical and near-infrared wavelengths (Keenan & Schroeder 1952; Keenan 1954; Joyce et al. 1998), and various absorption bands in the spectra of S-type stars have been assigned to BaO by Dubois (1977). Moreover, ScO has been observed in the optical spectrum of V1309 Sco, a remnant of a stellar merger whose conditions resemble those of AGB outflows (Kamiński et al. 2015). However, these oxides (BaO, ScO, ZrO, and VO) have not yet been detected through their rotational spectrum, which would allow us to derive their abundances. Other molecules, such as BaCl<sub>2</sub>, Sc<sub>2</sub>O, Sc<sub>2</sub>O<sub>2</sub>, and ZrCl<sub>2</sub>, only reach mole fractions of about  $10^{-10}$  at large radii ( $\sim 10 R_*$ ) in certain AGB atmospheres, although in this region it is more uncertain that chemical equilibrium prevails. The vanadium-oxygen cluster V<sub>4</sub>O<sub>10</sub> is predicted to be the main carrier of V in oxygen-rich atmospheres beyond  $\sim 7 R_*$  (see the bottom panel in Fig. A.8). However, this highly symmetric cluster is predicted to be nonpolar according to quantum-chemical calculations at the B3LYP/cc-pVTZ + PP for V level and thus cannot be observed through its rotational spectrum. The large titanium-carbon cluster Ti<sub>8</sub>C<sub>12</sub> is predicted to lock most of the titanium in S- and C-type atmospheres beyond 2-3  $R_*$  (see the second panel in Fig. A.8). However, its large size is a handicap for detecting it through its rotational spectrum, which is likely to be crowded by lines so that spectral dilution is a serious problem.

Three Cr-bearing molecules (CrS, CrO, and CrCl) are potentially detectable in AGB stars. Although chromium is mostly in

atomic form, these molecules are predicted with mole fractions in the range  $10^{-10}$ - $10^{-9}$  in M-type atmospheres, and all of them have quite high dipole moments. CrO has been observed in the optical toward the stellar-merger remnant V1309 Sco, an object where other oxides such as TiO, VO, ScO, and AlO have also been found (Kamiński et al. 2015). These observations support that CrO can plausibly be detected at radio wavelengths in O-rich AGB stars.

The metal transition hydrides MnH and CoH are also in the list of potentially detectable molecules. Chemical equilibrium predicts that MnH is present with a uniform mole fraction of  $\sim 10^{-10}$  in AGB atmospheres, regardless of the C/O (see the second panel in Fig. A.9). The high dipole moment of MnH (10.65 D; Koseki et al. 2006) can help to detect it. The dipole moment is lower for CoH (1.88 D; Wang et al. 2009), but this hydride is predicted to be the main carrier of Co in AGB atmospheres of any chemical type and is therefore expected to be present with a fairly large abundance. Although there is certainly a problem of incompleteness in the Co-bearing molecules included in the calculations, which might affect the predicted abundance of CoH (see Sec. A.13), this molecule is a very interesting target for future searches in AGB atmospheres when the rotational spectrum is measured in the laboratory.

Iron and nickel are, as many other transition metals, predicted to be mostly in the form of neutral atoms. However, in O-rich atmospheres, the sulfides FeS and NiS reach relatively high mole fractions (up to  $\sim 4 \times 10^{-8}$  and  $\sim 4 \times 10^{-7}$ , respectively), which together with the high dipole moments of these molecules make them attractive candidates for detection. Iron monoxide (FeO) is also calculated with a non-negligible mole fraction (up to  $\sim 3 \times 10^{-10}$ ) in M-type atmospheres, and thus could be detectable given its high dipole moment. A claim of detection of FeO in the oxygen-rich AGB star R Dor has recently been made using ALMA (Decin et al. 2018b). The inferred abundance relative to H<sub>2</sub> is a few times  $10^{-8}$ , about two orders of magnitude above the predictions of chemical equilibrium. Further observations are required to unambiguously establish the presence of FeO and derive its abundance. The molecule Fe(OH)<sub>2</sub> is predicted to have a rising abundance with increasing radius, reaching a mole fraction of  $\sim 10^{-8}$  at  $10 R_*$  (see the third panel in Fig. A.9). However, this molecule is predicted to have a linear O-Fe-O structure, and thus probably has a very low dipole moment (Wang & Andrews 2006).

## 5. Condensates

### 5.1. Observational constraints

It is well known that solid dust grains are formed in AGB atmospheres, and that the later ejection of this material into the interstellar medium constitutes the main source of interstellar dust in the Galaxy (Gehrz 1989). Infrared observations have allowed us to identify a few solid compounds in AGB envelopes, although the identification of some of them is still under discussion (see reviews by Molster et al. 2010 and Waters 2011). The observational situation of condensates identified in AGB envelopes is summarized in Table 4.

The dust in oxygen-rich AGB envelopes is mainly composed of silicates and oxides. Amorphous silicate is widely observed through the 9.7  $\mu\text{m}$  band, and crystalline silicates of the families of olivine (Mg<sub>(2-2x)</sub>Fe<sub>2x</sub>SiO<sub>4</sub>) and pyroxene (Mg<sub>(1-x)</sub>Fe<sub>x</sub>SiO<sub>3</sub>) have also been identified through narrow bands at mid- and far-infrared wavelengths (Waters et al. 1996; Blommaert et al. 2014). Alumina (Al<sub>2</sub>O<sub>3</sub>), a highly refractory condensate, is

**Table 4.** Condensates identified in AGB dust.

Condensate	Identification	
	M stars	
Amorphous silicate	IR	Woolf & Ney (1969)
Crystalline silicates		
Olivine ( $\text{Mg}_{(2-2x)}\text{Fe}_{2x}\text{SiO}_4$ )	IR	Waters et al. (1996)
Pyroxene ( $\text{Mg}_{(1-x)}\text{Fe}_x\text{SiO}_3$ )	IR	Waters et al. (1996)
Alumina ( $\text{Al}_2\text{O}_3$ )	IR	Onaka et al. (1989)
	PM	Nittler et al. (1994)
		Hutcheon et al. (1994)
$\text{Mg}_{(1-x)}\text{Fe}_x\text{O}$ with $x=0.9$	IR	Posch et al. (2002)
Spinel ( $\text{MgAl}_2\text{O}_4$ )	IR ?	Posch et al. (1999)
	PM	Nittler et al. (1997)
Hibonite ( $\text{CaAl}_2\text{O}_9$ )	PM	Choi et al. (1999)
Gehlenite ( $\text{Ca}_2\text{Al}_2\text{SiO}_7$ )	IR ?	Heras & Hony (2005)
Fe	IR ?	Kemper et al. (2002)
	C stars	
Amorphous carbon	IR	Martin & Rogers (1987)
Graphite	PM	Amari et al. (1990)
SiC	IR	Treffers & Cohen (1974)
	PM	Bernatowicz et al. (1987)
MgS	IR	Goebel & Moseley (1985)
TiC	PM	Bernatowicz et al. (1991)
	S stars	
MgS	IR	Hony et al. (2009)
Amorphous silicate	IR ?	Hony et al. (2009)
Alumina ( $\text{Al}_2\text{O}_3$ )	IR ?	Smolders et al. (2012)
Diopside ( $\text{MgCaSi}_2\text{O}_6$ )	IR ?	Hony et al. (2009)
Gehlenite ( $\text{Ca}_2\text{Al}_2\text{SiO}_7$ )	IR ?	Smolders et al. (2012)

Notes: IR indicates identification through infrared observations, while PM stands for identification in presolar material from meteorites. A question mark indicates that the identification is not completely secure.

also observed at infrared wavelengths (Onaka et al. 1989) and has also been identified in presolar grains (Nittler et al. 1994; Hutcheon et al. 1994). There is also evidence of Mg-Fe oxides of the type  $\text{Mg}_{1-x}\text{Fe}_x\text{O}$ , with a high content of Fe (Posch et al. 2002). Another condensate that is highly refractory is hibonite ( $\text{CaAl}_2\text{O}_9$ ), which has been identified in presolar grains (Choi et al. 1999). Spinel ( $\text{MgAl}_2\text{O}_4$ ) has been proposed as a constituent of dust in O-rich envelopes (Posch et al. 1999), although the identification has been questioned (DePew et al. 2006; Zeidler et al. 2013). Further evidence for the presence of spinel comes from the analysis of presolar grains in meteorites (Nittler et al. 1997). Heras & Hony (2005) found evidence of gehlenite ( $\text{Ca}_2\text{Al}_2\text{SiO}_7$ ) based on modeling the spectral energy distribution of 28 O-rich AGB stars in the 2.4–45.2  $\mu\text{m}$  range. The presence of metallic iron grains has been also inferred in the oxygen-rich envelope OH 127.8+0.0 (Kemper et al. 2002). However, the identification is particularly uncertain because Fe lacks spectral features and it is only recognized by an excess of opacity in 3–8  $\mu\text{m}$  range.

In carbon-rich AGB envelopes, dust is mostly composed of carbon, either amorphous or in the form of graphite. These two materials do not have spectral features but provide a smooth continuum at infrared wavelengths. Martin & Rogers (1987) modeled the spectral energy distribution of the prototypical carbon star IRC +10216 and found that amorphous carbon, rather than graphite, is the main form of carbonaceous dust in C-rich envelopes. Graphite must also be present to some extent because it has been identified in presolar meteoritic material, with isotopic ratios pointing to formation in the outflows of C-rich AGB stars (Amari et al. 1990). Silicon carbide (SiC) dust is widely identified toward C stars through a band centered at 11.3  $\mu\text{m}$

(Treffers & Cohen 1974), and presolar SiC grains have also been identified in carbonaceous meteorites (Bernatowicz et al. 1987). Goebel & Moseley (1985) proposed MgS as the carrier of a band observed at 30  $\mu\text{m}$ . The assignment to MgS has been disputed by Zhang et al. (2009), who argued that the amount of MgS required to reproduce the observed band strength implies a sulfur abundance higher than solar. This problem vanishes if MgS is only present in the outer layers of the grains (Lombaert et al. 2012), as originally proposed by Zhukovska & Gail (2008). Currently, MgS remains the best candidate for the 30  $\mu\text{m}$  feature (Sloan et al. 2014). Finally, there is strong evidence of the presence of TiC in grains formed in C-rich AGB ejecta from the analysis of presolar material in meteorites (Bernatowicz et al. 1991).

The chemical composition of dust around S stars appears to contain features of both O-rich and C-rich stars. The study of Hony et al. (2009) revealed the 30  $\mu\text{m}$  band, which is attributable to MgS, the amorphous silicate band, which appears shifted from 9.7  $\mu\text{m}$  to redder wavelengths, however, and is proposed to be due to non-stoichiometric silicates and a series of emission bands in the 20–40  $\mu\text{m}$  that were tentatively assigned to diopside ( $\text{MgCaSi}_2\text{O}_6$ ). The presence of alumina ( $\text{Al}_2\text{O}_3$ ) and gehlenite ( $\text{Ca}_2\text{Al}_2\text{SiO}_7$ ) was also inferred by Smolders et al. (2012) by modeling the spectral energy distribution of a large sample of S stars.

## 5.2. Expectations from chemical equilibrium

Chemical equilibrium calculations can be very informative on the types of condensates that are expected to form in AGB atmospheres and on the sequence in which they are expected to appear (Sharp et al. 1995; Lodders & Fegley 1997, 1999; Gail & Sedlmayr 2013). Our main motivation to revisit the subject here is twofold. First, we aim to cross-check our calculations against previously published results. Second, we seek to establish a condensation sequence in M-, S-, and C-type atmospheres using a realistic pressure-temperature profile that serves us as starting point to discuss the most likely gas-phase precursors of selected condensates.

Here we present results from chemical equilibrium calculations in which condensates are considered. We collected thermochemical data for 185 condensed species. If all condensates are included simultaneously in the calculations, when multiple condensates having elements in common are thermodynamically favorable, only the most stable ones form at the expense of others that may never become abundant because their constituent elements are trapped by other more stable compounds. To circumvent this problem of competition between condensates with elements in common, calculations were run including only one condensed species each time. This allowed us to have a complete condensation sequence, without missing condensates, and to compare with previously published condensation sequences. For these calculations, we adopted the elemental composition given in Table 1 and the pressure-temperature profile discussed in Sec. 2.4.

Carbonaceous dust in C-rich envelopes is expected to be mostly in the form of amorphous carbon (Martin & Rogers 1987). However, thermochemical data are not available for amorphous carbon, and we therefore used graphite as a proxy. Similarly, no thermochemical data for amorphous silicates or crystalline silicates with varying Mg/Fe, which are observed in O-rich envelopes (Woolf & Ney 1969; Waters et al. 1996), are available. Therefore, forsterite ( $\text{Mg}_2\text{SiO}_4$ ) and enstatite ( $\text{MgSiO}_3$ ) were used in the chemical equilibrium calculations as proxies of olivine, pyroxene, and amorphous silicate. Similarly,

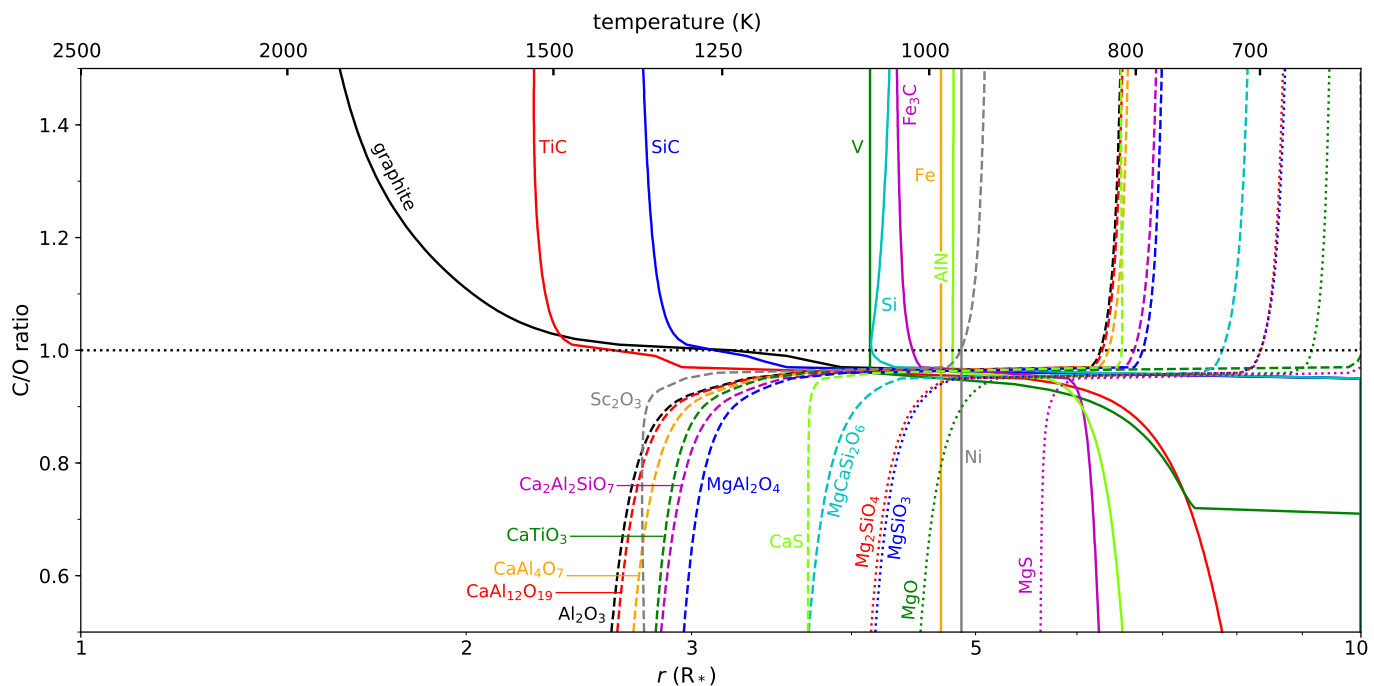


**Fig. 5.** Radius (bottom  $x$ -axis) and temperature (top  $x$ -axis) at which some relevant condensates are predicted to appear in AGB atmospheres are shown as a function of the C/O ( $y$ -axis).

we lack thermochemical data for the Mg-Fe oxide  $\text{Mg}_{0.1}\text{Fe}_{0.9}\text{O}$  identified in M stars. Nevertheless, the oxides MgO and FeO were included, and the latter was used as a proxy of  $\text{Mg}_{0.1}\text{Fe}_{0.9}\text{O}$ . We note, however, that there might be significant differences between the thermochemical properties of amorphous carbon and graphite, amorphous silicates and crystalline forsterite and enstatite, and  $\text{Mg}_{0.1}\text{Fe}_{0.9}\text{O}$  and FeO, which might lead to some changes in the condensation sequence calculated here for M-, S-, and C-type atmospheres.

Results from the chemical equilibrium calculations regarding condensates are shown in Fig. 5 and Fig. 6, where we show the radius (bottom  $x$ -axis) and temperature (top  $x$ -axis) at which each condensate appears. In Fig. 5 the condensation radius (and temperature) of some relevant condensates is shown as a function of the C/O ( $y$ -axis). In Fig. 6 we show all the condensates that appear in the 1-10  $R_*$  range in M- and C-type atmospheres on an abundance scale ( $y$ -axis). The abundance scale is given by the maximum mass ratio relative to H that each condensate may attain, according to the abundances of its constituent elements (see Table 1). This is to be compared with the typical dust-to-gas mass ratios derived in AGB envelopes, in the range  $(1-4) \times 10^{-3}$  (Ramstedt et al. 2008), and is indicated by a gray horizontal band in Fig. 6. This shows that condensates with maximum attainable mass ratios close to  $10^{-3}$  can be main constituents of dust, while those for which the maximum attainable mass ratio is substantially lower than  $10^{-3}$  can only be minor components of circumstellar dust. Still, minor condensates might be very important if they are predicted to be among the first condensates, in which case they can serve as condensation nuclei and accelerate the condensation of other compounds.

Chemical equilibrium predicts that the first condensates in carbon-rich atmospheres should be carbon, followed by TiC, and then SiC, while in oxygen-rich atmospheres  $\text{Al}_2\text{O}_3$  should be the first condensate to appear, followed by minerals such as hibonite ( $\text{CaAl}_{12}\text{O}_{19}$ ), grossite ( $\text{CaAl}_4\text{O}_7$ ), scandia ( $\text{Sc}_2\text{O}_3$ ), perovskite ( $\text{CaTiO}_3$ ), gehlenite ( $\text{Ca}_2\text{Al}_2\text{SiO}_7$ ), and spinel ( $\text{MgAl}_2\text{O}_4$ ). How-

ever, these conclusions change for C-to-O ratios close to one (see Fig. 5). For example, the condensation sequence C-TiC-SiC changes to TiC-C-SiC for C/O below 1.02, and to TiC-SiC-C for even lower C/O, in the range 0.96-1.00. These values hold for the specific pressure-temperature profile adopted here, which yields pressures between a few  $10^{-10}$  and  $10^{-8}$  bar in the region where these compounds are expected to condense (see Fig. 1). For higher pressures, the C-to-O ratios that separate the different condensation sequences shift to higher values. For example, at pressures of  $10^{-6}$ - $10^{-5}$  bar, TiC condenses before carbon if  $\text{C/O} < 1.1$  (Lodders & Fegley 1997). Evidence of TiC serving as nucleation site for carbon dust has been found from the analysis of presolar grains (Bernatowicz et al. 1991, 1996), which implies formation at low C-to-O ratios and/or high pressures (Lodders & Fegley 1997). In oxygen-rich atmospheres with C/O in the range 0.82-0.96,  $\text{Sc}_2\text{O}_3$ , rather than  $\text{Al}_2\text{O}_3$ , is predicted to be the first condensate. Although  $\text{Sc}_2\text{O}_3$  can only be a minor condensate because the elemental abundance of Sc is low (see the upper panel in Fig. 6), it may provide the condensation nuclei for oxides and silicates. Therefore, depending on the C/O, either carbon, TiC,  $\text{Sc}_2\text{O}_3$ , or  $\text{Al}_2\text{O}_3$  would be the first condensate according to chemical equilibrium. Lodders & Fegley (1999) reported that highly refractory condensates involving trace elements such as Hf and Zr are also likely to serve as condensation nuclei. Concretely, these authors mentioned  $\text{HfO}_2$  and  $\text{ZrO}_2$  in O-rich atmospheres and ZrC in C-rich stars. These condensates are not included in our calculations. Despite the low elemental abundance of Zr, there is evidence for ZrC in presolar grains (Bernatowicz et al. 1996). Therefore it would not be surprising if other highly refractory condensates involving trace elements such as  $\text{Sc}_2\text{O}_3$  might also be identified in presolar grains.

It is worth noting that for slightly oxygen-rich conditions ( $\text{C/O} = 0.96$ -1.00), our calculations predict that condensates typical of carbon-rich conditions, such as TiC, SiC, and carbon, form well before minerals typical of oxygen-rich conditions, such as oxides and silicates (see Fig. 5). This behavior recalls

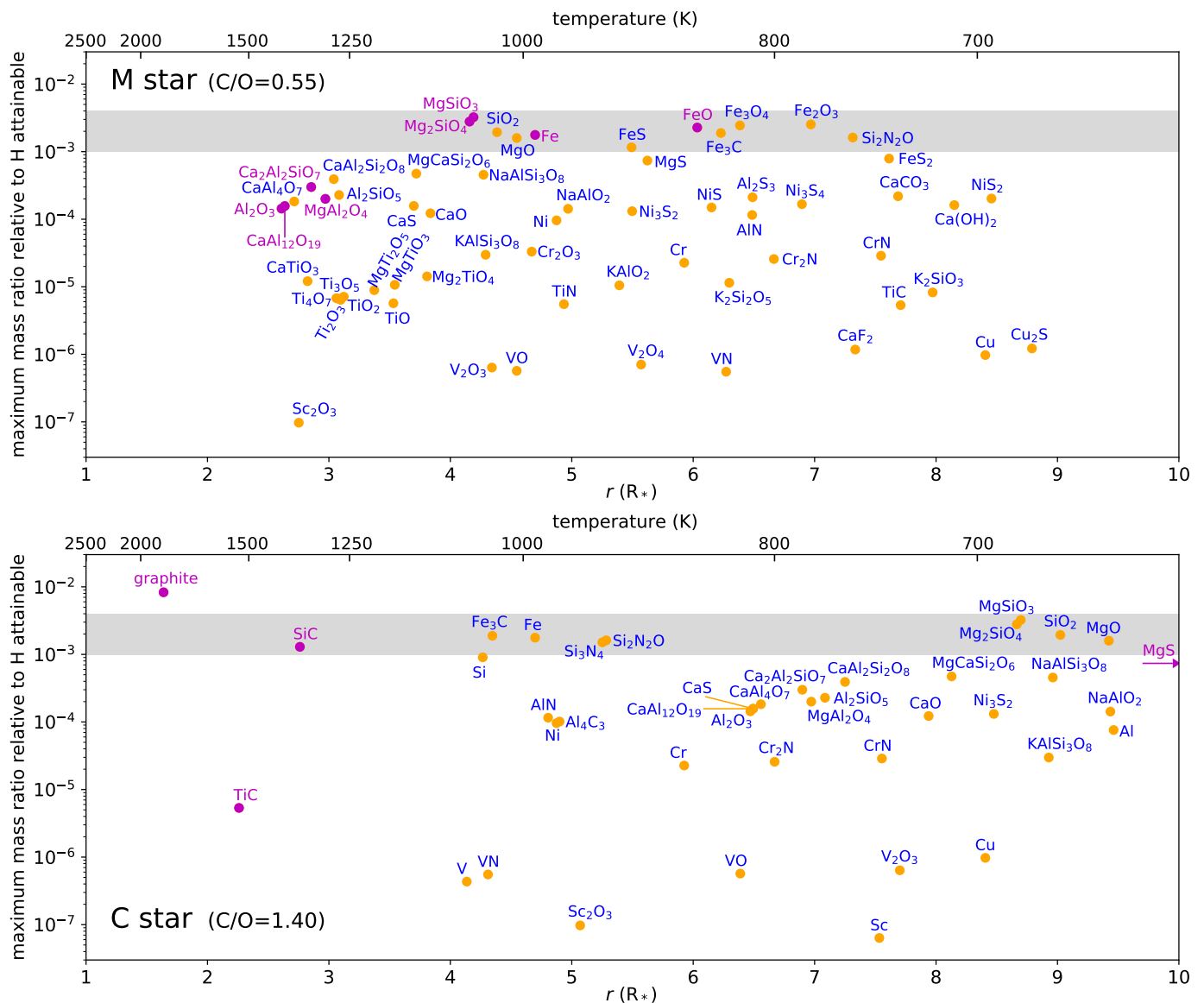


**Fig. 6.** All condensates predicted to appear in the 1-10  $R_*$  range in atmospheres of M- and C-type AGB stars (upper and lower panels, respectively). Condensates are located in the diagrams according to their condensation radius (bottom x-axis; the corresponding temperature is given in the top x-axis) and maximum mass ratio relative to H attainable. Condensates observed in AGB envelopes (see Table 4) are indicated in magenta. The range of dust-to-gas mass ratios derived by Ramstedt et al. (2008) for envelopes of AGB stars is indicated by a gray horizontal band. In C-type AGB atmospheres, MgS is predicted to condense at temperatures below 628 K (see Table 5), i.e., beyond 10  $R_*$ .

that found previously for gas-phase molecules (see Sec. 3.3). That is, for slightly oxygen-rich conditions, the chemical composition shares more features with a carbon-rich mixture than with an oxygen-rich one, and this applies to both gaseous species and condensates. This conclusion has direct consequences for S-type stars. For example, the predicted condensation sequence for an S-type atmosphere with  $C/O = 1$  resembles that of a carbon-rich star far more than that of an M-type atmosphere (see Fig. 5).

Our calculations indicate that dust is expected to form very close to the star, at 1-3  $R_*$ . Near-infrared polarimetric interferometric observations of R Dor and W Hya found that dust is already present as close to the star as 1.3-1.5  $R_*$  (Khouri et al. 2016; Ohnaka et al. 2017). The calculations also predict that carbon dust in C-rich atmospheres forms closer to the star than alumina dust in O-rich stars. Similarly, in S-type stars, condensation is shifted to slightly larger radii than in O- and C-rich stars.

The limited observational constraints on the composition of dust in AGB envelopes is roughly consistent with the expectations from chemical equilibrium. In the case of M-type stars (see Table 4 and the upper panel in Fig. 6), observations indicate that the bulk of grains is composed of Mg-Fe silicates, which is consistent with the fact that MgSiO<sub>3</sub> and Mg<sub>2</sub>SiO<sub>4</sub> are the first condensates of those that can attain dust-to-gas mass ratios higher than 10<sup>-3</sup>. The detection of Al<sub>2</sub>O<sub>3</sub>, MgAl<sub>2</sub>O<sub>4</sub>, and CaAl<sub>12</sub>O<sub>19</sub> and the possible presence of Ca<sub>2</sub>Al<sub>2</sub>SiO<sub>7</sub> are also in line with expectations from chemical equilibrium. These are among the first condensates predicted to appear, and all of them may attain moderately high dust-to-gas mass ratios higher than 10<sup>-4</sup>. In C-type stars (see Table 4 and the lower panel in Fig. 6), amorphous carbon and SiC are the main constituents of grains according to observations, and this is also in line with the predictions from chemical equilibrium, which clearly indicate that these two compounds are the first main condensates. In the case of S-type stars,

**Table 5.** Condensates of each element in M and C stars.

Element <sup>a</sup>	M stars			C stars		
	Condensate	$f_{el}^b$ (%)	$T_c^c$ (K)	Condensate	$f_{el}^b$ (%)	$T_c^c$ (K)
Mg 7.60	<b>MgAl<sub>2</sub>O<sub>4</sub></b>	4	1301	MgAl <sub>2</sub> O <sub>4</sub>	4	780
	MgCaSi <sub>2</sub> O <sub>6</sub>	5	1137	MgCaSi <sub>2</sub> O <sub>6</sub>	5	711
	<b>Mg<sub>2</sub>SiO<sub>4</sub></b>	100	1063	Mg <sub>2</sub> SiO <sub>4</sub>	100	684
	<b>MgSiO<sub>3</sub></b>	81	1058	MgSiO <sub>3</sub>	81	683
	MgO	100	1008	MgO	100	651
	MgS	33	887	<b>MgS</b>	33	< 628
Si 7.51	<b>Ca<sub>2</sub>Al<sub>2</sub>SiO<sub>7</sub></b>	3	1332	<b>SiC</b>	100	1359
	CaAl <sub>2</sub> Si <sub>2</sub> O <sub>8</sub>	14	1283	Si	100	1047
	Al <sub>2</sub> SiO <sub>5</sub>	4	1272	Si <sub>3</sub> N <sub>4</sub>	100	924
	MgCaSi <sub>2</sub> O <sub>6</sub>	14	1137	Si <sub>2</sub> N <sub>2</sub> O	100	921
	<b>Mg<sub>2</sub>SiO<sub>4</sub></b>	62	1063	Ca <sub>2</sub> Al <sub>2</sub> SiO <sub>7</sub>	3	785
	<b>MgSiO<sub>3</sub></b>	100	1058	Al <sub>2</sub> SiO <sub>5</sub>	4	772
	NaAlSi <sub>3</sub> O <sub>8</sub>	16	1046	CaAl <sub>2</sub> Si <sub>2</sub> O <sub>8</sub>	14	762
	SiO <sub>2</sub>	100	1030	MgCaSi <sub>2</sub> O <sub>6</sub>	14	711
	Si <sub>2</sub> N <sub>2</sub> O	100	758	Mg <sub>2</sub> SiO <sub>4</sub>	62	684
				MgSiO <sub>3</sub>	100	683
				NaAlSi <sub>3</sub> O <sub>8</sub>	16	671
Fe 7.50	<b>Fe</b>	100	988	Fe <sub>3</sub> C	100	1035
	FeS	42	900	Fe	100	988
	<b>FeO</b>	100	850			
	Fe <sub>3</sub> C	100	834			
	Fe <sub>3</sub> O <sub>4</sub>	100	822			
	Fe <sub>2</sub> O <sub>3</sub>	100	780			
	FeS <sub>2</sub>	21	740			
S 7.12	CaS	17	1140	CaS	17	814
	FeS	100	900	Ni <sub>3</sub> S <sub>2</sub>	8	693
	Ni <sub>3</sub> S <sub>2</sub>	8	899	<b>MgS</b>	100	< 628
	MgS	100	887			
	NiS	13	841			
	Al <sub>2</sub> S <sub>3</sub>	32	814			
	Ni <sub>3</sub> S <sub>4</sub>	17	785			
	FeS <sub>2</sub>	100	740			
	NiS <sub>2</sub>	25	694			
Al 6.45	<b>Al<sub>2</sub>O<sub>3</sub></b>	100	1406	AlN	100	975
	<b>CaAl<sub>12</sub>O<sub>19</sub></b>	100	1397	Al <sub>4</sub> C <sub>3</sub>	100	964
	CaAl <sub>4</sub> O <sub>7</sub>	100	1373	Al <sub>2</sub> O <sub>3</sub>	100	815
	<b>Ca<sub>2</sub>Al<sub>2</sub>SiO<sub>7</sub></b>	78	1332	CaAl <sub>12</sub> O <sub>19</sub>	100	814
	<b>MgAl<sub>2</sub>O<sub>4</sub></b>	100	1301	CaAl <sub>4</sub> O <sub>7</sub>	100	809
	CaAl <sub>2</sub> Si <sub>2</sub> O <sub>8</sub>	100	1283	Ca <sub>2</sub> Al <sub>2</sub> SiO <sub>7</sub>	78	785
	Al <sub>2</sub> SiO <sub>5</sub>	100	1272	MgAl <sub>2</sub> O <sub>4</sub>	100	780
	NaAlSi <sub>3</sub> O <sub>8</sub>	62	1046	Al <sub>2</sub> SiO <sub>5</sub>	100	772
	KAlSi <sub>3</sub> O <sub>8</sub>	4	1043	CaAl <sub>2</sub> Si <sub>2</sub> O <sub>8</sub>	100	762
	NaAlO <sub>2</sub>	62	955	KAlSi <sub>3</sub> O <sub>8</sub>	4	672
	KAlO <sub>2</sub>	4	910	NaAlSi <sub>3</sub> O <sub>8</sub>	62	671
	AlN	100	814	NaAlO <sub>2</sub>	62	650
	Al <sub>2</sub> S <sub>3</sub>	100	814	Al	100	649
Ca 6.34	<b>CaAl<sub>12</sub>O<sub>19</sub></b>	11	1397	CaS	100	814
	CaAl <sub>4</sub> O <sub>7</sub>	32	1373	CaAl <sub>12</sub> O <sub>19</sub>	11	814
	CaTiO <sub>3</sub>	4	1341	CaAl <sub>4</sub> O <sub>7</sub>	32	809
	<b>Ca<sub>2</sub>Al<sub>2</sub>SiO<sub>7</sub></b>	100	1332	Ca <sub>2</sub> Al <sub>2</sub> SiO <sub>7</sub>	100	785
	CaAl <sub>2</sub> Si <sub>2</sub> O <sub>8</sub>	64	1283	CaAl <sub>2</sub> Si <sub>2</sub> O <sub>8</sub>	64	762
	CaS	100	1140	CaO	100	721
	MgCaSi <sub>2</sub> O <sub>6</sub>	100	1137	MgCaSi <sub>2</sub> O <sub>6</sub>	100	711
	CaO	100	1116			
	CaCO <sub>3</sub>	100	735			
	Ca(OH) <sub>2</sub>	100	710			

observations seem to indicate a chemical composition of dust that is more similar to that of O-rich stars, with the exception of MgS (see Table 4), while chemical equilibrium favors a dust composition that is more carbon-rich-like (see Fig. 5). We note, however, that the comparison between observations and chemical equilibrium for S stars is difficult because on the one hand,

**Table 5.** Continued.

Element <sup>a</sup>	M stars			C stars		
	Condensate	$f_{el}^b$ (%)	$T_c^c$ (K)	Condensate	$f_{el}^b$ (%)	$T_c^c$ (K)
Na 6.24	NaAlSi <sub>3</sub> O <sub>8</sub>	100	1046	NaAlSi <sub>3</sub> O <sub>8</sub>	100	671
	NaAlO <sub>2</sub>	100	955	NaAlO <sub>2</sub>	100	650
Ni 6.22	Ni	100	966	Ni	100	966
	Ni <sub>3</sub> S <sub>2</sub>	100	899	Ni <sub>3</sub> S <sub>2</sub>	100	693
	NiS <sub>2</sub>	100	694			
Cr 5.64	Cr <sub>2</sub> O <sub>3</sub>	100	992	Cr	100	860
	Cr	100	860	Cr <sub>2</sub> N	100	801
	Cr <sub>2</sub> N	100	801	CrN	100	743
	CrN	100	743			
K 5.03	KAlSi <sub>3</sub> O <sub>8</sub>	100	1043	KAlSi <sub>3</sub> O <sub>8</sub>	100	672
	KAlO <sub>2</sub>	100	910			
	K <sub>2</sub> Si <sub>2</sub> O <sub>5</sub>	100	829			
	K <sub>2</sub> SiO <sub>3</sub>	100	719			
Ti 4.95	CaTiO <sub>3</sub>	100	1341	<b>TiC</b>	100	1539
	Ti <sub>4</sub> O <sub>7</sub>	100	1278			
	Ti <sub>3</sub> O <sub>5</sub>	100	1273			
	Ti <sub>2</sub> O <sub>3</sub>	100	1269			
	TiO <sub>2</sub>	100	1263			
	MgTi <sub>2</sub> O <sub>5</sub>	100	1205			
	TiO	100	1173			
	MgTiO <sub>3</sub>	100	1170			
	Mg <sub>2</sub> TiO <sub>4</sub>	100	1121			
	TiN	100	959			
	TiC	100	734			
Cu 4.19	Cu	100	697	Cu	100	697
	Cu <sub>2</sub> S	100	679			
V 3.93	V <sub>2</sub> O <sub>3</sub>	100	1036	V	100	1067
	VO	100	1008	VN	100	1041
	V <sub>2</sub> O <sub>4</sub>	100	892	VO	100	822
	VN	100	831	V <sub>2</sub> O <sub>3</sub>	100	735
Sc 3.15	Sc <sub>2</sub> O <sub>3</sub>	100	1362	Sc <sub>2</sub> O <sub>3</sub>	100	944
				Sc	100	744

Notes:

Condensates observed in AGB stars (see Table 4) are highlighted in magenta.

<sup>a</sup> Element and abundance log  $\epsilon$ , defined as  $\log \epsilon(X) = 12 + \log(X/H)$ .

<sup>b</sup> Maximum fraction of elements that can be trapped by condensate.

<sup>c</sup> Condensation temperature.

observational constraints are more uncertain, and on the other, the predicted condensation sequence is extremely sensitive to the exact C/O.

Table 5 presents similar information to that shown in Fig. 6, but in a different manner. We list in order of appearance the condensates that are expected to trap each refractory element in M- and C-type atmospheres. The table also lists the maximum fraction of the element that each condensate can trap and the corresponding condensation temperature. In the main, the solid reservoirs of each element identified in M- and C-type atmospheres are similar to those presented by Lodders & Fegley (1999) in their Table 1, although there are some differences, which probably arise from differences in the thermochemical database of condensates and in the pressures and C-to-O ratios involved in the calculations. We now discuss each element individually, guided by Table 5.

*Magnesium.* The first Mg condensate expected in M-type atmospheres is spinel (MgAl<sub>2</sub>O<sub>4</sub>), for which there is evidence from infrared observations (Posch et al. 1999) and analysis of presolar grains (Nittler et al. 1997). Spinel cannot be a main reservoir of Mg, however, because it can only trap a small fraction of Mg (up to 4 %) because the abundance of Al is lower. The

next Mg condensate predicted is diopside ( $\text{MgCaSi}_2\text{O}_6$ ), which has tentatively been identified in S-type stars (Hony et al. 2009), but not in O-rich envelopes. The presence of diopside in M-type envelopes, which would only trap as much as 5 % of Mg, depends on whether some Ca is left after condensation of more refractory Ca compounds, such as  $\text{CaTiO}_3$ ,  $\text{Ca}_2\text{Al}_2\text{SiO}_7$ , and  $\text{CaAl}_2\text{Si}_2\text{O}_8$ . Next in the condensation sequence of Mg, we have forsterite ( $\text{Mg}_2\text{SiO}_4$ ) and enstatite ( $\text{MgSiO}_3$ ), the Mg-rich end members of the olivine and pyroxene families,  $\text{Mg}_{(2-2x)}\text{Fe}_{2x}\text{SiO}_4$  and  $\text{Mg}_{(1-x)}\text{Fe}_x\text{SiO}_3$ , respectively, which are expected to be main reservoirs of Mg, in agreement with observations (Molster et al. 2002). There is evidence of Mg in the form of  $\text{Mg}_{0.1}\text{Fe}_{0.9}\text{O}$  (Posch et al. 2002), which according to the condensation temperatures of MgO and FeO, should form from the Mg that is left after condensation of Mg-rich silicates. MgS is predicted to condense at even farther distances than MgO, and therefore little Mg is expected to be available to form it. In C-rich atmospheres, MgS is predicted to form at even larger distances from the star, beyond  $10 R_*$  (at temperatures below 628 K) for our radial pressure and temperature profiles. The lower condensation temperature of MgS in C-rich atmospheres, compared to O-rich ones, is related to the different main gaseous reservoirs of sulfur in these two types of sources (SiS in C-rich atmospheres and  $\text{H}_2\text{S}$  in O-rich ones), which compete differently with solid MgS for the sulfur. In spite of the large condensation radius of MgS in C-rich sources, this is the only Mg condensate identified so far in C-rich ejecta (Goebel & Moseley 1985). Several O-containing Mg condensates are predicted to appear earlier than MgS in C-rich atmospheres (see Table 5). Their formation must therefore be inhibited either by the difficulty of competing for the oxygen, or because more refractory compounds would have trapped most of the Si, Al, and Ca. The formation of MgS at large distances from the AGB star, although somewhat surprising, is consistent with its presence in the outer layers of preexisting grains (Zhukovska & Gail 2008; Lombaert et al. 2012). There is evidence that CS act as gas-phase precursor of MgS dust in high mass-loss rate C-rich envelopes, as indicated by the decrease in its fractional abundance with increasing envelope density and with increasing flux of the  $30 \mu\text{m}$  feature attributed to MgS dust (Massalkhi et al. 2019). However, in some C-rich envelopes, gaseous CS and SiS trap most of the sulfur (Danilovich et al. 2018; Massalkhi et al. 2019), so that little would be left to form MgS dust.

**Silicon.** In O-rich ejecta, silicon is predicted to condense first in the form of various Ca- and Al-containing silicates: gehlenite ( $\text{Ca}_2\text{Al}_2\text{SiO}_7$ ), anorthite ( $\text{CaAl}_2\text{Si}_2\text{O}_8$ ), andalusite ( $\text{Al}_2\text{SiO}_5$ ), and diopside ( $\text{MgCaSi}_2\text{O}_6$ ), although these can only take a small fraction of the silicon. Among them, there is only a tentative identification of the first expected condensate, gehlenite (Heras & Hony 2005), but no observational indication of the others. Clearly, the first main Si condensates are forsterite ( $\text{Mg}_2\text{SiO}_4$ ) and enstatite ( $\text{MgSiO}_3$ ). Silica ( $\text{SiO}_2$ ) might also be an important reservoir of Si because it is predicted to condense at only slightly lower temperatures than forsterite and enstatite. In C-rich atmospheres, the first and main Si condensate is clearly SiC, for which there is evidence from both infrared observations and analysis of presolar grains (Treffers & Cohen 1974; Bernatowicz et al. 1987). Other main Si condensates are pure Si,  $\text{Si}_3\text{N}_4$ , and  $\text{Si}_2\text{N}_2\text{O}$ , although they have much lower condensation temperatures.

**Iron.** Metallic iron is predicted to condense at a temperature of 988 K independently of the C/O. In M-type atmospheres, this would be the first and main solid reservoir of the element, which is consistent with the inference of Fe grains from the modeling of the spectral energy distribution of the O-rich star OH 127.8+0.0

(Kemper et al. 2002). Metallic iron is expected to condense after silicates. Other Fe condensates such as sulfides, oxides, and carbides (see Table 5) can form later from the Fe that is left after condensation of pure iron. The detection of  $\text{Mg}_{0.1}\text{Fe}_{0.9}\text{O}$  (Posch et al. 2002) is an indication of this. A potentially important reservoir of iron is troilite ( $\text{FeS}$ ), which is predicted to condense at slightly higher temperatures than FeO. In C-rich envelopes, most iron is expected to be in the form of  $\text{Fe}_3\text{C}$  because this carbide is predicted to condense earlier than pure Fe. Lodders & Fegley (1999) found that  $(\text{Fe,Ni})_3\text{P}$  and FeSi might also be important Fe condensates in O-rich and C-rich, respectively, atmospheres.

**Sulfur.** The first S-containing condensate expected in both M- and C-type atmospheres is CaS. This compound, which would condense at a significantly higher temperature in O-rich atmospheres than in C-rich conditions, can take up to 17% of the sulfur. Depending on the degree of depletion of this element from the gas phase, other S-containing condensates may form, such as FeS and  $\text{Ni}_3\text{S}_2$  in M-type atmospheres and  $\text{Ni}_3\text{S}_2$  and MgS in C-rich atmospheres. The presence of FeS in O-rich ejecta depends on whether some Fe is left after the condensation of pure iron, while similarly, the formation of  $\text{Ni}_3\text{S}_2$  is conditioned on the condensation of pure Ni. The observational evidence of MgS in C-rich envelopes, together with the fact that CaS is the first condensate involving either Ca or S in C-rich atmospheres, strongly indicates that CaS is a very likely constituent of dust.

**Aluminium.** Alumina ( $\text{Al}_2\text{O}_3$ ) is predicted to be the first and main Al condensate in O-rich atmospheres, which is in line with observational evidence from infrared observations (Onaka et al. 1989) and from the analysis of presolar meteoritic material (Nittler et al. 1994; Hutcheon et al. 1994). Other main condensates that appear later in the condensation sequence of Al and that can trap part of the Al that is not used by alumina are hibonite ( $\text{CaAl}_2\text{O}_7$ ), grossite ( $\text{CaAl}_4\text{O}_7$ ), gehlenite ( $\text{Ca}_2\text{Al}_2\text{SiO}_7$ ), spinel ( $\text{MgAl}_2\text{O}_4$ ), anorthite ( $\text{CaAl}_2\text{Si}_2\text{O}_8$ ), and andalusite ( $\text{Al}_2\text{SiO}_5$ ). Observational evidence for the presence of some of these condensates has been reported, concretely, hibonite (Choi et al. 1999), gehlenite (Heras & Hony 2005), and spinel (Posch et al. 1999; Nittler et al. 1997). In C-rich atmospheres, aluminum is predicted to condense at temperatures below 1000 K. Main condensates, in order of appearance, are AlN,  $\text{Al}_4\text{C}_3$ , and  $\text{Al}_2\text{O}_3$ . None of them have been observed so far.

**Calcium.** The first Ca condensates expected in O-rich atmospheres are the calcium aluminum oxides hibonite and grossite (already mentioned when discussing aluminum), and perovskite ( $\text{CaTiO}_3$ ). These condensates can only trap a fraction of the calcium, however. In particular, the low abundance of  $\text{CaTiO}_3$  may be behind the lack of observational evidence of this mineral in O-rich dust. Main Ca condensates that appear later in the condensation sequence of Ca are the calcium aluminum silicates gehlenite and anorthite. In C-rich atmospheres, calcium is expected to condense at relatively large distances from the AGB star ( $> 6.5 R_*$ , corresponding to temperatures around or below 800 K). The first main Ca condensate is CaS, followed by the same calcium aluminum oxides and silicates expected in O-rich ejecta.

The condensates involving other refractory elements that are less abundant than calcium are given in Table 5. For several elements, the first and main expected condensate is the same, regardless of the C/O. This is the case of Na and K, in which case albite ( $\text{NaAlSi}_3\text{O}_8$ ) and orthoclase ( $\text{KAlSi}_3\text{O}_8$ ) are the main expected condensates, of Ni and Cu, which are predicted to condense in pure metallic form, and of Sc, whose main condensate is  $\text{Sc}_2\text{O}_3$ . In the case of Cr and V, the oxides  $\text{Cr}_2\text{O}_3$  and  $\text{V}_2\text{O}_3$ , respectively, are the main expected condensate in O-rich atmo-

spheres, while in carbon-rich ejecta, these two elements are expected to condense in pure metallic form. Finally, for titanium, the main condensate in O-rich conditions is  $\text{CaTiO}_3$ , followed by several titanium oxides, while in C-rich atmospheres, TiC is clearly the main expected condensate, and this is supported by analysis of presolar grains (Bernatowicz et al. 1991).

## 6. Gas-phase precursors of dust

Condensates can only form in regions in which the gas temperature and pressure make the appearance of solid compounds thermodynamically favorable. That is, condensates cannot appear earlier than predicted by chemical equilibrium, although they can appear later, depending on the kinetics of the process of condensation. The first condensates are predicted to form at a given distance from the star, and this process must necessarily occur at the expense of gas-phase atoms and small molecules. For our adopted radial profiles of pressure and temperature, the first condensates are expected to appear when temperatures are below 2000 K in the C-rich case and 1500 K in the O-rich case (see Fig. 5). Although condensation in the expanding and cooling outflow from AGB stars occurs in nonequilibrium conditions (Gail & Sedlmayr 2013), chemical equilibrium can provide a useful starting point to examine the most likely gas-phase precursors of the first condensates.

Here we focus on the possible gas-phase precursors of the three condensates that are predicted to appear well before any other in C-rich outflows (carbon, TiC, and SiC) and of the first solid expected to condense in O-rich atmospheres:  $\text{Al}_2\text{O}_3$ . For each condensate, we examine the main gaseous reservoirs of the constituent elements, discuss the plausibility of the different reservoirs to act as precursors, and comment on the role that clusters of medium size may play in the formation of condensation nuclei.

### 6.1. Carbon dust in C-rich atmospheres

Carbon dust is expected to be the first condensate in C-rich atmospheres, except for very low C/O. In the region where graphite is expected to form according to chemical equilibrium ( $1.6 R_*$ ; see top left panel in Fig. 7), the main reservoir of carbon is acetylene. Other abundant C-bearing molecules are HCN, CS,  $\text{C}_3$ , and atomic carbon. Because HCN and CS contain nitrogen and sulfur, respectively, they are less likely candidates to act as precursors of dust made up purely of carbon. Thus, chemical equilibrium indicates that  $\text{C}_2\text{H}_2$ ,  $\text{C}_3$ , and C are the most likely precursors of carbon dust in C-type AGB atmospheres.

Gail et al. (1984) considered that  $\text{C}_2\text{H}_2$  is the main source of carbon atoms in the synthesis of graphite in C-rich outflows, which would imply a depletion in the gas-phase abundance of acetylene in the region where carbon dust forms. This is in contrast with the study of Fonfría et al. (2008), who modeled rovibrational lines of  $\text{C}_2\text{H}_2$  in the carbon star IRC +10216 and found that acetylene maintains a constant abundance out to  $\sim 20 R_*$ , a distance at which most carbon dust should have already formed. Atomic carbon is the main predicted reservoir of the element at the photosphere, although its abundance declines steeply with increasing radius. If, as predicted by chemical equilibrium, carbon dust forms inside  $2 R_*$ , then atomic carbon may provide the necessary carbon to form dust. In a recent experiment designed to mimic the formation of carbon dust in evolved stars, atomic carbon was used as precursor, leading to the synthesis of amorphous carbon nanoparticles (Martínez et al. 2019).

If atomic carbon is the precursor of carbon dust, then the formation of the first condensation nuclei must proceed through clusters  $\text{C}_n$  of increasing size. This is the theoretical scenario used by Gail et al. (1984) to describe the process of nucleation during the formation of graphite in C-rich atmospheres. Our calculations only include  $\text{C}_n$  clusters up to  $\text{C}_5$ . The most abundant in the region around  $1.6 R_*$  of these is  $\text{C}_3$ , while  $\text{C}_2$ ,  $\text{C}_4$ , and  $\text{C}_5$  have lower abundances. It is unclear whether carbon clusters larger than  $\text{C}_5$  might be stable enough to be present with a significant abundance. In any case, the large abundance of  $\text{C}_3$  makes it a good candidate to act as precursor in the formation of carbon dust. Observational constraints of the radial variation of the  $\text{C}_3$  abundance in the innermost regions of C-rich envelopes, currently restricted to the outer envelope (Hinkle et al. 1988), might shed light on this.

### 6.2. Titanium carbide dust in C-rich atmospheres

Titanium carbide is predicted to be the first condensate in the atmospheres of C-stars with very low C/O and in S-type atmospheres. The finding of TiC grains embedded in presolar graphitic material also indicates that TiC is a first condensate (Bernatowicz et al. 1991). Given the relative elemental abundances of titanium and carbon and the stoichiometry 1:1 of solid TiC, the formation of titanium carbide dust will be limited by the precursor providing Ti. Titanium carbide is expected to condense at a radius of  $2.3 R_*$  in our fiducial C-rich atmosphere. In this region, the main reservoir of titanium is atomic Ti (see the top right panel in Fig. 7). Gail & Sedlmayr (2013) suggested that atomic Ti reacting with  $\text{C}_2\text{H}_2$  is the net reaction responsible for the formation of TiC dust. Acetylene is indeed the main reservoir of carbon at  $2.3 R_*$ , although atomic carbon also has an abundance comparable to that of atomic Ti and might act as the carbon-supplier precursor.

Several gaseous molecules contain both titanium and carbon and might play a role in the formation of TiC dust. The most obvious is the diatomic molecule TiC, which is predicted to have a too low abundance, however. Therefore, a process of formation of TiC grains through a sequence of addition of TiC molecules to form clusters  $(\text{TiC})_n$  of increasing size  $n$  is unlikely because of the low amount of Ti locked by TiC molecules. Of the small Ti-C molecules,  $\text{TiC}_2$  is the most abundant, although it remains orders of magnitude below atomic Ti. Large  $\text{Ti}_x\text{C}_y$  clusters become abundant at the expense of atomic Ti and small Ti-bearing molecules in the region where TiC dust condensation is expected. Although this coincidence may be accidental, it strongly suggests that the assembly of large  $\text{Ti}_x\text{C}_y$  clusters might be related to the formation of TiC condensation nuclei. The most stable and abundant  $\text{Ti}_x\text{C}_y$  clusters are  $\text{Ti}_8\text{C}_{12}$  and  $\text{Ti}_{13}\text{C}_{22}$ , the former displacing atomic Ti as main reservoir of titanium at radii larger than  $2.3 R_*$ . Therefore,  $\text{Ti}_8\text{C}_{12}$  emerges as a very attractive candidate of a gas-phase precursor of TiC dust. It is clear that formation through addition of  $\text{Ti}_8\text{C}_{12}$  monomers leading to  $(\text{Ti}_8\text{C}_{12})_n$  of increasing  $n$  does not preserve the stoichiometry of solid TiC. If  $\text{Ti}_8\text{C}_{12}$  acts as precursor, some rearrangement in which Ti atoms are incorporated or carbon atoms are lost is needed during the growth of TiC condensation nuclei.

The condensation of TiC in the outflows of carbon stars has been studied theoretically in conditions of nonequilibrium by Chigai et al. (1999). These authors considered the growth of  $(\text{TiC})_n$  clusters of increasing size through chemical reactions involving atomic Ti and  $\text{C}_2\text{H}_2$ , following the formalism described by Gail & Sedlmayr (1988) for the heteromolecular formation and growth of carbon grains. Chigai et al. (1999) found that

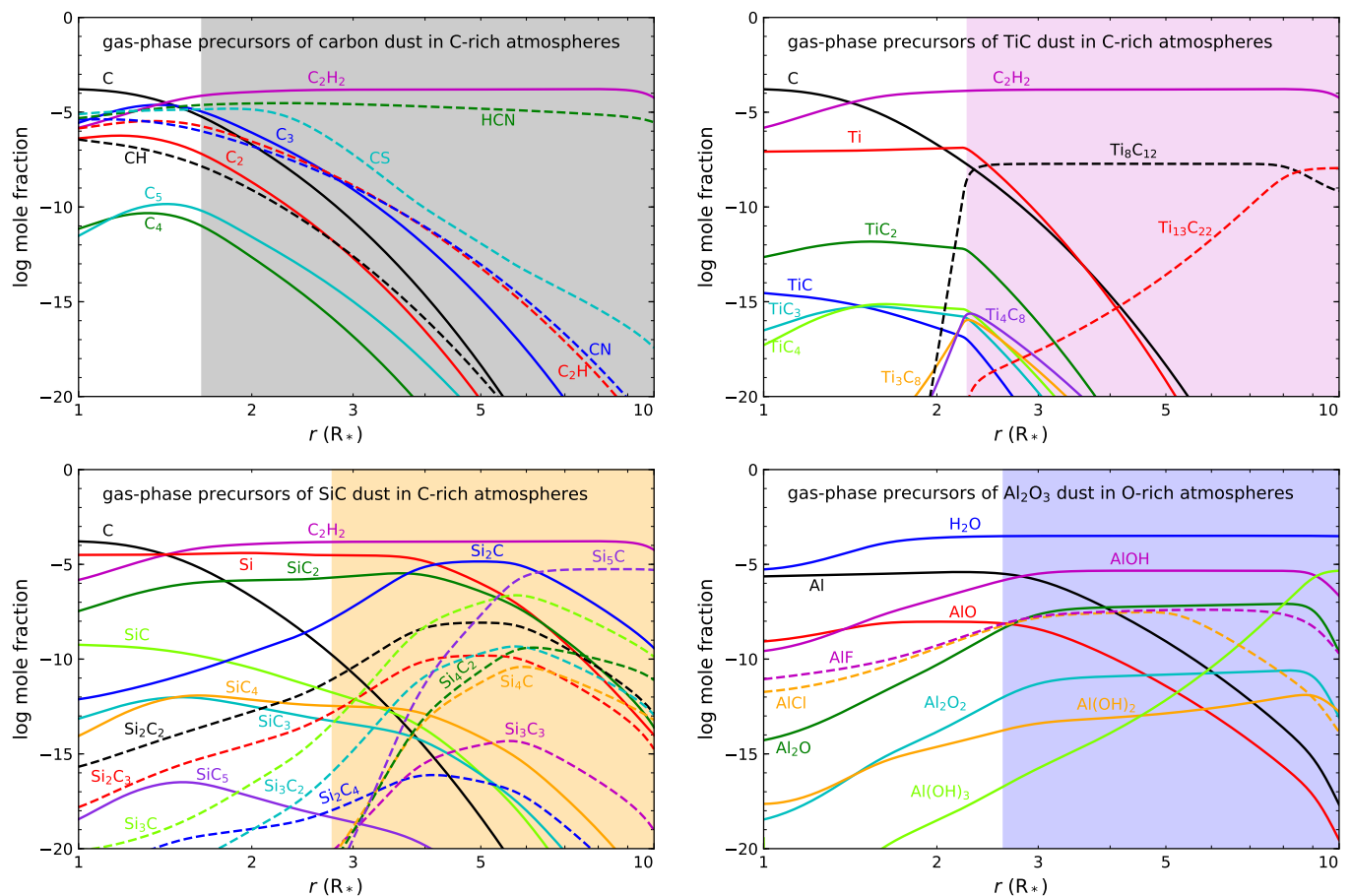


**Fig. 7.** Calculated chemical equilibrium abundances as a function of radius for gaseous reservoirs that can act as precursors of some of the first condensates expected in C- and O-rich AGB atmospheres: carbon, TiC, and SiC dust in C-rich stars (top left, top right, and bottom left, respectively), and  $\text{Al}_2\text{O}_3$  dust in O-rich stars (bottom right). Abundances correspond to chemical equilibrium calculations in which only gaseous species are included. The shadowed areas indicate the regions where the condensation of the different types of dust is thermodynamically favorable: from 1.6  $R_{\odot}$  for graphite, 2.3  $R_{\odot}$  for TiC, 2.8  $R_{\odot}$  for SiC, and 2.6  $R_{\odot}$  for  $\text{Al}_2\text{O}_3$ .

formation of TiC cores covered by graphite mantles, in agreement with the constraints from presolar grains (Bernatowicz et al. 1991), is possible over certain ranges of mass-loss rate and gas outflow velocity. The study of Chigai et al. (1999), however, did not investigate the detailed chemical pathways leading to the formation of TiC molecules and small  $(\text{TiC})_n$  clusters, mainly because the relevant reactions and rate constants are unknown.

### 6.3. Silicon carbide dust in C-rich atmospheres

Silicon carbide is expected to condense after carbon and TiC for C/O higher than 1.02 and after TiC for any C/O (see Fig. 5). This implies that SiC grains may nucleate heterogeneously, that is, on preexisting condensation nuclei of carbon and/or TiC. However, the analysis of a presolar SiC grain containing TiC crystals seems to indicate that SiC and TiC nucleated and grew independently (Bernatowicz et al. 1992), which implies that SiC can nucleate homogeneously. Silicon carbide is expected to condense at 2.8  $R_{\odot}$ , and in this region, the main reservoir of silicon is atomic Si, while the main reservoir of carbon is  $\text{C}_2\text{H}_2$  (see the bottom left panel in Fig. 7). Therefore, these two species are candidates for gas-phase precursors of SiC dust, as suggested by Gail & Sedlmayr (2013). The role of acetylene in the formation of dust is in question, however, because of the lack of radial abundance

decline inferred for IRC +10216 (Fonfría et al. 2008), as discussed in Sec. 6.1.

Alternative candidates are molecules containing Si-C bonds, some of which are predicted to be abundant in C-rich atmospheres. Concretely,  $\text{SiC}_2$ , in the condensation region of SiC dust,  $\text{Si}_2\text{C}$ , slightly farther away, and  $\text{Si}_5\text{C}$ , at even larger radii, are predicted to be the most abundant carriers of Si-C bonds (see the bottom left panel in Fig. 7). The molecules  $\text{SiC}_2$  and  $\text{Si}_2\text{C}$  are indeed observed to be abundant in C-rich atmospheres (Cernicharo et al. 2010; Fonfría et al. 2014; Cernicharo et al. 2015; Massalkhi et al. 2018). Moreover, there is evidence that  $\text{SiC}_2$  is a gas-phase precursor of SiC dust. On the one hand, Fonfría et al. (2014) inferred an abundance decline with increasing radius in the dust formation region of IRC +10216. On the other, Massalkhi et al. (2018) found that the abundance of  $\text{SiC}_2$  in C-rich AGB envelopes decreases with increasing envelope density. Both observational facts indicate a depletion of gaseous  $\text{SiC}_2$  to form SiC dust grains. The molecule  $\text{Si}_2\text{C}$  is as abundant as  $\text{SiC}_2$  (Cernicharo et al. 2015) and might also act as gas-phase precursor of SiC dust.

The formation of SiC dust in the outflows of C-rich AGB stars has been studied theoretically by Yasuda & Kozasa (2012). These authors presented chemical equilibrium abundances for  $\text{Si}_x\text{C}_y$  species that agree with ours. This is expected because we used the same thermochemical properties for  $\text{Si}_x\text{C}_y$  species

as they did, that is, those of Deng et al. (2008). Yasuda & Kozasa (2012) investigated further the kinetics of formation of SiC dust in the framework of a dust-driven wind model considering a nucleation process consisting of addition of SiC and Si<sub>2</sub>C<sub>2</sub> molecules to form (SiC)<sub>n</sub> clusters of increasing *n*. This clustering sequence is also favored by the quantum chemical calculations of (SiC)<sub>n</sub> clusters by Gobrecht et al. (2017). While small condensation nuclei may form at the expense of SiC and Si<sub>2</sub>C<sub>2</sub>, the abundances of these molecules is too low to provide the required amount of SiC dust. Observations derive dust-to-gas mass ratios of  $(1 - 4) \times 10^{-3}$  (Ramstedt et al. 2008) and mass ratios between SiC and carbon dust of 0.02-0.25 (Groenewegen et al. 1998), which results in a mass ratio between SiC dust and H<sub>2</sub> of  $(0.2 - 10) \times 10^{-4}$ . The calculated mole fraction of Si<sub>2</sub>C<sub>2</sub> is at most  $10^{-8}$ , which translates into a mass ratio relative to H<sub>2</sub> of  $2 \times 10^{-7}$ , at least two orders of magnitude below the observational value. The probability of the SiC molecule to act as main gas-phase precursor of SiC dust is even lower because the predicted abundance is low, which agrees with the abundance upper limit derived from observations (Velilla Prieto et al. 2015). In summary, nucleation may occur by addition of SiC and Si<sub>2</sub>C<sub>2</sub> molecules to (SiC)<sub>n</sub> clusters, although the mass of condensation nuclei grown by this process is limited by the low gas-phase abundance of SiC and Si<sub>2</sub>C<sub>2</sub>. The molecules SiC<sub>2</sub> and Si<sub>2</sub>C thus emerge as the two most likely gas-phase precursors of SiC dust.

#### 6.4. Alumina dust in O-rich atmospheres

Alumina is the first main condensate predicted to appear in O-rich atmospheres. Our chemical equilibrium calculations places its condensation radius at  $2.6 R_*$ . In this region, the main carriers of aluminum are atomic Al and AlOH (see the bottom right panel in Fig. 7). Other carriers of Al in the condensation region of alumina are AlO, Al<sub>2</sub>O, AlF, and AlCl. From these, atomic Al and the molecules containing an Al-O bond arise as the most likely gas-phase precursors of Al<sub>2</sub>O<sub>3</sub>.

Gail & Sedlmayr (2013) suggested that atomic Al reacting with water, the main carrier of oxygen other than CO, drive the condensation of Al<sub>2</sub>O<sub>3</sub>. Gobrecht et al. (2016) modeled the kinetics of formation of alumina dust in M-type atmospheres. In their chemical scheme, clusters (Al<sub>2</sub>O<sub>3</sub>)<sub>2</sub>, the seed of condensation nuclei, form by three-body recombination of Al<sub>2</sub>O<sub>3</sub> molecules. The formation of Al<sub>2</sub>O<sub>3</sub> molecules relies on the oxidation, by reaction with H<sub>2</sub>O, of Al<sub>2</sub>O<sub>2</sub>, which is formed by three-body recombination of AlO, which in turn is formed in the reaction of atomic Al with OH. In the scenario depicted by these authors, the starting reservoir of aluminum therefore is atomic Al, with AlO, Al<sub>2</sub>O<sub>2</sub>, and Al<sub>2</sub>O<sub>3</sub> acting as intermediate species. In the more recent model by Boulanger et al. (2019), in which the chemical kinetics scheme was revised with respect to Gobrecht et al. (2016), Al<sub>2</sub>O<sub>3</sub> molecules are not efficiently formed, which prevents the growth of large (Al<sub>2</sub>O<sub>3</sub>)<sub>n</sub> clusters. Boulanger et al. (2019) indicated that limitations in the chemical network for Al-bearing species are the reason for the low abundance of Al<sub>2</sub>O<sub>3</sub>.

From an observational point of view, two potential gas-phase precursors of alumina dust have been observed around M-type stars: AlO and AlOH (Kamiński et al. 2016; Decin et al. 2017). Reliable radial abundance distributions have not been derived, however, which makes it difficult to evaluate whether these molecules act as gas-phase precursors of alumina dust.

## 7. Summary

We investigated theoretically the chemical composition of AGB atmospheres of M-, S-, and C-type by means of chemical equilibrium calculations using a recently developed code. We compiled a large dataset of thermochemical properties for 919 gaseous and 185 condensed species involving 34 elements. We considered for the first time a large number of titanium-carbon clusters. Concretely, we computed thermochemical data for all Ti<sub>x</sub>C<sub>y</sub> clusters with  $x = 1-4$  and  $y = 1-4$  and for various stable large clusters such as Ti<sub>3</sub>C<sub>8</sub>, Ti<sub>4</sub>C<sub>8</sub>, Ti<sub>6</sub>C<sub>13</sub>, Ti<sub>7</sub>C<sub>13</sub>, Ti<sub>8</sub>C<sub>12</sub>, Ti<sub>9</sub>C<sub>15</sub>, and Ti<sub>13</sub>C<sub>22</sub>. We studied the chemical composition in the 1-10  $R_*$  region of a generic AGB atmosphere by adopting realistic radial profiles of temperature and pressure based on constraints from recent observations and results from hydrodynamic models.

We compared the predictions of chemical equilibrium with the latest observational constraints. Chemical equilibrium reproduces the observed abundances of most of the parent molecules detected in AGB envelopes reasonably well. However, there are serious discrepancies between chemical equilibrium and observations for some parent molecules, which are observed with abundances several orders of magnitude above the expectations from chemical equilibrium. The concerned species are HCN, CS, NH<sub>3</sub>, and SO<sub>2</sub> in M-type stars, H<sub>2</sub>O and NH<sub>3</sub> in S-type stars, and the hydrides H<sub>2</sub>O, NH<sub>3</sub>, SiH<sub>4</sub>, and PH<sub>3</sub> in C-type stars.

We systematically surveyed of each element, examining the main reservoirs (see Appendix A) and identifying several molecules that have not yet been observed in AGB atmospheres, but are predicted with non-negligible abundances. The most promising detectable molecules are SiC<sub>5</sub>, SiNH, SiCl, PS, HBO, and the metal-containing molecules MgS, CaS, CaOH, CaCl, CaF, ScO, ZrO, VO, FeS, CoH, and NiS. For most of them, sensitive high-angular resolution observations with telescopes such as ALMA offer the best probabilities of detection.

We also investigated which condensates are predicted to appear and at which radius they are expected according to chemical equilibrium. In agreement with previous studies, we found that carbon, TiC, and SiC are the first condensates predicted to appear in C-rich outflows, while in O-rich atmospheres, Al<sub>2</sub>O<sub>3</sub> is the first main expected condensate. Chemical equilibrium indicates that the most probable gas-phase precursors of carbonaceous dust are acetylene, atomic carbon, and/or C<sub>3</sub>, while silicon carbide dust is most probably formed at the expense of the molecules SiC<sub>2</sub> and Si<sub>2</sub>C. As concerns TiC dust, most titanium is atomic in the inner regions of AGB atmospheres and thus atomic Ti is a likely supplier of titanium during the formation of TiC dust. Interestingly, we found that according to chemical equilibrium, large titanium-carbon clusters such as Ti<sub>8</sub>C<sub>12</sub> and Ti<sub>13</sub>C<sub>22</sub> become the main reservoirs of titanium at the expense of atomic Ti in the region where TiC condensation is expected to occur. This strongly indicates that large Ti<sub>x</sub>C<sub>y</sub> clusters are important intermediate species during the formation of the first condensation nuclei of TiC. Finally, in the case of Al<sub>2</sub>O<sub>3</sub> dust, chemical equilibrium indicates that the main gas-phase precursor must be atomic Al or the molecules AlOH, AlO, and Al<sub>2</sub>O, which are the main carriers of Al-O bonds in O-rich atmospheres.

*Acknowledgements.* We acknowledge funding support from the European Research Council (ERC Grant 610256: NANOCOSMOS) and from Spanish MINECO through grants AYA2016-75066-C2-1-P and MAT2017-85089-C2-1-R. M.A. and J.I.M. also acknowledge funding support from the Ramón y Cajal programme of Spanish MINECO (grants RyC-2014-16277 and RyC-2015-17730, respectively). We thank the anonymous referee for a detailed report which helped to improve this manuscript. M.A. thanks Carlos Abia for an interesting discussion on elemental abundances and C/O, and Sara Bladh and Bernd Frey-

tag for kindly providing radial profiles from their hydrodynamic models of AGB atmospheres. P.L.A. thanks Allan East for useful discussions.

## References

- Abia, C., Boffin, H. M. J., Isern, J., & Rebolo, R. 1993, *A&A*, 272, 455
- Abia, C. & Wallerstein, G. 1998, *MNRAS*, 293, 89
- Abia, C., Domínguez, I., Gallino, R., et al. 2002, *ApJ*, 579, 817
- Abia, C., Cunha, K., Cristallo, S., et al. 2010, *ApJ*, 715, L94
- Abia, C., Cunha, K., Cristallo, S., & de Laverny, P. 2015, *A&A*, 581, A88
- Abia, C., Cristallo, S., Cunha, K., et al. 2019, *A&A*, 625, A40
- Adam, C. & Ohnaka, K. 2019, *A&A*, 628, A132
- Agúndez, M. & Cernicharo, J. 2006, *ApJ*, 650, 374
- Agúndez, M., Cernicharo, J., & Guélin, M. 2007, *ApJ*, 662, L91
- Agúndez, M., Cernicharo, J., Pardo, J. R., et al. 2008, *A&A*, 485, L33
- Agúndez, M., Cernicharo, J., & Guélin, M. 2010, *ApJ*, 724, L133
- Agúndez, M., Cernicharo, J., Waters, L. B. F. M., et al. 2011, *A&A*, 553, L6
- Agúndez, M., Fonfría, J. P., Cernicharo, J., et al. 2012, *A&A*, 543, A48
- Agúndez, M., Parmentier, V., Venot, O., et al. 2014b, *A&A*, 564, A73
- Agúndez, M., Cernicharo, J., Decin, L., et al. 2014b, *ApJ*, 790, L27
- Agúndez, M., Cernicharo, J., & Guélin, M. 2014c, *A&A*, 570, A45
- Allen, M. D., Ziurys, L. M., & Brown, J. M. 1996, *Chem. Phys. Lett.*, 257, 130
- Allibert, M., Chatillon, C., Jacob, K. T., & Lourttau, R. 1981, *J. Am. Ceram. Soc.*, 64, 307
- Álvarez-Barcia, S. & Flores, J. R. 2016, *PCCP*, 18, 6103
- Amari, S., Anders, E., Virag, A., & Zinner, E. 1990, *Nature*, 345, 238
- Anderson, M. A., Allen, M. D., & Ziurys, L. M. 1994, *ApJ*, 424, 503
- Asplund, M., Grevesse, N., Sauval, A. J., & Scott, P. 2009, *ARA&A*, 47, 481
- Balducci, G., Gigli, G., & Guido, M. 1983, *J. Chem. Phys.*, 79, 5616
- Barklem, P. S., & Collet, R. 2016, *A&A*, 588, A96
- Bauschlicher, C. W. & Maitre, P. 1995, *Theor. Chim. Acta*, 90, 189
- Beaton, S. A. & Gerry, C. L. 1999, *J. Chem. Phys.*, 110, 10715
- Becke, A. D. 1988, *Phys. Rev. A*, 38, 3098
- Bergeat, J., Knapik, A., & Rutily, B. 2001, *A&A*, 369, 178
- Bernatowicz, T. J., Fraundorf, G., Ming, T., et al. 1987, *Nature*, 330, 728
- Bernatowicz, T. J., Amari, S., Zinner, E. K., & Lewis, R. S. 1991, *ApJ*, 373, L73
- Bernatowicz, T. J., Amari, S., & Lewis, R. S. 1992, *Lunar Planet. Sci.*, 23, 91
- Bernatowicz, T. J., Cowsik, R., Gibbons, P. C., et al. 1996, *ApJ*, 472, 760
- Betrencourt, M., Boudjaadar, D., Chollet, P., et al. 1986, *J. Chem. Phys.*, 84, 4121
- Betz, A. L., McLaren, R. A., & Spears, D. L. 1979, *ApJ*, 229, L97
- Bladh, S., Liljegren, S., Höfner, S., et al. 2019, *A&A*, 626, A100
- Blecic, J., Harrington, J., & Bowman, M. O. 2016, *ApJS*, 225, 4
- Blom, C. E., Hedderich, H. G., Lovas, F. J., et al. 1992, *J. Mol. Spectr.*, 152, 109
- Blommaert, J. A. D. L., de Vries, B. L., Waters, L. B. F. M., et al. 2014, *A&A*, 565, A109
- Bogey, M., Demuynck, C., Destombes, J. L., & Walters, A. 1991, *A&A*, 244, L47
- Boulangier, J., Gobrecht, D., Decin, L., et al. 2019, *MNRAS*, 489, 4890
- Breier, A. A., Waßmuth, B., Büchling, T., et al. 2018, *J. Mol. Spectr.*, 350, 43
- Brinkley Jr., S. R. 1947, *J. Chem. Phys.*, 15, 107
- Brugh, D. J., Suenram, R. D., & Stevens, W. J. 1999, *J. Chem. Phys.*, 111, 3526
- Brünken, S., Müller, H. S. P., Lewen, F., & Giesen, T. F. 2005, *J. Chem. Phys.*, 123, 164315
- Bujarrabal, V., Fuente, A., & Omont, A. 1994, *A&A*, 285, 247
- Büsener, H., Heinrich, F., & Hese, A. 1987, *Chem. Phys.*, 112, 139
- Cabezas, C., Cernicharo, J., Alonso, J. L., et al. 2013, *ApJ*, 775, 133
- Cannon, N. A., Boldyrev, A. I., Li, X., & Wang, L.-S. 2000, *J. Chem. Phys.*, 113, 2671
- Cernicharo, J. & Guélin, M. 1987, *A&A*, 183, L10
- Cernicharo, J., Waters, L. B. F. M., Decin, L., et al. 2010, *A&A*, 521, L8
- Cernicharo, J., McCarthy, M. C., Gottlieb, C. A., et al. 2015, *ApJ*, 806, L3
- Cernicharo, J., Velilla-Prieto, L., Agúndez, M., et al. 2019a, *A&A*, 627, L4
- Cernicharo, J., Cabezas, C., Pardo, J. R., et al. 2019b, *A&A*, 630, L2
- Chase Jr., M. W. 1998, *NIST-JANAF Thermochemical Tables 4th ed.*, *J. Phys. Chem. Ref. Data Monogr.* 9
- Cherchneff, I. & Barker, J. R. 1992, *ApJ*, 394, 703
- Cherchneff, I. 2006, *A&A*, 456, 1001
- Cherchneff, I. 2011, *A&A*, 526, L11
- Cherchneff, I. 2012, *A&A*, 545, A12
- Chigai, T., Yamamoto, T., & Kozasa, T. 1999, *ApJ*, 510, 999
- Childs, W. J., Goodman, L. S., Nielsen, U., & Pfeufer, V. 1984, *J. Chem. Phys.*, 80, 2283
- Choi, B.-G., Wasseburg, G. J., & Huss, G. R. 1999, *ApJ*, 522, L133
- Clegg, R. E. S. & Lambert, D. L. 1978, *ApJ*, 226, 931
- Danilovich, T., Bergman, P., Justtanont, K., et al. 2014, *A&A*, 569, A76
- Danilovich, T., De Beck, E., Black, J. H., et al. 2016, *A&A*, 588, A119
- Danilovich, T., Van de Sande, M., De Beck, E., et al. 2017, *A&A*, 606, A124
- Danilovich, T., Ramstedt, S., Gobrecht, D., et al. 2018, *A&A*, 617, A132
- Danilovich, T., Richards, A. M. S., Karakas, A. I., et al. 2019, *MNRAS*, 484, 494
- De Beck, E., Lombaert, R., Agúndez, M., et al. 2012, *A&A*, 539, A108
- De Beck, E., Kamiński, T., Patel, N. A., et al. 2013, *A&A*, 558, A132
- Decin, L., Agúndez, M., Barlow, M. J., et al. 2010, *Nature*, 467, 64
- Decin, L., Richards, A. M. S., Waters, L. B. F. M., et al. 2017, *A&A*, 608, A55
- Decin, L., Richards, A. M. S., Danilovich, T., et al. 2018a, *A&A*, 615, A28
- Decin, L., Danilovich, T., Gobrecht, D., et al. 2018b, *ApJ*, 855, 113
- Deng, J. L., Su, K. H., Wang, X., et al. 2008, *Eur. Phys. J. D*, 49, 21
- DePew, K., Speck, A., & Dijkstra, C. 2006, *ApJ*, 640, 971
- Dewar, M. J. S., Jie, C., & Zöebisch, E. G. 1988, *Organometallics*, 7, 513
- DeYonker, N. J., Li, S., Yamaguchi, Y., et al. 2005, *J. Chem. Phys.*, 122, 234316
- Dong, F., Heinbuch, S., Xie, Y., et al. 2010, *PCCP*, 12, 2569
- Drouin, B. J., Yu, S., Miller, C. E., et al. 2010, *J. Quant. Spectr. Rad. Transf.*, 111, 1167
- Duari, D., Cherchneff, I., & Willacy, K. 1999, *A&A*, 341, L47
- Dubois, I. 1977, *A&A*, 57, 51
- Duning, T. H. 1989, *J. Chem. Phys.*, 90, 1007
- Eriksson, G. 1971, *Acta Chem. Scand.*, 25, 2651
- Ernst, W. E. & Törring, T. 1983, *Phys. Rev. A*, 27, 875
- Ernst, W. E., Kindt, S., Nair, K. P. R., & Törring, T. 1984, *Phys. Rev. A*, 29, 1158
- Flores-Mijangos, J., Brown, J. M., Matsushima, F., et al. 2004, *J. Mol. Spectr.*, 225, 189
- Flory, M. A. & Ziurys, L. M. 2008, *J. Mol. Spectr.*, 247, 76
- Fonfría, J. P., Cernicharo, J., Richter, M. J., & Lacy, J. H. 2008, *ApJ*, 673, 445
- Fonfría, J. P., Fernández-López, M., Agúndez, M., et al. 2014, *MNRAS*, 445, 3289
- Fonfría, J. P., Hinkle, K. H., Cernicharo, J., et al. 2017, *ApJ*, 835, 196
- Fonfría, J. P., Santander-García, M., Cernicharo, J., et al. 2019, *A&A*, 622, L14
- Ford, K. E. S. & Neufeld, D. A. 2001, *ApJ*, 557, L113
- Fowler, P. W. & Sadlej, A. J. 1991, *Mol. Phys.*, 73, 43
- Freytag, B., Liljegren, S., & Höfner, S. 2017, *A&A*, 600, A137
- Frisch, M. J., Trucks, G. W., Schlegel, H. B., et al. 2009, *Gaussian-09 Rev. E.01*; model: B3LYP/cc-pVTZ (C and Ti) and SDD (Ti)
- Gail, H.-P., Keller, R., & Sedlmayr, E. 1984, *A&A*, 133, 320
- Gail, H.-P. & Sedlmayr, E. 1988, *A&A*, 206, 153
- Gail, H.-P. & Sedlmayr, E. 2013, *Physics and Chemistry of Circumstellar Dust Shells* (Cambridge: Cambridge Univ. Press)
- Gehrz, R. D. 1989, in *Interstellar Dust*, ed. L. J. Allamandola & A. G. G. M. Tielens, *IAU Symp.* 135, 445
- Geiger, C. A., Kleppa, O. J., Mysen, B. O., et al. 1988, *Geochim. Cosmochim. Acta*, 52, 1729
- Giannozzi, P., Baroni, S., Bonini, N., et al. 2009, *J. Phys. Condens. Matter*, 21, 395502
- Gobrecht, D., Cherchneff, I., Sarangi, A., et al. 2016, *A&A*, 585, A6
- Gobrecht, D., Cristallo, S., Piersanti, L., & Bromley, S. T. 2017, *ApJ*, 840, 117
- Goebel, J. H. & Moseley, S. H. 1985, *ApJ*, 290, L35
- González-Alfonso, E. & Cernicharo, J. 1999, *ApJ*, 525, 845
- González Delgado, D., Olofsson, H., Kerschbaum, F., et al. 2003, *A&A*, 411, 123
- Goos, E., Burcat, A., & Ruscic, B., *Extended Third Millennium Ideal Gas Thermochemical Database with updates from Active Thermochemical Tables*, <https://burcat.technion.ac.il/>
- Gordon, S. & McBride, B. J. 1994, *NASA Reference Publication 1311*, I
- Gosavi, R. K. & Strausz, O. P. 1986, *Chem. Phys. Lett.*, 131, 243
- Goto, M. & Saito, S. 1993, *Chem. Phys. Lett.*, 211, 443
- Goumans, T. P. M. & Bromley, S. T. 2012, *MNRAS*, 420, 3344
- Goumans, T. P. M. & Bromley, S. T. 2013, *Philos. Trans. Royal Soc. A*, 371, 20110580
- Groenewegen, M. A. T., Whitelock, P. A., Smith, C. H., & Kerschbaum, F. 1998, *MNRAS*, 293, 18
- Guélin, M., Lucas, R., & Cernicharo, J. 1993, *A&A*, 280, L19
- Guichemerre, M. & Chabaud, G. 2000, *J. Phys. Chem. A*, 104, 2105
- Gurvich, L. V., Veyts, I. V., & Alcock, C. B. 1989, *Thermodynamic Properties of Individual Substances* (New York: Hemisphere)
- Gutsev, G. L., Rao, B. K., & Jena, P. 2000, *J. Phys. Chem. A*, 104, 11961
- Halfen, D. T. & Ziurys, L. M. 2004, *ApJ*, 607, L63
- Halfen, D. T. & Ziurys, L. M. 2008, *ApJ*, 672, L77
- Halfen, D. T. & Ziurys, L. M. 2016, *ApJ*, 833, 89
- Halfen, D. T., Min, J., & Ziurys, L. M. 2017, *J. Mol. Spectr.*, 331, 1
- Harrison, J. F. & Hutchison, J. H. 1999, *Mol. Phys.*, 97, 1009
- Hasegawa, T. I., Kwok, S., Koning, N., et al. 2006, *ApJ*, 637, 791
- Helms, D. A., Winniewisser, M., & Winniewisser, G. 1980, *J. Phys. Chem.*, 84, 1758
- Heras, A. M. & Hony, S. 2005, *A&A*, 439, 171
- Hinkle, K. W., Keady, J. J., & Bernath, P. F. 1988, *Science*, 241, 1319
- Hinkle, K. W., Lambert, D. L., & Wing, R. F. 1989, *MNRAS*, 238, 1365
- Hocking, W. H., Pearson, E. F., Creswell, R. A., & Winniewisser, G. 1978, *J. Chem. Phys.*, 68, 1128
- Höfner, S. & Olofsson, H. 2018, *A&A Rev.*, 26, 1

- Hohenberg, P. & Kohn, W. 1964, *Phys. Rev.*, 136, B864
- Hony, S., Heras, A. M., Molster, F. J., & Smolders, K. 2009, *A&A*, 501, 609
- Hutcheon, I. D., Huss, G. R., Fahey, A. J., & Wasseburg, G. J. 1994, *ApJ*, 425, L97
- Janczyk, A. & Ziurys, L. M. 2006, *J. Mol. Spectr.*, 236, 11
- Jonsson, J., Launila, O., & Lindgren, B. 1992, *MNRAS*, 258, 49
- Joyce, R. R., Hinkle, K. H., Wallace, L., et al. 1998, *AJ*, 116, 2520
- Kamiński, T., Gottlieb, C. A., Menten, K. M., et al. 2013, *A&A*, 551, A113
- Kamiński, T., Mason, E., Tylenda, R., & Schmidt, M. R. 2015, *A&A*, 580, A34
- Kamiński, T., Wong, K. T., Schmidt, M. R., et al. 2016, *A&A*, 592, A42
- Kamiński, T., Müller, H. S. P., Schmidt, M. R., et al. 2017, *A&A*, 599, A59
- Kardar, M. *Statistical Physics of Particles*, (Cambridge Univ. Press), Cambridge (UK), 2007
- Karna, S. P. & Grein, F. 1987, *J. Mol. Spectr.*, 122, 28
- Katoh, K., Okabayashi, T., Tanimoto, M., et al. 2004, *J. Chem. Phys.*, 120, 7927
- Kawaguchi, K., Kagi, E., Hirano, T., et al. 1993, *ApJ*, 406, L39
- Kawashima, Y., Endo, Y., Kawaguchi, K., & Hirota, E. 1987, *Chem. Phys. Lett.*, 135, 441
- Keady, J. J. & Ridgway, S. T. 1993, *ApJ*, 406, 199
- Kee, R. J., Rupley, F. M., Miller, J. A., et al. 2000, *CHEMKIN Collection*, Release 3.6, Reaction Design, Inc., San Diego, CA
- Keenan, P. C. & Schroeder, L. W. 1952, *ApJ*, 115, 82
- Keenan, P. C. 1954, *ApJ*, 120, 484
- Kemper, F., de Koter, A., Waters, L. B. F. M., et al. 2002, *A&A*, 384, 585
- Khouri, T., Maercker, M., Waters, L. B. F. M., et al. 2016, *A&A*, 591, A70
- Khouri, T., Vlemmings, W. H. T., Olofsson, H., et al. 2018, *A&A*, 620, A75
- Klaus, T., Takano, S., & Winnewisser, G. 1997, *A&A*, 322, L1
- Klisch, E., Klein, H., Winnewisser, G., & Herbst, E. 1998, *Z. Naturforsch. A*, 53, 733
- Köhler, T. M., Gail, H.-P., & Sedlmayr, E. 1997, *A&A*, 320, 553
- Kohn, W. & Sham, L. J. 1965, *Phys. Rev.*, 140, A1133
- Koseki, S., Matsushita, T., & Gordon, M. S. 2006, *J. Phys. Chem. A*, 110, 2560
- Kröckertskoth, T., Knöckel, H., & Tiemann, E. 1987, *Mol. Phys.*, 62, 1031
- Lambert, D. L., Gustafsson, B., Eriksson, K., & Hinkle, K. H. 1986, *ApJS*, 62, 373
- Lammertsma, K. & Güner, O. F. 1988, *J. Am. Chem. Soc.*, 110, 5239
- Le Bertre, T. 1988, *A&A*, 190, 79
- Lewen, F., Brünken, S., Winnewisser, G., et al. 2004, *J. Mol. Spectr.*, 226, 113
- Lodders, K. & Fegley Jr., B. 1993, *Earth Planet. Sci. Lett.*, 117, 125
- Lodders, K. & Fegley Jr., B. 1997, in *Astrophysical Implications of the Laboratory Study of Presolar Materials*, ed. T. J. Bernatowitz & E. Zinner (Woodbury, NY: AIP), 391
- Lodders, K. & Fegley Jr., B. 1999, in *Asymptotic Giant Branch Stars*, ed. T. Le Bertre, A. Lèbre, & C. Waelkens, IAU Symp. 191, 279
- Lodders, K. 1999, *J. Phys. Chem. Ref. Data*, 28, 1705
- Lodders, K. 2004, *J. Phys. Chem. Ref. Data*, 33, 357
- Lodders, K. & Amari, S. 2005, *Chem. Erde-Geochem.*, 65, 93
- Lombaert, R., de Vries, B. L., de Koter, A., et al. 2012, *A&A*, 544, L18
- Maercker, M., Danilovich, T., Olofsson, H., et al. 2016, *A&A*, 591, A44
- Marigo, P., Ripamonti, E., Nanni, A., et al. 2016, *MNRAS*, 456, 23
- Martin, P. G. & Rogers, C. 1987, *ApJ*, 322, 374
- Martin-Drumel, M. A., Pirali, O., Balcon, D., et al. 2011, *Rev. Sci. Instrum.*, 82, 113106
- Martínez, L., Santoro, G., Merino, P., et al. 2019, *Nature Astron.*, doi:10.1038/s41550-019-0899-4
- Massalkhi, S., Agúndez, M., Cernicharo, J., et al. 2018, *A&A*, 611, A29
- Massalkhi, S., Agúndez, M., & Cernicharo, J. 2019, *A&A*, 628, A62
- Massalkhi, S., Agúndez, M., Cernicharo, J., & Velilla Prieto, L. 2020, *A&A*, submitted
- Matos, J. M., Roos, B. O., Sadlej, A. J., & Diercksen, G. H. F. 1988, *Chem. Phys.*, 119, 71
- McBride, B. J., Zehe, M. J., & Gordon, S. 2002, NASA Technical Publication TP-2002-211556
- McCarthy, M. C., Tamassia, F., & Thorwirth, S. 2015, *Mol. Phys.*, 113, 2204
- McCarthy, M. C., Gottlieb, C. A., & Cernicharo, J. 2019, *J. Mol. Spectr.*, 356, 7
- Melendres, C. A., Hebert, A. J., & Street, K. 1969, *J. Chem. Phys.*, 51, 855
- Melnick, G. J., Neufeld, D. A., Ford, K. E. S., et al. 2001, *Nature*, 412, 160
- Milam, S. N., Apponi, A. J., Woolf, N. J., & Ziurys, L. M. 2007, *ApJ*, 668, L131
- Milam, S. N., Halfen, D. T., Tenenbaum, E. D., et al. 2008, *ApJ*, 684, 618
- Möller, K., Schütze-Pahlmann, H.-K., Hoefl, J., & Törring, T. 1982, *Chem. Phys.*, 68, 399
- Molster, F. J., Waters, L. B. F. M., Tielens, A. G. G. M., & Barlow, M. J. 2002, *A&A*, 382, 184
- Molster, F. J., Waters, L. B. F. M., & Kemper, F. 2010, in *Astromineralogy, Lecture Notes in Physics*, vol. 815, ed. T. Henning (Berlin: Springer), 143
- Müller, H. S. P., Schlöder, F., Stutzki, J., & Winnewisser, G. 2005, *J. Mol. Struct.*, 742, 215
- Müller, H. S. P. & Woon, D. E. 2013, *J. Phys. Chem. A*, 117, 13868
- Muñoz, J., Rohmer, M.-M., Bénard, M., et al. 1999, *J. Phys. Chem. A*, 103, 4762
- Naumkin, F. Y. 2008, *J. Phys. Chem. A*, 112, 4660
- Neufeld, D. A., González-Alfonso, E., Melnick, G., et al. 2010, *A&A*, 521, L5
- Neufeld, D. A., González-Alfonso, E., Melnick, G., et al. 2011, *ApJ*, 727, L29
- Nittler, L. R., Alexander, C. M. O'D., Gao, X., et al. 1994, *Nature*, 370, 443
- Nittler, L. R., Alexander, C. M. O'D., Gao, X., et al. 1997, *ApJ*, 483, 475
- Ochterski, J. W., *Thermochemistry in Gaussian*, 2000; <http://gaussian.com/thermo/>
- Ohishi, M., Yamamoto, S., Saito, S., et al. 1988, *ApJ*, 329, 511
- Ohnaka, K., Weigelt, G., & Hofmann, K.-H. 2017, *A&A*, 597, A20
- Oike, T., Okabayashi, T., & Tanimoto, M. 1998, *J. Chem. Phys.*, 109, 3501
- Omont, A., Lucas, R., Morris, M., & Guilloteau, S. 1993, *A&A*, 267, 490
- Onaka, T., de Jong, T., & Willems, F. J. 1989, *A&A*, 218, 169
- O'Sullivan, P. J., Hamilton, P. A., Davies, P. B., et al. 2006, *J. Mol. Spectr.*, 235, 248
- Pardo, J. R., Alcolea, J., Bujarrabal, V., et al. 2004, *A&A*, 424, 145
- Perdew, J. P., Burke, K., & Ernzerhof, M. 1996, *Phys. Rev. Lett.*, 77, 3865
- Phelps, D. J. & Dalby, F. W. 1966, *Phys. Rev. Lett.*, 16, 3
- Posch, T., Kerschbaum, F., Mutschke, H., et al. 1999, *A&A*, 352, 609
- Posch, T., Kerschbaum, F., Mutschke, H., et al. 2002, *A&A*, 393, L7
- Presilla-Márquez, J. D., Gay, S. C., Rittby, C. M. L., & Graham, W. R. M. 1995, *J. Chem. Phys.*, 102, 6354
- Pulliam, R. L., Savage, C., Agúndez, M., et al. 2010, *ApJ*, 725, L181
- Pulliam, R. L. & Ziurys, L. M. 2010, *J. Chem. Phys.*, 133, 174313
- Quintana-Lacaci, G., Cernicharo, J., Agúndez, M., et al. 2016, *A&A*, 818, 192
- Quintana-Lacaci, G., Cernicharo, J., Velilla Prieto, L., et al. 2017, *A&A*, 607, L5
- Ram, R. S., Engleman Jr., R., & Bernath, P. F. 1998, *J. Mol. Spectr.*, 190, 341
- Ramstedt, S., Schöier, F. L., Olofsson, H., & Lindgren, A. A. 2008, *A&A*, 487, 645
- Ramstedt, S., Schöier, F. L., & Olofsson, H. 2009, *A&A*, 499, 515
- Reid, M. J. & Menten, K. M. 1997, *ApJ*, 476, 327
- Rintelman, J. M. & Gordon, M. S. 2001, *J. Chem. Phys.*, 115, 1795
- Robie, R. A., Hemingway, B. S., & Fisher, J. R. 1979, *Thermodynamic Properties of Minerals and Related Substances at 298.15 K and 1 Bar (10<sup>5</sup> Pascals) Pressure and at Higher Temperatures*, U.S. Geol. Survey Bull. 1452
- Ruscic, B., Feller, D., & Peterson, K. A. 2014, *Theor. Chem. Acc.*, 133, 1415
- Russell, H. N. 1934, *ApJ*, 79, 317
- Scarl, E. A. & Dalby, F. W. 1974, *Can. J. Phys.*, 52, 1429
- Schmidt, M. R., He, J. H., Szczerba, R., et al. 2016, *A&A*, 592, A131
- Schöier, F. L., Olofsson, H., & Lindgren, A. A. 2006, *A&A*, 454, 247
- Schöier, F. L., Bast, J., Olofsson, H., & Lindqvist, M. 2007, *A&A*, 473, 871
- Schöier, F. L., Maercker, M., Justtanont, K., et al. 2011, *A&A*, 530, A83
- Schöier, F. L., Ramstedt, S., Olofsson, H., et al. 2013, *A&A*, 550, A78
- Scurlock, C. T., Fletcher, D. A., & Steimle, T. C. 1993, *J. Mol. Spectr.*, 159, 350
- Sevy, A., Matthew, D. J., & Morse, M. D. 2018, *J. Chem. Phys.*, 149, 044306
- Sharkas, K., Gagliardi, L., & Truhlar, D. G. 2017, *J. Phys. Chem. A*, 121, 9392
- Sharp, C. M. & Wasserburg, G. J. 1995, *Geochim. Cosmochim. Acta*, 59, 1633
- Sheridan, P. M., Brewster, M. A., & Ziurys, L. M. 2002, *ApJ*, 576, 1108
- Shirley, J., Scurlock, C., & Steimle, T. 1990, *J. Chem. Phys.*, 93, 1568
- Sloan, G. C., Lagadec, E., Zijlstra, A. A., et al. 2014, *ApJ*, 791, 28
- Smith, V. V. & Lambert, D. L. 1985, *ApJ*, 294, 326
- Smith, V. V. & Lambert, D. L. 1986, *ApJ*, 311, 843
- Smolders, K., Neyskens, P., Blommaert, J. A. D. L., et al. 2012, *A&A*, 540, A72
- Snyder, L. C. 1974, *J. Chem. Phys.*, 61, 747
- Stanton, J. F., Dudek, J., Theulé, P., et al. 2005, *J. Chem. Phys.*, 122, 124314
- Stearns, C. A. & Kohl, F. J. 1974, NASA Technical Note TN D-7613
- Steimle, T. C., Nachman, D. F., Shirley, J. E., et al. 1989, *J. Chem. Phys.*, 91, 2049
- Steimle, T. C., Fletcher, D. A., Jung, K. Y., & Scurlock, C. T. 1992, *J. Chem. Phys.*, 96, 2556
- Steimle, T. C., Gengler, J., & Hodges, P. J. 2004, *J. Chem. Phys.*, 121, 12303
- Stock, J. W., Kitzmann, D., Patzer, A. B. C., & Sedlmayr, E. 2018, *MNRAS*, 479, 865
- Suenram, R. D., Lovas, F. J., Fraser, G. T., & Matsumura, K. 1990, *J. Chem. Phys.*, 92, 4724
- Suenram, R. D., Fraser, G. T., & Lovas, F. J. 1991, *J. Mol. Spectr.*, 148, 114
- Suh, K.-W. 2004, *ApJ*, 615, 485
- Szentpály, L. v. & Schwerdtfeger, P. 1990, *Chem. Phys. Lett.*, 170, 555
- Takano, S., Yamamoto, S., & Saito, S. 1989, *Chem. Phys. Lett.*, 159, 563
- Takano, S., Yamamoto, S., & Saito, S. 1991, *J. Chem. Phys.*, 94, 3355
- Takano, S., Saito, S., & Tsuji, T. 1992, *PASJ*, 44, 469
- Takano, S., Yamamoto, S., & Saito, S. 2004, *J. Mol. Spectr.*, 224, 137
- Tanimoto, M., Saito, S., Endo, Y., & Hirota, E. 1983, *J. Mol. Spectr.*, 100, 205
- Tanimoto, M., Saito, S., Endo, Y., & Hirota, E. 1984, *J. Mol. Spectr.*, 103, 330
- Tanimoto, M., Saito, S., & Hirota, E. 1986, *J. Chem. Phys.*, 84, 1210
- Tejero, J. & Cernicharo, J. 1991, *Modelos de Equilibrio Termodinámico Aplicados a Envolturas Circunestelares de Estrellas Evolucionadas* (Madrid: IGN)
- Tenenbaum, E. D., Woolf, N. J., & Ziurys, L. M. 2007, *ApJ*, 666, L29
- Tenenbaum, E. D. & Ziurys, L. M. 2010, *ApJ*, 712, L93
- Tiemann, E., Bojaschewsky, M., Sauter-Servaes, Ch., & Törring, T. 1974, *Z. Naturforsch. A*, 29, 1692
- Tiemann, E., Ryzlewicz, Ch., & Törring, T. 1976, *Z. Naturforsch. A*, 31, 128

- Töring, T. & Hoefft, J. 1986, *Chem. Phys. Lett.*, 126, 477
- Treffers, R. & Cohen, M. 1974, *ApJ*, 188, 545
- Tsuji, T. 1964, *Ann. Tokyo Astron. Observat.*, 9, 1
- Tsuji, T. 1973, *A&A*, 23, 411
- Tsuji, T., Ohnaka, K., Aoki, W., & Yamamura, I. 1997, *A&A*, 320, L1
- Turner, B. E., Steimle, T. C., & Meerts, L. 1994, *ApJ*, 426, L97
- Turney, J. M., Sari, L., Yamaguchi, Y., & Schaefer, H. F. 2005, *J. Chem. Phys.*, 122, 094304
- Van de Sande, M., Sundqvist, J. O., Millar, T. J., et al. 2018, *A&A*, 616, A106
- Van de Sande, M. & Millar, T. J. 2019, *ApJ*, 873, 36
- Vasiliiu, M., Feller, D., Gole, J. L., & Dixon, D. A. 2010, *J. Phys. Chem. A*, 114, 9349
- Velilla Prieto, L., Cernicharo, J., Quintana-Lacaci, G., et al. 2015, *ApJ*, 805, L13
- Velilla Prieto, L., Sánchez Contreras, C., Cernicharo, J., et al. 2017, *A&A*, 597, A25
- Vlemmings, W. H. T., Khouri, T., O’Gorman, E., et al. 2017, *Nature Astron.*, 1, 848
- Vlemmings, W. H. T., Khouri, T., & Olofsson, H. 2019, *A&A*, 626, A81
- Walker, K. A. & Gerry, M. C. L. 1997, *J. Mol. Spectr.*, 182, 178
- Wang, X. & Andrews, L. 2005, *J. Phys. Chem. A*, 109, 2782
- Wang, X. & Andrews, L. 2006, *J. Phys. Chem. A*, 110, 10035
- Wang, X. & Andrews, L. 2007, *J. Phys. Chem. A*, 111, 1860
- Wang, H., Zhuang, X., & Steimle, T. C. 2009, *J. Chem. Phys.*, 131, 114315
- Waters, L. B. F. M. 2011, in *Why Galaxies Care About AGB Stars II: Shining Examples and Common Inhabitants*, ed. F. Kerschbaum, T. Lebzelter, & R. F. Wing, *ASP Conf. Ser.* 445, 227
- Waters, L. B. F. M., Molster, F. J., de Jong, T., et al. 1996, *A&A*, 315, L361
- Wharton, L., Kaufman, M., & Klemperer, W. 1962, *J. Chem. Phys.*, 37, 621
- White, W. B., Johnson, S. M., & Dantzig, G. B. 1958, *J. Chem. Phys.*, 28, 751
- Willacy, K. & Cherchneff, I. 1998, *A&A*, 330, 676
- Willacy, K. 2004, *ApJ*, 600, L87
- Woitke, P., Helling, Ch., Hunter, G. H., et al. 2018, *A&A*, 614, A1
- Wong, K. T., Kamiński, T., Menten, K. M., & Wyrowski, F. 2016, *A&A*, 590, A127
- Wong, K. T., Menten, K. M., Kamiński, T., et al. 2018, *A&A*, 612, A48
- Woolf, N. J. & Ney, E. P. 1969, *ApJ*, 155, L181
- Woon, D. E. & Herbst, E. 2009, *ApJS*, 185, 273
- Yamamoto, T., Tanimoto, M., & Okabayashi, T. 2007, *PCCP*, 9, 3744
- Yamamura, I., de Jong, T., Onaka, T., et al. 1999, *A&A*, 341, L9
- Yamamura, I., Kawaguchi, K., & Ridgway, S. T. 2000, *ApJ*, 528, L33
- Yasuda, Y. & Kozasa, T. 2012, *ApJ*, 745, 159
- Yurchenko, S. N., Sinden, F., Lodi, L., et al. 2018, *MNRAS*, 473, 5324
- Zeidler, S., Posch, Th., & Mutschke, H. 2013, *A&A*, 553, A81
- Zeleznik, F. J. & Gordon, S. 1960, *NASA Technical Note D-473*
- Zhang, Ke, Jiang, B. W., & Li, A. 2009, *ApJ*, 702, 680
- Zhukovska, S. & Gail, H.-P. 2008, *A&A*, 486, 229
- Ziurys, L. M., Barclay Jr., W. L., & Anderson, M. A. 1992, *ApJ*, 384, L63
- Ziurys, L. M., Apponi, A. J., & Phillips, T. G. 1994, *ApJ*, 433, 729
- Ziurys, L. M., Apponi, A. J., Guélin, M., & Cernicharo, J. 1995, *ApJ*, 445, L47
- Ziurys, L. M., Schmidt, D. R., & Bernal, J. J. 2018, *ApJ*, 856, 169

## Appendix A: Element-by-element gas budget

Here we review the main gas-phase reservoirs of each element in AGB atmospheres according to chemical equilibrium. The calculations include only gaseous species and use as input the elemental composition given in Table 1 for AGB stars of M-, S-, and C-type and the pressure-temperature profile discussed in Sec. 2.4, which is taken as representative of AGB atmospheres. We do not discuss the noble gases He, Ne, and Ar, which are essentially present as neutral atoms, nor hydrogen, which is mostly present as  $H_2$  with the exception of the hot inner atmosphere ( $> 1700$  K for our adopted pressure-temperature profile) where H is more abundant. The remaining elements we include comprise the nonmetals B, C, N, O, F, Si, P, S, and Cl, metals such as Al, the alkali metals Li, Na, K, and Rb, the alkali-earth metals Be, Mg, Ca, Sr, and Ba, and the transition metals Sc, Ti, V, Cr, Mn, Fe, Co, Ni, Cu, Zn, and Zr.

The importance of the various types of reservoirs, either atomic, molecular, or in the form of condensates, is different for each element. Here we focus solely on the gas-phase budget and do not consider condensates. However, as discussed in Sec. 5, most elements, especially metals, tend to form thermodynamically stable condensates below a given temperature. We therefore recall that in regions in which the temperature has dropped below the relevant condensation temperature for each element, the abundance of the element in the gas phase must decrease, and all the abundances calculated here for the gaseous species should therefore be scaled down in these regions.

Nonmetals in the gas-phase budget in general tend to be in molecular form, although neutral atoms can also be a major reservoir in the hot inner atmosphere for many of them, such as C, Si, and B in carbon-rich stars, O and S in oxygen-rich stars, and P and Cl regardless of the C/O. For metals, the atomic reservoir tends to be more important than for nonmetals. Ionized atoms can be abundant in the hottest regions, and neutral atoms frequently largely dominate any molecular form throughout the entire extended atmosphere. We caution, however, that for some metals the number of molecules for which thermochemical data are available is small and therefore important molecular reservoirs of metals might be missed.

### Appendix A.1: Carbon

The main gas reservoirs of carbon are shown in the two upper panels of Fig. A.1. Most carbon is in the form of CO. This implies that M-type stars, which have  $C/O < 1$ , have no carbon-bearing molecule with a significant abundance, with the exception of  $CO_2$ . On the other hand, in C-type stars, where the C/O is higher than one, a great variety of carbon-bearing molecules are formed with large abundances. These include pure carbon clusters, hydrocarbons, and different stable molecules in which a carbon atom is bonded to a nonmetal, such as N, S, Si, or P, or to a metal, such as Na, K, Al, or Ti. The situation for S-type stars with C/O equalling one resembles that of C-type stars, but the abundances of carbon-bearing molecules are scaled down by some orders of magnitude.

In C-type stars, the main reservoir of carbon that is not locked into CO is atomic in the hot innermost atmosphere and  $C_2H_2$  elsewhere. Only at large radii ( $> 10 R_*$ ) does  $CH_4$  become the main reservoir, although it is unlikely that chemical equilibrium regulates the chemical composition at such large radii. At large radii, polycyclic aromatic hydrocarbons (PAHs) have also been predicted to become important carriers of carbon (Tejero & Chernicharo 1991; Cherchneff & Barker 1992). However, PAHs

are not observed in envelopes around AGB stars, and thus it is uncertain whether they effectively form in these environments. Other main reservoirs of carbon are HCN, CS, and  $C_3$ , while at a given distance from the star ( $3-5 R_*$ ), silicon, titanium, and aluminum carbides of medium to large size ( $SiC_2$ ,  $Si_2C$ ,  $Si_3C$ ,  $Si_5C$ ,  $Ti_8C_{12}$ , and  $Al_2C_2$ ) become increasingly abundant.

### Appendix A.2: Oxygen

In the two lower panels of Fig. A.1 we show the calculated abundances of the most abundant oxygen-bearing molecules. Similarly to the case of carbon, the very high abundance of CO in this case causes a lack of O-bearing species in C-type stars, with the exception of SiO and  $Al_2O$ , which become abundant reservoirs of silicon and aluminum, respectively, at large radii. In contrast, in oxygen-rich atmospheres, many different O-bearing molecules are formed abundantly, mostly consisting of oxides, hydroxides, and inorganic acids. Excluding CO, most oxygen is atomic in the surroundings of the AGB star and in the form of  $H_2O$  elsewhere. Additional important reservoirs of oxygen are the radical OH, which is very abundant in the hot inner atmosphere, and SiO, which is a very stable molecule that locks most of the silicon. Other molecules present at a lower level of abundance are AlOH,  $CO_2$ , SO, and PO. At large radii ( $> 5 R_*$ ), polyatomic molecules such as the hydroxides  $Al(OH)_3$  and  $Ca(OH)_2$ , also become quite abundant. In S-type stars the situation resembles that of carbon stars, with a paucity of oxygen-bearing molecules, and only SiO and  $Al_2O$  reach relatively high abundances.

### Appendix A.3: Nitrogen

The main reservoir of nitrogen in AGB atmospheres, regardless of the C/O, is clearly  $N_2$  (see the top panel in Fig. A.2). Unfortunately, this species is very difficult to detect and has never been observed in the atmosphere or envelope of an AGB star. Only HCN competes with  $N_2$  in abundance in carbon-rich atmospheres, and to a lower extent, in S-type atmospheres. Neutral atoms are not an important reservoir of nitrogen because they would need temperatures in excess of 3000 K to compete in abundance with  $N_2$ . Other nitrogen-bearing molecules are present at a lower level. The metastable isomer HNC and the radical CN reach relatively high abundances, comparable to or somewhat lower than that of HCN, in the hottest inner atmosphere of S- and C-type stars, although the HNC-to-HCN and CN-to-HCN abundance ratios experience a steep decline with decreasing temperature, and thus with increasing radius. At large radii ( $> 5 R_*$ ), molecules such as SiNH and the metal cyanides NaCN and KCN reach non-negligible abundances in S- and C-type stars. In oxygen-rich atmospheres, the only N-bearing molecule that reaches a non-negligible abundance except for  $N_2$  is NO, which is calculated with a mole fraction of  $\sim 10^{-8}$  in the inner atmosphere, although this rapidly decreases with increasing radius.

### Appendix A.4: Silicon

The calculated abundances of Si-bearing species are shown in the two lower panels of Fig. A.2. The main carrier of silicon in M-type atmospheres is clearly SiO, while SiS and  $SiS_2$  also become abundant at large radii ( $> 5 R_*$ ). In C-type atmospheres, atomic silicon in the inner atmosphere and SiS in the outer parts are the most abundant reservoirs. SiO is also an important Si-

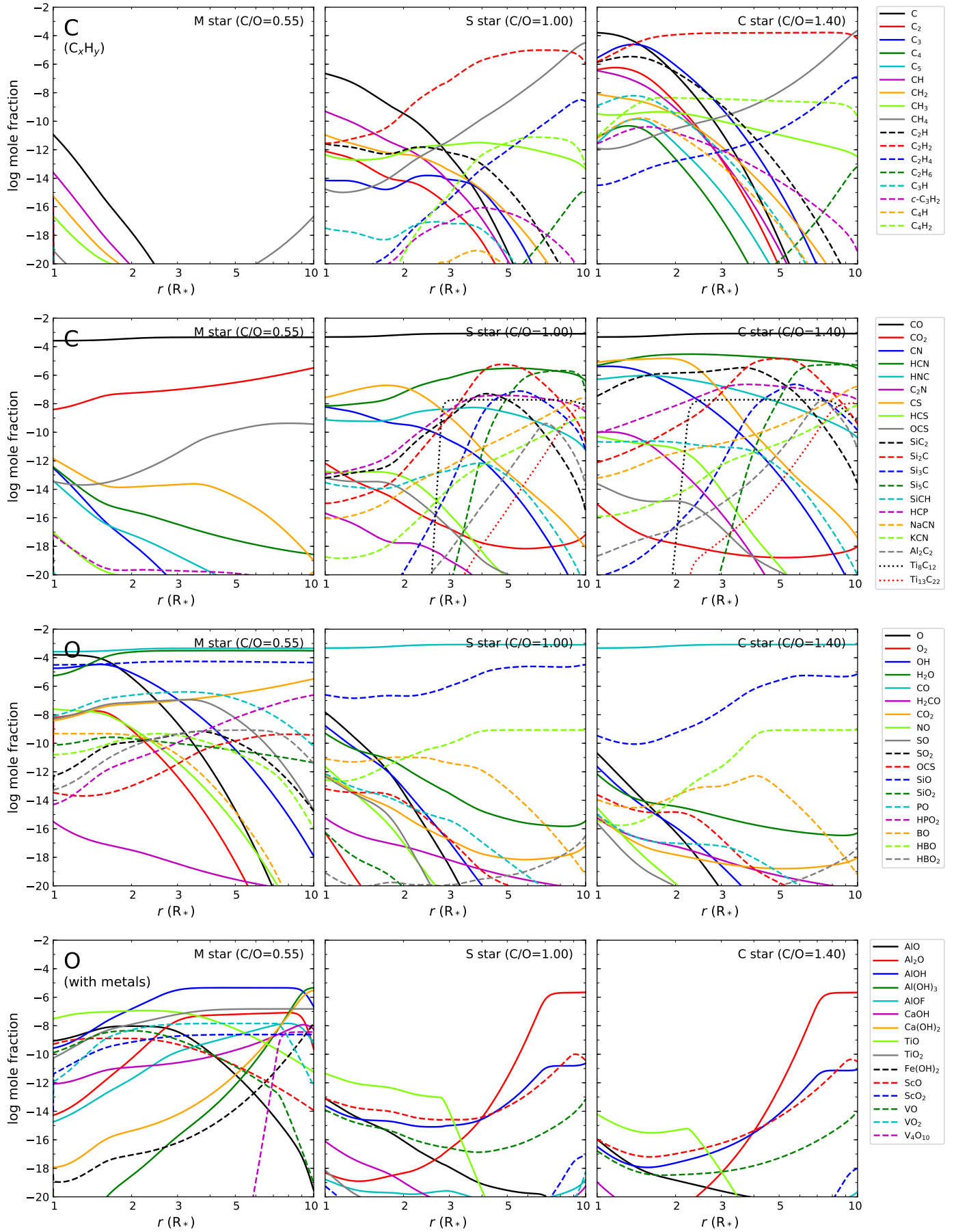


**Fig. A.1.** Chemical equilibrium abundances of species containing C (upper panels) and O (lower panels) in M-, S-, and C-type AGB atmospheres.

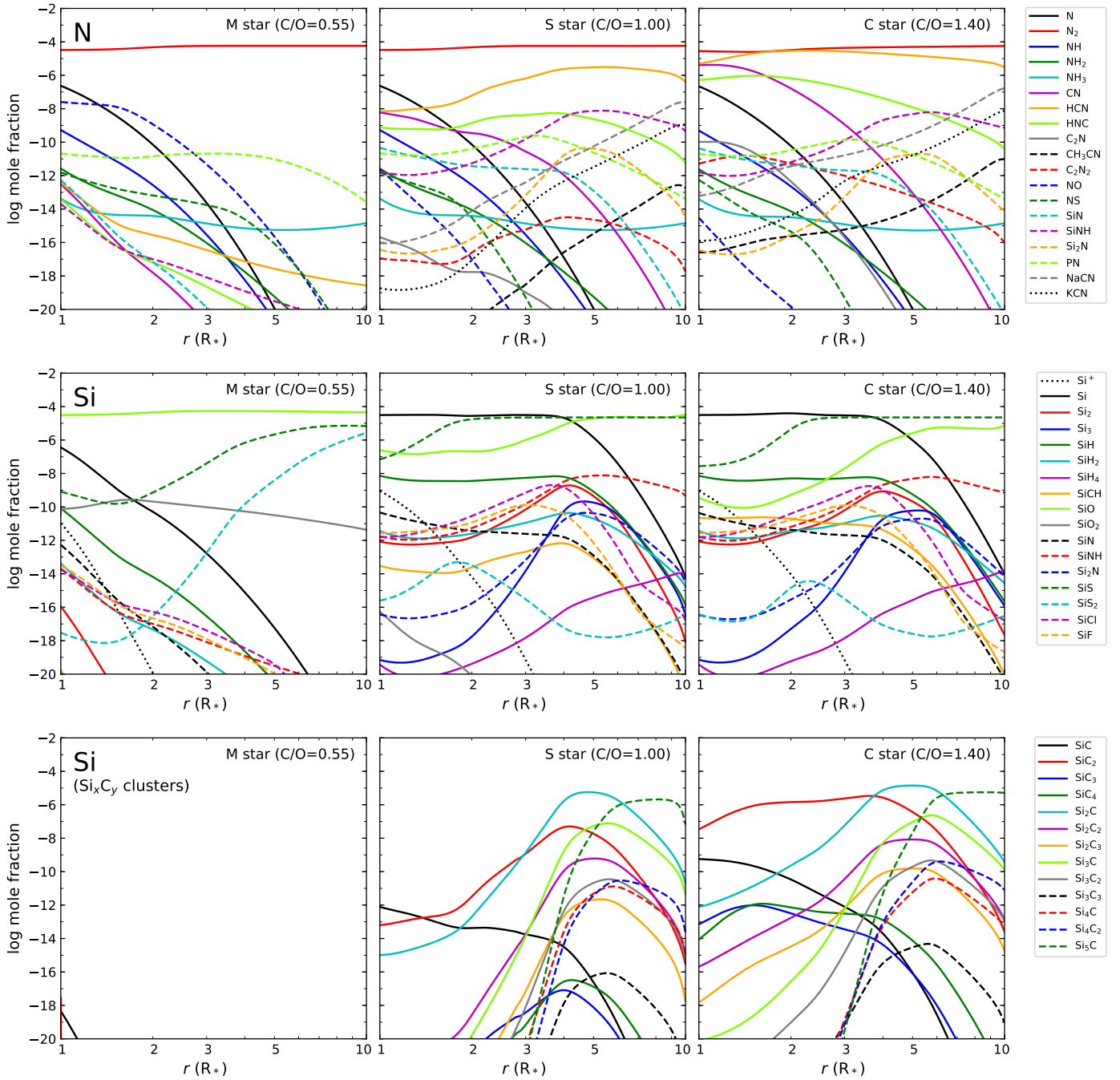


**Fig. A.2.** Chemical equilibrium abundances of species containing N and Si in M-, S-, and C-type AGB atmospheres.

bearing species in carbon-rich atmospheres, but it only reaches a high abundance, slightly below that of SiS, beyond  $\sim 5 R_*$ . In the atmospheres around S-type stars, the three species Si, SiS, and SiO are all main reservoirs of silicon, each in a different region.

In carbon-rich atmospheres, the availability of carbon that is not locked into CO brings a variety of silicon-carbon clusters of the type  $\text{Si}_x\text{C}_y$ , some of them with very high abundances (see bottom panel of Fig. A.2). The most abundant are clearly  $\text{SiC}_2$ ,  $\text{Si}_2\text{C}$ , and  $\text{Si}_5\text{C}$ , the latter being a main reservoir only at large radii ( $> 6 R_*$ ). Other clusters predicted at a lower level are  $\text{Si}_3\text{C}$  and  $\text{Si}_2\text{C}_2$ . The calculated abundances are on the same order as those reported by Yasuda & Kozasa (2012), who also used thermochemical data for  $\text{Si}_x\text{C}_y$  clusters from Deng et al. (2008). These silicon-carbon clusters are also present in S-type atmo-

spheres with abundances comparable to or somewhat lower than in carbon-rich atmospheres, while they are completely absent in oxygen-rich atmospheres.

#### Appendix A.5: Sulfur

The calculated abundances of sulfur-bearing species are shown in the two upper panels of Fig. A.3. Atomic sulfur is the main reservoir of this element in the inner atmosphere of M-type stars and also for S-type stars, although it is restricted to a smaller region around the star. In carbon-rich atmospheres, CS replaces atomic sulfur as the main reservoir in the inner atmosphere. The other main carrier of sulfur in S- and C-type stars is SiS, while in M-type stars molecules such as  $\text{S}_2$ ,  $\text{H}_2\text{S}$ , and SiS lock most of the

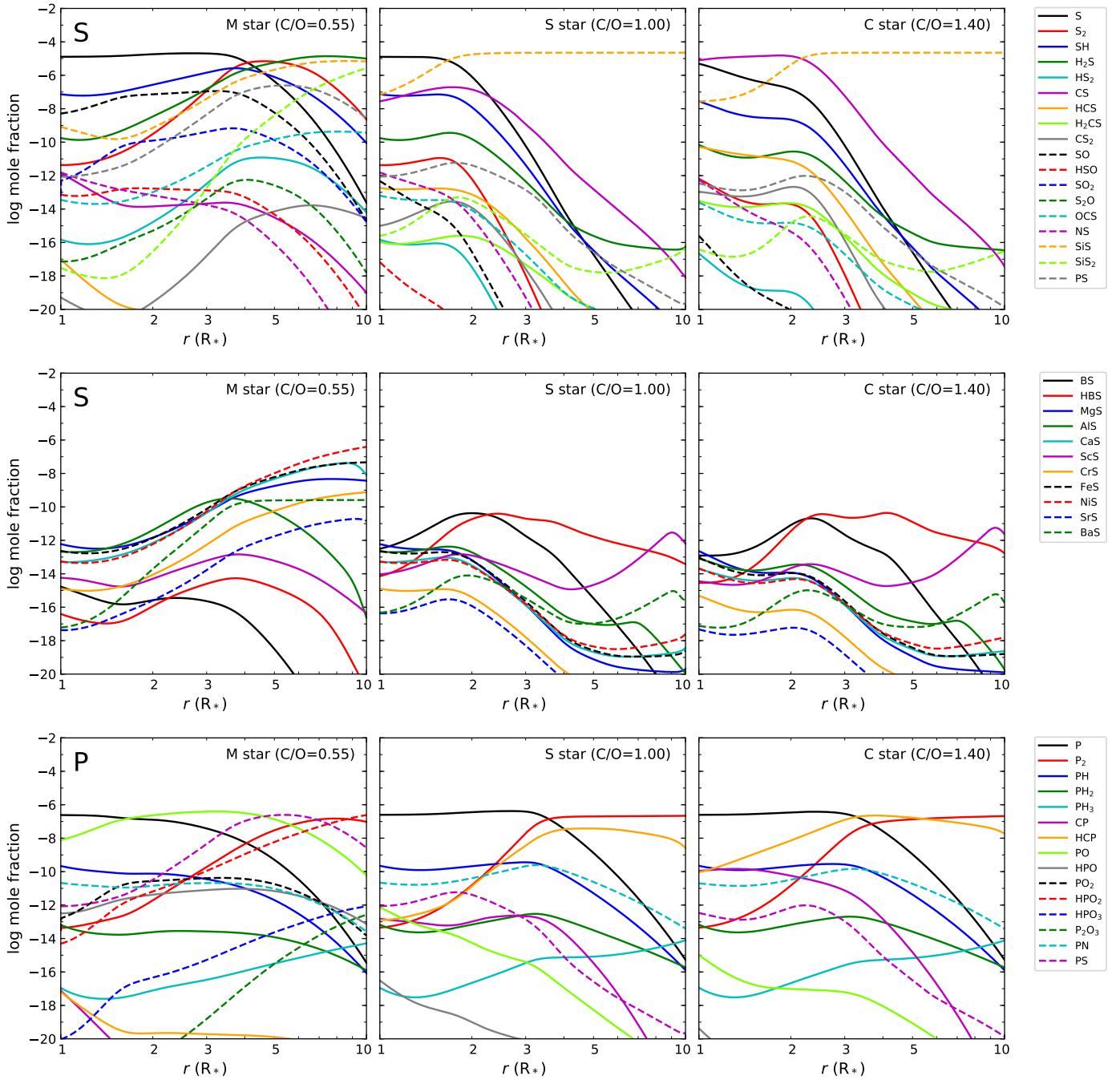


**Fig. A.3.** Chemical equilibrium abundances of species containing S and P in M-, S-, and C-type AGB atmospheres.

sulfur in the region in which atomic S drops in abundance. The radical SH is also an important S-bearing species, especially in M-type stars, where SO, PS, and SiS<sub>2</sub> also trap a non-negligible amount of sulfur.

#### Appendix A.6: Phosphorus

In the bottom panel of Fig. A.3 we show the calculated abundances of the most abundant P-bearing molecules. Most of the phosphorus is atomic in the inner atmosphere of S- and C-type stars, while at larger radii ( $> 3 R_*$ ), the molecules HCP and P<sub>2</sub> become the main carriers of this element. In M-type stars, atomic P is the main reservoir only very closely to the star, and molecules

such as PO, PS, P<sub>2</sub>, and HPO<sub>2</sub> (the latter only at large radii,  $\sim 10 R_*$ ) lock most of the phosphorus.

The calculations presented here differ somewhat from those presented in a previous study by Agúndez et al. (2007). For example, our calculations indicate that in carbon-rich atmospheres, P, P<sub>2</sub>, and HCP are all main carriers of phosphorus, while the calculations carried out by Agúndez et al. (2007) indicated that HCP is the main and almost exclusive reservoir of this element. The reason for the difference most likely is the formation enthalpy of HCP. The value at 298.15 K given in the NIST-JANAF compilation (Chase 1998) is  $149.9 \pm 63 \text{ kJ mol}^{-1}$  (note the substantial uncertainty). The thermochemical data adopted here for HCP is taken from the Third Millennium Thermochemical Database (Goos, Burcat, & Ruscic) and use a substantially

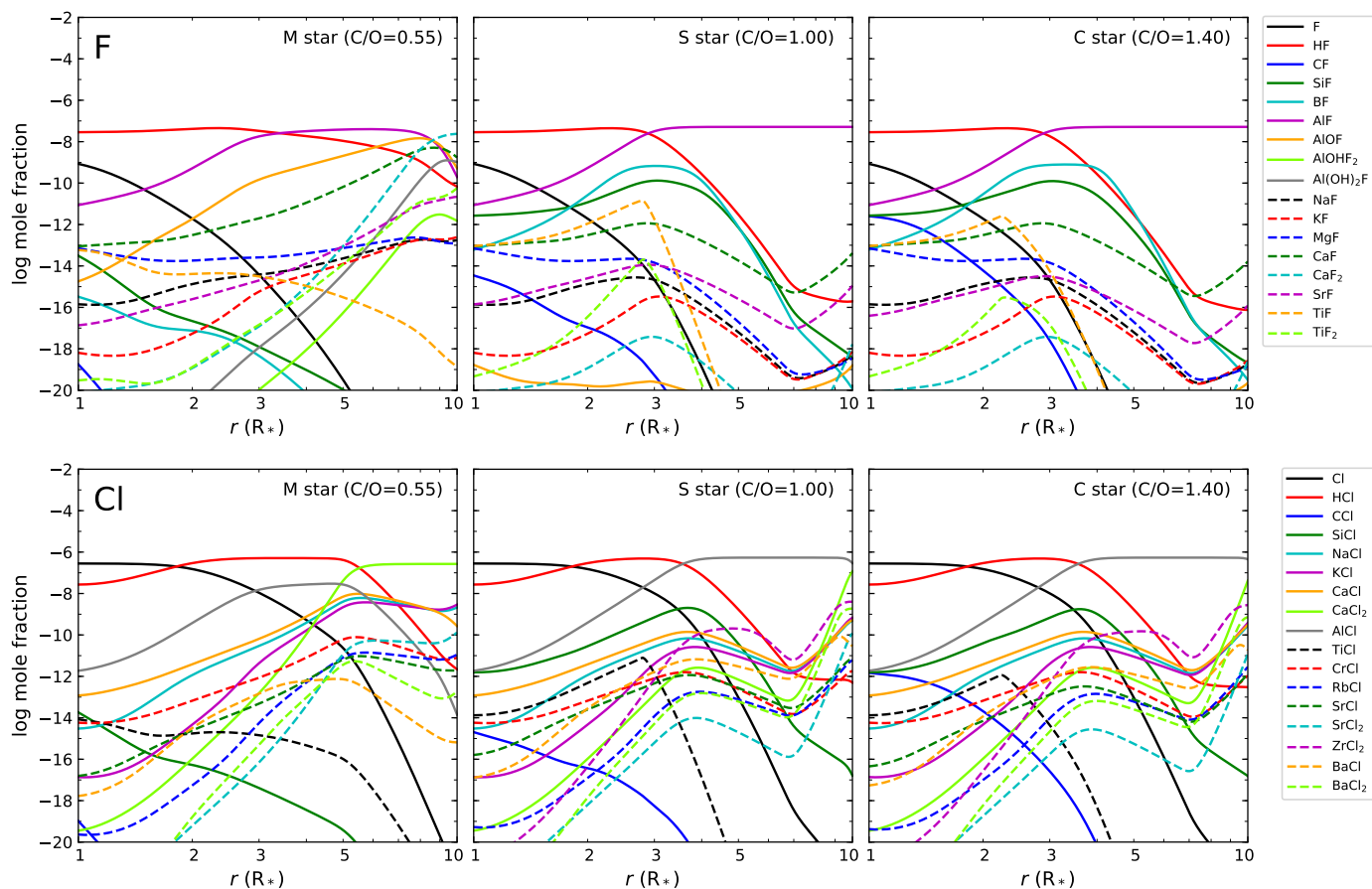


**Fig. A.4.** Chemical equilibrium abundances of species containing F and Cl in M-, S-, and C-type AGB atmospheres.

higher formation enthalpy,  $216 \text{ kJ mol}^{-1}$ , based on a more recent revision (see NIST CCCBDB<sup>5</sup>). Another important difference concerns  $\text{P}_4\text{O}_6$ , for which Agúndez et al. (2007) found that it is the main reservoir of phosphorus beyond  $\sim 4 R_*$  in oxygen-rich atmospheres. Here we find a negligible abundance for this species. The reason is again related to the formation enthalpy. The NIST-JANAF compilation (Chase 1998) gives a value at 298.15 K of  $-2214.3 \pm 33.5 \text{ kJ mol}^{-1}$ . The Third Millennium Thermochemical Database (Goos, Burcat, & Ruscic) states that the latter value is erroneous and uses a much higher value,  $-1606 \text{ kJ mol}^{-1}$ , from the compilation of Gurvich et al. (1989).

#### Appendix A.7: Fluorine

The main gas reservoirs of fluorine are shown in the top panel of Fig. A.4. The budget of this element in AGB atmospheres is relatively simple and remarkably independent of the C/O. Atomic fluorine only becomes the main reservoir at temperatures above  $\sim 3250 \text{ K}$  and thus is not an important reservoir in cool AGB stars. Most of the fluorine is locked by HF in the inner atmosphere, while AlF becomes the main carrier of this element at radii larger than  $\sim 3 R_*$ . This applies to M-, S-, and C-type stars. In M-type stars, at radii as large as  $10 R_*$ , metal-containing molecules such as AlOF, CaF, and  $\text{CaF}_2$  can trap important amounts of fluorine.

#### Appendix A.8: Chlorine

The calculated abundances of Cl-bearing species are shown in the lower panel of Fig. A.4. The situation for chlorine, with HCl and AlCl as major reservoirs, somewhat resembles that of fluorine, although there are some important differences. In this case, atomic chlorine is an important reservoir of the element in the inner atmosphere. For our adopted pressure-temperature profile, atomic chlorine is the main carrier for temperatures above  $\sim 1750 \text{ K}$  and HCl dominates at lower temperatures, regardless of the C/O. At radii larger than  $3\text{--}4 R_*$ , the chlorine budget is different depending on the C/O. In this region, AlCl becomes the most abundant Cl-bearing species in S- and C-type atmospheres, while for M-type stars,  $\text{CaCl}_2$  replaces AlCl as the most important reservoir of this element. Chlorine tends to form relatively stable metal chlorides. In addition to the aforementioned AlCl and  $\text{CaCl}_2$ , metal chlorides such as CaCl, NaCl, KCl, SiCl, and  $\text{ZrCl}_2$  are formed to different extents depending on the C/O.

#### Appendix A.9: Boron

In the upper panel of Fig. A.5 we show the most abundant species containing boron. The low abundance of this element,  $5 \times 10^{-10}$  relative to H makes the observation of B-containing species difficult. No such species has been observed to date in the atmosphere or envelope of an AGB star. Boron is essentially in atomic form in the inner atmosphere of S- and C-type atmospheres. However, at a relatively short distance from the star ( $\sim 2 R_*$ ), the molecules BF and HBO become the main carriers of the element. In the atmospheres of M-type stars the situation is dif-

<sup>5</sup> <https://cccbdb.nist.gov/>

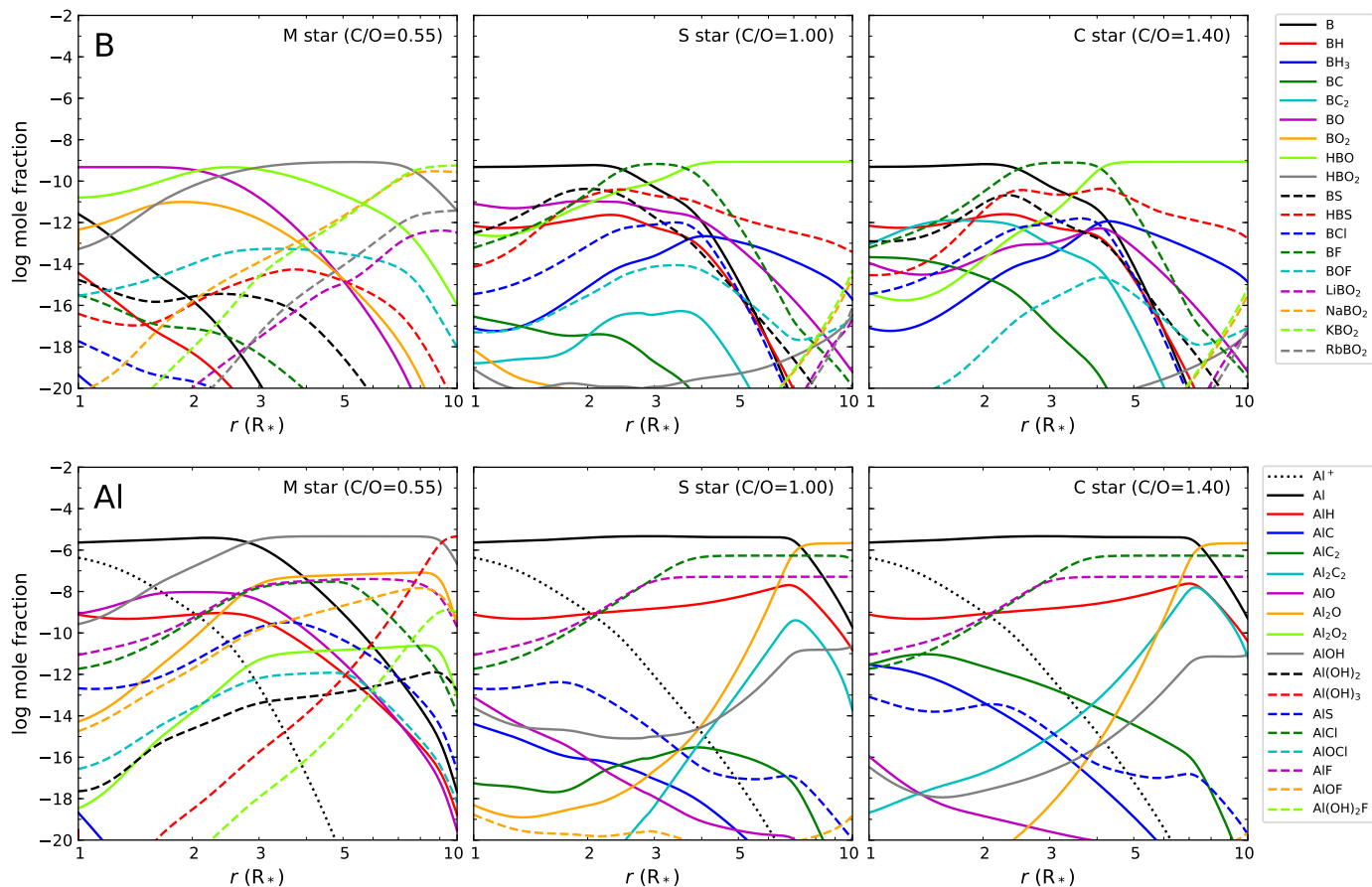


**Fig. A.5.** Chemical equilibrium abundances of species containing B and Al in M-, S-, and C-type AGB atmospheres.

ferent. Atomic boron is not a main carrier, and the molecules BO, HBO, and HBO<sub>2</sub> take most of the element. At radii larger than 7-8  $R_*$ , where chemical equilibrium is less likely to hold, the alkali metaborate species NaBO<sub>2</sub> and KBO<sub>2</sub> are predicted to be the main reservoirs of boron in oxygen-rich atmospheres.

#### Appendix A.10: Aluminum

The aluminum budget is shown in the lower panel of Fig. A.5. This element is mostly in the form of neutral atoms at the photosphere of AGB stars, regardless of the C/O, while Al<sup>+</sup> is the second most abundant carrier and becomes the main reservoir for temperatures above  $\sim 3000$  K. At distances larger than a few stellar radii, atomic aluminum begins to become less abundant in favor of molecules. In M-type atmospheres, hydroxides such as AlOH and Al(OH)<sub>3</sub>, the latter only at large radii ( $> 9 R_*$ ), are main carriers of aluminum, while molecules such as AlO, Al<sub>2</sub>O, AlCl, and AlF are also predicted to trap a significant fraction of the element. In the atmospheres of S- and C-type stars, the main molecular reservoirs of aluminum are the halides AlCl and AlF, together with Al<sub>2</sub>O at radii larger than  $\sim 7 R_*$ .

#### Appendix A.11: Alkali metals: Li, Na, K, and Rb

The calculated abundances of species containing the alkali metals Li, Na, K, and Rb are shown in Fig. A.6. The four elements show a similar behavior. That is, most of the element is in atomic rather than in molecular form. Ionized atoms are the main reservoir at the photosphere, while neutral atoms dominate from ra-

dial distances not too far from the AGB star. The importance of ionized atoms increases with atomic number, following the decrease in the ionization energy. The most important molecular reservoir for all the alkali metals are chlorides. In the case of lithium, LiCl even becomes the main carrier of Li at large radii, especially in M-type atmospheres. For Na, K, and Rb, the corresponding chloride (NaCl, KCl, and RbCl, respectively) trap a significant fraction of the alkali metal regardless of the C/O. In S- and C-type atmospheres, the cyanides NaCN and KCN also become abundant at large radii, while in M-type atmospheres, the alkali metaborate species LiBO<sub>2</sub>, NaBO<sub>2</sub>, KBO<sub>2</sub>, and RbBO<sub>2</sub> are also important carriers of alkali metals.

In general, molecules are not the main reservoirs of alkali metals. However, the high elemental abundance of Na and K ( $\sim 10^{-6}$  and  $\sim 10^{-7}$  relative to H, respectively) makes it possible to observe molecules such as NaCl, KCl, NaCN, and KCN in envelopes of AGB stars. In the case of Li and Rb, they can experience significant abundance enhancements compared to the Sun in some AGB stars, but their mean abundances remain low ( $\sim 10^{-12}$  for Li and  $\sim 10^{-10}$  for Rb, relative to H), which makes it difficult to detect molecules such as LiCl and RbCl.

#### Appendix A.12: Alkali-earth metals: Be, Mg, Ca, Sr, and Ba

In Fig. A.7 we show the calculated abundances of species containing the alkali-earth metals Be, Mg, Ca, Sr, and Ba. As with alkali metals, alkali-earth metals are mostly in atomic form in the photosphere of AGB stars and also to a large extent in the remaining extended atmosphere. Moreover, as occurs for alkali

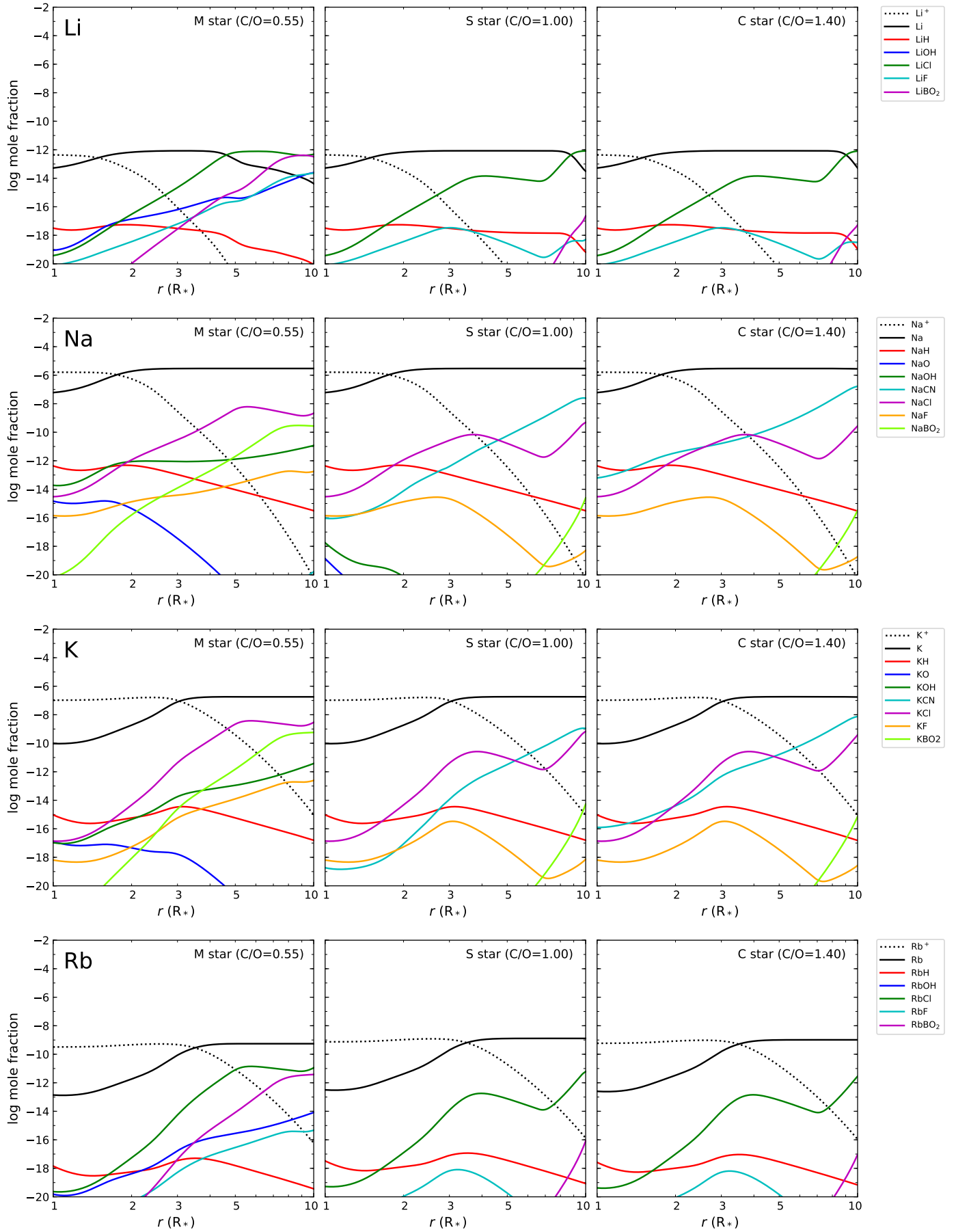
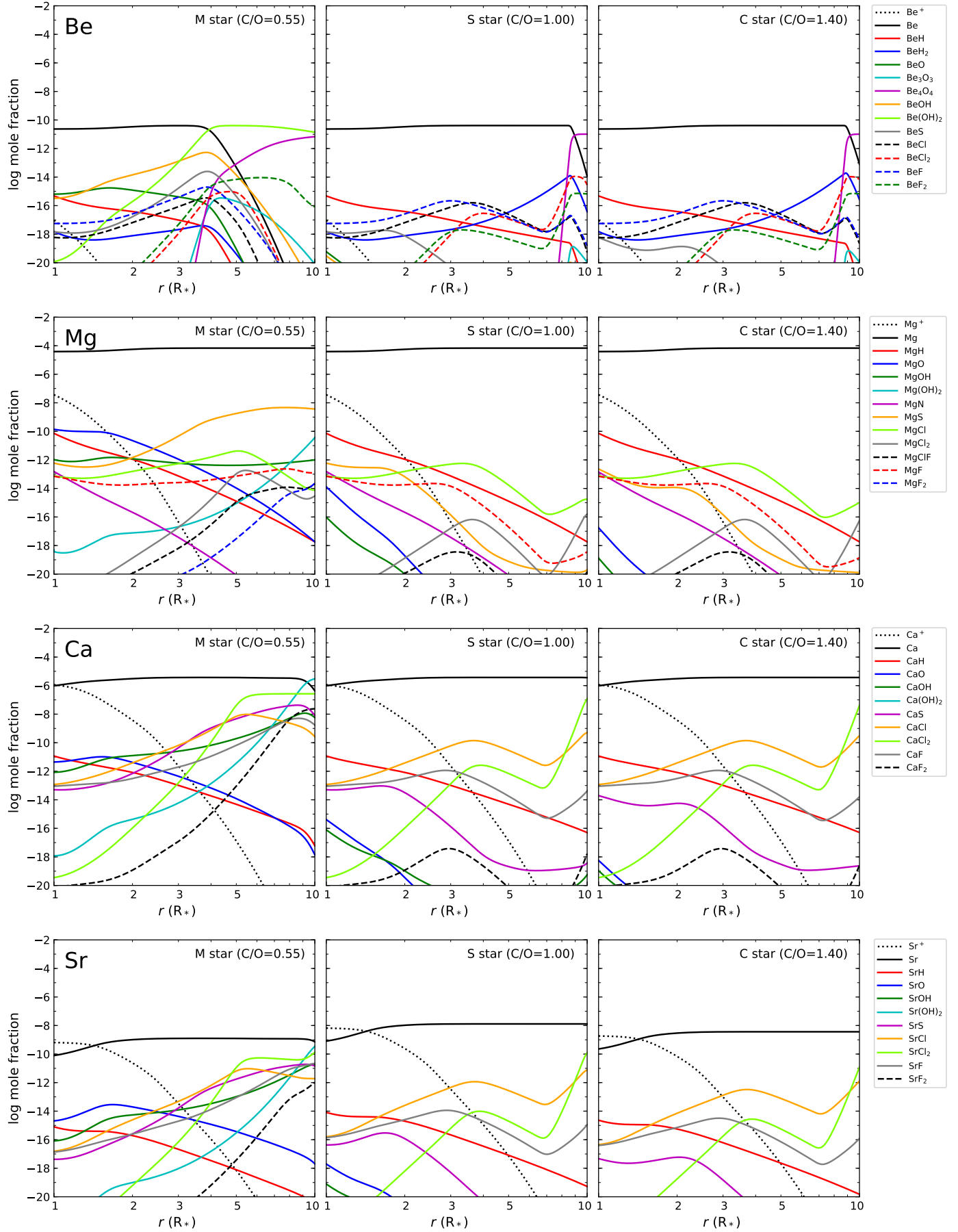


Fig. A.6. Chemical equilibrium abundances of species containing alkali metals in M-, S-, and C-type AGB atmospheres.



**Fig. A.7.** Chemical equilibrium abundances of species containing alkali-earth metals in M-, S-, and C-type AGB atmospheres.

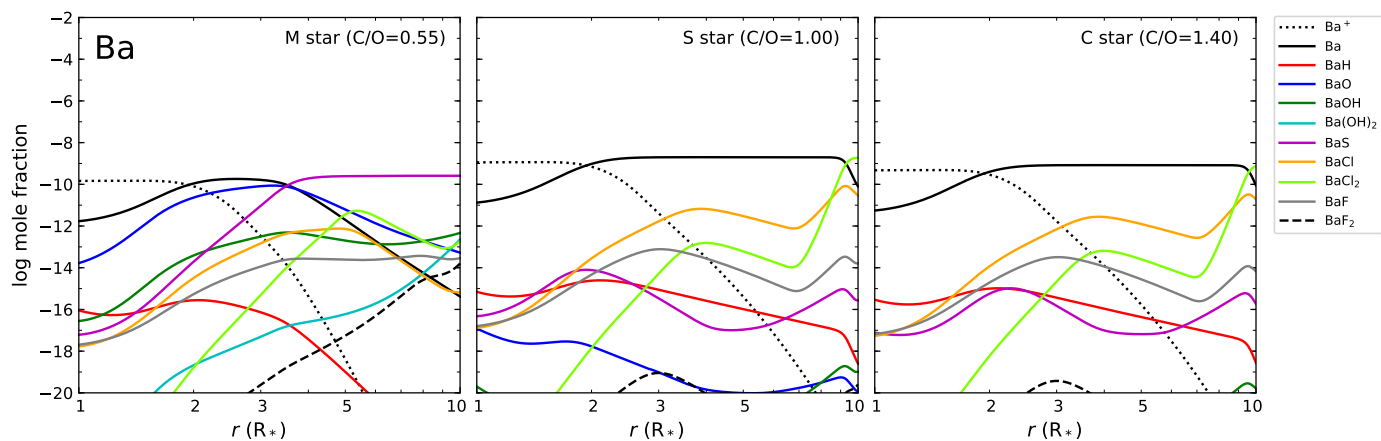


Fig. A.7. Continued.

metals, ionized atoms become increasingly important with increasing atomic number, and thus decreasing ionization energy. They are of little importance for Be, but are a main reservoir in the case of Ba. Molecules can also trap a larger or smaller fraction of the alkali-earth metal depending on each element and on the radial distance from the AGB star.

Beryllium is essentially in the form of neutral atoms in S- and C-type atmospheres, while in M-type stars, molecules such as  $\text{Be}(\text{OH})_2$  and  $\text{Be}_4\text{O}_4$  become main reservoirs of this element beyond  $\sim 4 R_*$ . The abundances reached by these molecules are low, however, because the intrinsic abundance of Be is low ( $\sim 10^{-11}$  relative to H).

In the case of magnesium, neutral atoms are clearly the main reservoir throughout the entire extended atmosphere for any C/O. The only Mg-bearing molecules that are present with non-negligible abundances are MgS and MgO, which reach mole fractions between  $\sim 10^{-10}$  and a few times  $10^{-9}$  in oxygen-rich atmospheres. In S- and C-type atmospheres, Mg-bearing molecules are largely absent.

Calcium is also mostly atomic in AGB atmospheres regardless of the C/O. However, some molecules such as CaOH,  $\text{Ca}(\text{OH})_2$ , CaS, CaCl,  $\text{CaCl}_2$ , CaF, and  $\text{CaF}_2$  form with relatively high abundances, especially in oxygen-rich atmospheres. In S- and C-type atmospheres, no Ca-bearing molecule is predicted with a significant abundance, except for CaCl and  $\text{CaCl}_2$  at large radii ( $\sim 10 R_*$ ).

The situation of Sr resembles that of Ca; atoms are the main reservoir, and some hydroxides, halides, and monosulfide trap a fraction of Sr in oxygen-rich atmospheres. As an s-process element, the abundance of Sr is higher in AGB atmospheres than in the Sun, but it is still substantially lower than that of Ca, resulting in very low mole fractions for Sr-bearing molecules ( $< 10^{-10}$ ) and low probabilities for detecting any of them.

The last alkali-earth metal included is Ba. Similarly to Ca and Sr, most barium is atomic in AGB atmospheres, although in M-type atmospheres BaO and BaS emerge as two important reservoirs of this element, with mole fractions of about  $10^{-10}$ . There is evidence of BaO in M-type atmospheres from near-infrared spectra (Dubois 1977). Dubois (1977) also identified BaF and BaCl in M- and S-type atmospheres, respectively, although our calculations show low abundances for these halides. Their presence in such atmospheres might be a consequence of an enhancement in the abundance of the s-process element Ba over the values adopted by us.

### Appendix A.13: Transition metals: Sc, Ti, Zr, V, Cr, Mn, Fe, Co, Ni, Cu, and Zn

The calculated abundances of species containing transition metals are shown in Fig. A.8 (Sc, Ti, Zr, and V), Fig. A.9 (Cr, Mn, Fe, and Co), and Fig. A.10 (Ni, Cu, and Zn). In general, transition metals tend to be mostly as neutral atoms in S- and C-type atmospheres, while in oxygen-rich atmospheres, neutral atoms and oxides are important reservoirs. There seems to be a trend: from left to right in the periodic table, the abundance of oxides in M-type atmospheres decreases in favor of atoms or other molecules such as sulfides and hydrides. For example, oxides are a main reservoir for Sc, Ti, Zr, and V, but not for Cr, Mn, Fe, Ni, Cu, or Zn. These generic conclusions are to be taken with caution, however, because there might be an important problem of completeness regarding the metal-bearing molecules for which thermochemical data is available. An example of this is illustrated by the case of titanium, in which the availability of thermochemical data for the many titanium-carbon clusters computed in this work reveals that some large  $\text{Ti}_x\text{C}_y$  clusters become the main reservoir of titanium in S- and C-type stars over a large part of the atmosphere. The same might also hold true for other metals for which thermochemical data of metal-carbon clusters are currently lacking. Another example is provided by cobalt, for which thermochemical data are only available for a few Co-bearing molecules such as CoH and some halides. Unlike the remaining transition metals, cobalt is predicted to be essentially present as CoH. However, the situation may change when Co-bearing molecules such as oxides or sulfides, for which thermochemical data are currently lacking, are included in the calculation.

The Sc, Ti, Zr, and V budgets (shown in Fig. A.8) share some similarities. In S- and C-type atmospheres, the metal is mostly in the form of neutral atoms. This is clearly the case of Sc and V, although for Ti and Zr some molecules become main carriers of the metal over a certain region of the atmosphere. In the case of Ti, large titanium-carbon clusters (mostly  $\text{Ti}_8\text{C}_{12}$ ) trap most of the Ti at radii larger than  $\sim 2 R_*$ , while for Zr, the molecules ZrO and  $\text{ZrCl}_2$  are also main carriers of Zr at radial distances  $> 6 R_*$ . We note, however, that if thermochemical data were available for metal-carbon clusters  $\text{M}_x\text{C}_y$  (where M stands for the metal) involving Sc, Zr, and V, the budget of these elements in S- and C-type atmospheres might be different. In oxygen-rich atmospheres, the oxides MO and  $\text{MO}_2$  are the main reservoirs of the transition metal. The oxides of the most abun-

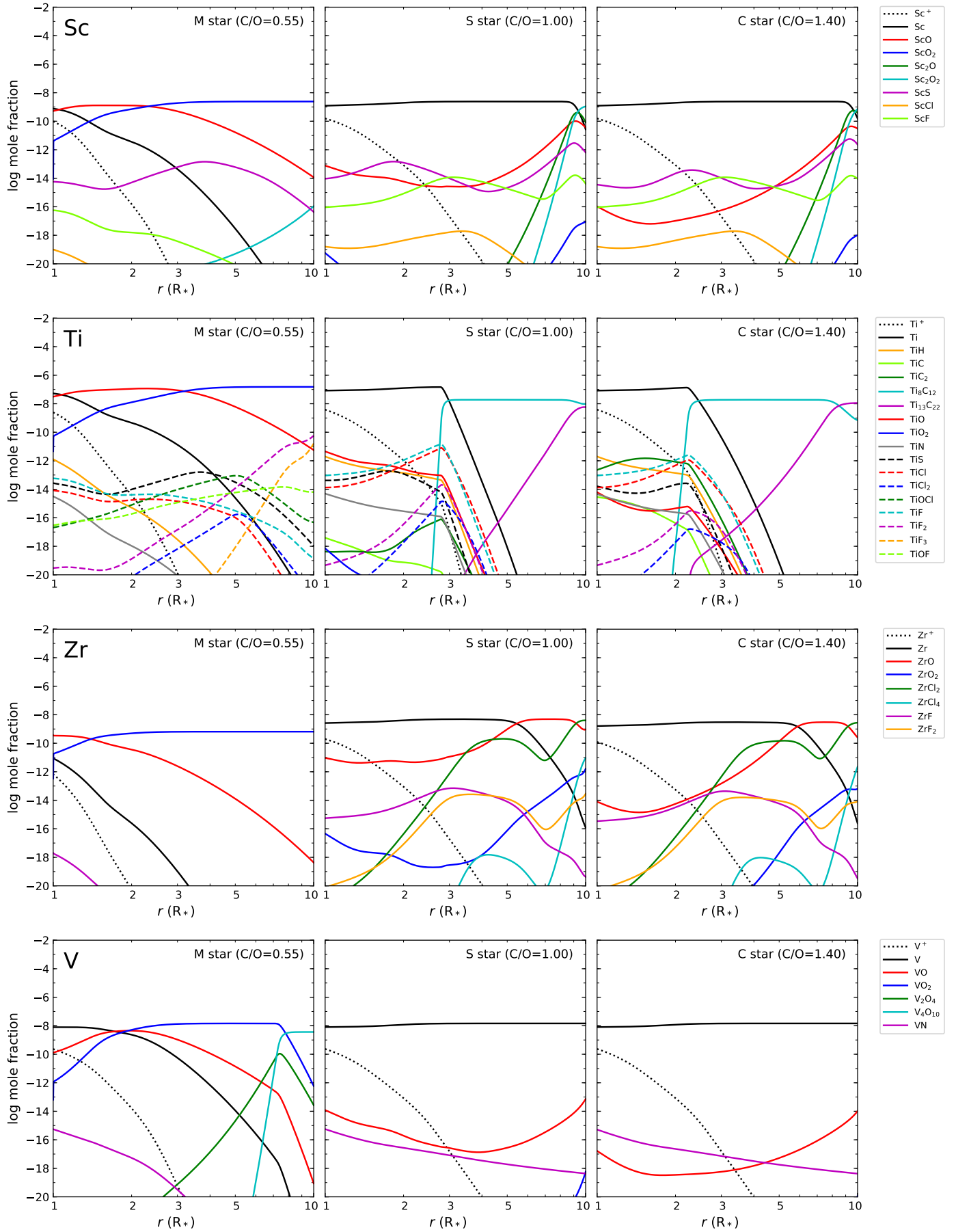


**Fig. A.8.** Chemical equilibrium abundances of species containing Sc, Ti, Zr, and V in M-, S-, and C-type AGB atmospheres.

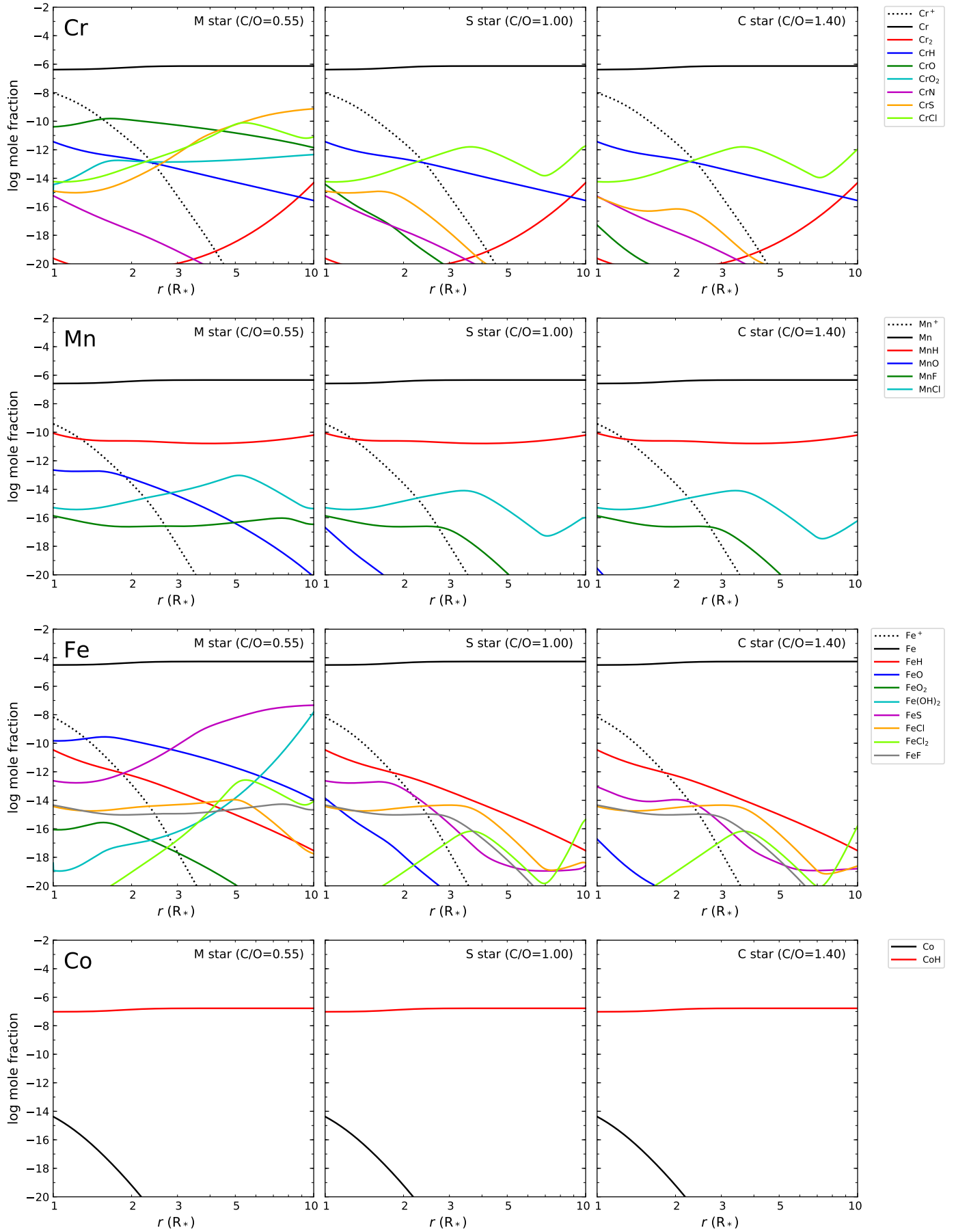
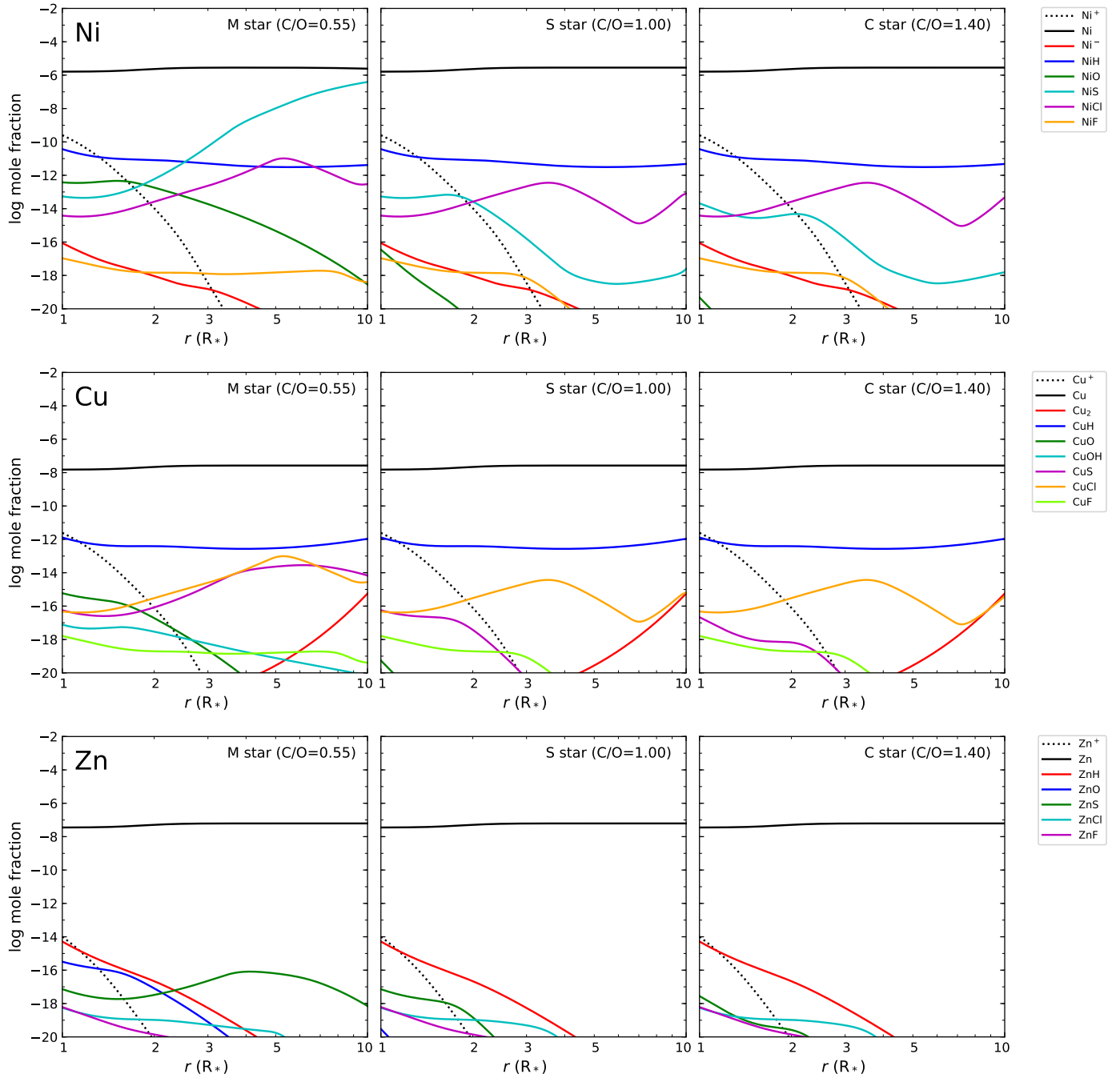


Fig. A.9. Chemical equilibrium abundances of species containing Cr, Mn, Fe, and Co in M-, S-, and C-type AGB atmospheres.



**Fig. A.10.** Chemical equilibrium abundances of species containing Ni, Cu, and Zn in M-, S-, and C-type AGB atmospheres.

dant of these four metals, TiO and TiO<sub>2</sub>, have been observed in the atmospheres of M stars (Kamiński et al. 2017). The oxides ZrO and VO have long been detected in the optical and near-infrared toward M- and S-type AGB stars (Keenan & Schroeder 1952; Keenan 1954; Joyce et al. 1998), and ScO has also recently been detected at optical and near-infrared wavelengths toward the remnant of a stellar merger V1309 Sco (Kamiński et al. 2015). Thus, detecting ZrO, VO, and ScO in M-type atmospheres through their rotational spectrum may be simply a matter of sensitivity. The sulfides TiS and ZrS have been observed through near-infrared observations toward S-type stars (Hinkle et al. 1989; Jonsson et al. 1992; Joyce et al. 1998). Our calculations result in a low mole fraction ( $< 10^{-12}$ ) for TiS in S-type atmospheres, however, while in the case of ZrS, we lack ther-

mochemical data. We note that similarly to the case of titanium-carbon clusters in carbon-rich atmospheres, large metal-oxygen clusters with specific stoichiometries might also be fairly abundant in oxygen-rich atmospheres, as is illustrated by the case of V, where V<sub>4</sub>O<sub>10</sub> is a main reservoir at large radii. Calculations of thermochemical data for such clusters (M<sub>x</sub>O<sub>y</sub>) are expected to allow us to shed light on this.

For Cr, Mn, Fe, Ni, Cu, and Zn, neutral atoms are clearly the main reservoir of the metal throughout the extended atmosphere and for any C/O. For the most abundant of these elements, some molecules can reach non-negligible abundances. In the case of Cr (top panel in Fig. A.9), the molecules CrO, CrS, and CrCl reach mole fractions of about  $10^{-10}$  in oxygen-rich atmospheres. The only Mn-bearing molecule that is predicted with

a non-negligible abundance is MnH, which has a calculated mole fraction of about  $10^{-10}$  in atmospheres of any chemical type (see the second panel from the top in Fig. A.9). For iron (third panel from the top in Fig. A.9), the molecules FeS and FeO are present with mole fractions up to  $\sim 4 \times 10^{-8}$  and  $\sim 3 \times 10^{-10}$  in M-type atmospheres, while Fe(OH)<sub>2</sub> also becomes abundant at large radii. The hydride FeH has been observed at near-infrared wavelengths toward S-type stars, although its abundance has not been constrained (Clegg & Lambert 1978). According to our calculations, the abundance of FeH is insensitive to the C/O and thus is expected with the same abundance in M-, S-, and C-type atmospheres. The maximum predicted abundance, which is reached at the stellar photosphere, is somewhat low (slightly below  $10^{-10}$ ), however. The only Ni-bearing molecule with a non-negligible abundance is NiS, which becomes increasingly abundant with increasing radius in oxygen-rich atmospheres (see the top panel in Fig. A.10). Finally, for Cu and Zn, no molecule is predicted with a significant abundance.

Cobalt (see the bottom panel in Fig. A.9) is the only transition metal for which a hydride such as CoH is found to be the main carrier of the element by far. The Co budget is completely different to that of any other transition metal discussed here. Chemical equilibrium predicts that CoH is more abundant than atomic Co by orders of magnitude, and this applies to atmospheres with any C/O. For the other transition metals discussed here, neutral atoms are the main reservoir of the metal, or at least an important reservoir in the hottest regions of the atmosphere. This implies that CoH is a rather stable species. The thermochemical data for this molecule are taken from Barklem & Collet (2016). The other Co-containing molecules included in the calculations are the halides CoCl, CoCl<sub>2</sub>, CoCl<sub>3</sub>, Co<sub>2</sub>Cl<sub>4</sub>, and CoF<sub>2</sub>, which are all predicted to have negligible abundances compared to CoH. These halides are thus much less stable than CoH. Cobalt clearly has an incompleteness problem in the set of molecules for which thermochemical data are available. It would be desirable to have such data for potentially abundant molecules such as oxides, hydroxides, sulfides, and carbides. If some of them were found to be especially stable, then it might become a main carrier of Co at the expense of CoH.

## Appendix B: Thermochemical data of $\text{Ti}_x\text{C}_y$ clusters

For each cluster  $\text{Ti}_x\text{C}_y$ , we compute a partition function  $Z$  (Kardar 2007) which takes into account electronic ( $e$ ), translational ( $t$ ), rotational ( $r$ ), and vibrational ( $v$ ) contributions (Ochterski 2000),

$$Z(N, V, T) = \sum \exp\left(-\frac{U_e + U_t + U_r + U_v}{kT}\right) = Z_e Z_t Z_r Z_v, \quad (\text{B.1})$$

where  $N$  is the number of particles,  $V$  the volume,  $T$  the absolute temperature (i.e., we work in the microcanonical ensemble), the different terms  $U$  are the internal energy contributions as labelled above, and  $k$  is the Boltzmann constant.

The main thermodynamical magnitudes per unit mol, enthalpy ( $H$ ), entropy ( $S$ ), and heat capacity at constant pressure ( $C_P$ ), are derived as

$$H = \frac{RT^2}{Z} \left. \frac{\partial Z}{\partial V} \right|_V \quad (\text{B.2})$$

$$S = R \ln Z + \frac{RT}{Z} \left. \frac{\partial Z}{\partial V} \right|_V \quad (\text{B.3})$$

$$C_P = T \left. \frac{\partial S}{\partial T} \right|_P \quad (\text{B.4})$$

where  $R$  is the ideal gas constant and  $P$  is the pressure.

Here, we are only interested in values for not too low temperatures,  $T \geq 50$  K. Accordingly, we write:

$$Z_e = m \quad (\text{B.5})$$

$$Z_t = \left(\frac{2\pi M k T}{h^2}\right)^{3/2} \left(\frac{kT}{P}\right) \quad (\text{B.6})$$

$$Z_r = \begin{cases} \frac{1}{\sigma} \frac{T}{\Theta}, & \text{for linear} \\ \sqrt{\frac{\pi}{\sigma^2}} \frac{T^3}{\Theta}, & \text{for non-linear} \end{cases} \quad (\text{B.7})$$

$$Z_v = \prod_i \left[ \frac{\exp\left(-\frac{\hbar w_i}{2kT}\right)}{1 - \exp\left(-\frac{\hbar w_i}{kT}\right)} \right] \quad (\text{B.8})$$

where  $h$  is the Planck constant ( $\hbar = \frac{h}{2\pi}$ ),  $M$  the total mass,  $m$  the spin multiplicity of the electronic state (see Table B.1), and  $w_i$  is the vibrational frequency of the mode  $i$  (the product is taken over all modes  $i$  with positive frequencies). For linear clusters,  $\Theta = \frac{h^2}{8\pi^2 k I}$  ( $I$  is the moment of inertia) and  $\sigma = 1$  or  $2$  depending on whether it is heteronuclear or homonuclear. The only linear molecule is  $\text{TiC}$ , in which case  $\sigma = 1$  since it is heteronuclear. For non-linear clusters (all  $\text{Ti}_x\text{C}_y$  clusters except  $\text{TiC}$ ),  $\Theta = \Theta_x \Theta_y \Theta_z$  ( $x$ ,  $y$ , and  $z$  are the principal axes of the moment of inertia tensor) and  $\sigma$  is the order of the rotational subgroup in the point group associated to the cluster (see Table B.1).

For each cluster, self-consistent many-body wavefunctions  $\Psi$  and their associated ground-state variational total energies  $U_0$  for optimized geometrical configurations have been obtained from *ab initio* Density Functional Theory calculations (Hohenberg & Kohn 1964; Kohn & Sham 1965). The optimized geometries of the clusters are given in Table B.2. For the sake of efficiency and accuracy we apply two different strategies. For small

$\text{Ti}_x\text{C}_y$  clusters, with  $x + y \leq 10$ , we use an all-electron localized basis formed with linear combinations of gaussians (cc-pVTZ; Frisch et al. 2009; Duning 1989) and a chemistry model based on the hybrid exchange and correlation functional B3LYP (Becke 1988). For large  $\text{Ti}_x\text{C}_y$  clusters, with  $x + y > 10$ , the system is big enough to require the use of pseudo-potentials for Ti and we favor the use of an extended basis formed with linear combinations of plane-waves (Giannozzi et al. 2009) and a chemistry model based on a generalized-gradients approximation for exchange and correlation (Perdew et al. 1996), with  $E_c = 490$  eV and  $\Gamma$  point. Both approaches provide a reasonable representation of equilibrium geometries, but their combined use yields more accurate values of the enthalpy of atomization



for all the clusters studied here. In order to work with a minimal set of geometrical parameters, symmetrized models have been preferred whenever it has been possible.

Finally, the electric dipole moment  $\mathbf{p}$  has been obtained from  $\mathbf{p} = \langle \Psi | \mathbf{r} | \Psi \rangle$  (Snyder 1974). Since this is the expectation value of a one-electron operator, its value should not critically depend on the choice for the exchange-correlation functional, although it should be noted that in practice one cannot expect in computed values a precision better than  $\approx 10\%$ , because the contribution of the tails of wave functions require the use of large basis sets with diffuse functions.

The calculated enthalpies of atomization agree well with literature values, either experimental or theoretical, when these are available (see Table B.1). The thermochemical properties of all  $\text{Ti}_x\text{C}_y$  clusters calculated at 1 bar and as a function of temperature are given in Tables B.3-B.25.

**Table B.1.** Properties of  $\text{Ti}_x\text{C}_y$  clusters.

	$\sigma^a$	$G^b$	$m^c$	$\Delta_{\text{at}}H^d$		$\Delta_{\text{at}}H^o(298.15\text{ K})^e$	$\Delta_fH^o(298.15\text{ K})^f$
						kJ mol <sup>-1</sup>	
TiC	1	$C_v$	1	366	372 <sup>g</sup>	363	826.67
TiC <sub>2</sub>	2	$C_{2v}$	3	1146	1157 <sup>h</sup>	1143	763.35
TiC <sub>3</sub>	2	$C_{2v}$	1	1740		1738	885.03
TiC <sub>4</sub>	2	$C_{2v}$	3	2405	2398 <sup>h</sup>	2403	936.70
Ti <sub>2</sub> C	2	$C_{2v}$	3	726		722	940.67
Ti <sub>2</sub> C <sub>2</sub>	4	$D_{2h}$	1	1379		11376	1003.35
Ti <sub>2</sub> C <sub>3</sub>	1	$C_{2v}$	1	2024		2022	1074.02
Ti <sub>2</sub> C <sub>4</sub>	1	$C_s$	1	2708		2704	1108.70
Ti <sub>3</sub> C	1	$C_s$	1	909		902	1233.67
Ti <sub>3</sub> C <sub>2</sub>	2	$C_{2v}$	1	1714		1708	1144.34
Ti <sub>3</sub> C <sub>3</sub>	1	$C_s$	1	2403		2399	1170.02
Ti <sub>3</sub> C <sub>4</sub>	2	$C_{2v}$	1	3070		3068	1217.70
Ti <sub>4</sub> C	1	$C_s$	1	1185		1178	1430.67
Ti <sub>4</sub> C <sub>2</sub>	2	$C_{2v}$	1	1990		1985	1340.34
Ti <sub>4</sub> C <sub>3</sub>	1	$C_s$	1	2741		2737	1305.02
Ti <sub>4</sub> C <sub>4</sub>	12	$T_d$	1	3589		3587	1171.69
Ti <sub>3</sub> C <sub>8</sub>	1	$C_s$	1	6348	6436 <sup>i</sup>	6345	807.40
Ti <sub>4</sub> C <sub>8</sub>	2	$C_{2v}$	1	7077	7063 <sup>i</sup>	7075	550.40
Ti <sub>6</sub> C <sub>13</sub>	1	$C_1$	1	11682	11694 <sup>i</sup>	11682	472.77
Ti <sub>7</sub> C <sub>13</sub>	1	$C_1$	1	11975	12533 <sup>i</sup>	11973	654.77
Ti <sub>8</sub> C <sub>12</sub>	1	$C_1$	1	12723	12698 <sup>i</sup>	12727	-342.91
Ti <sub>9</sub> C <sub>15</sub>	1	$C_1$	1	14961		14958	49.11
Ti <sub>13</sub> C <sub>22</sub>	1	$C_1$	1	22513		22520	-604.17

<sup>a</sup> Order of the rotational subgroup. <sup>b</sup> Symmetry group. <sup>c</sup> Spin multiplicity. <sup>d</sup> Enthalpy of atomization (at 0 K and 0 bar). Ground state reference energies for the atoms are  $-37.8585747$  Ha for C and  $-849.3765897$  Ha for Ti using gaussians (upper block) and  $-5.6859$  Ha for C and  $-59.65385$  Ha for Ti using plane-waves (lower block). <sup>e</sup> Standard enthalpy of atomization (at 298.15 K and 1 bar). <sup>f</sup> Standard enthalpy of formation (at 298.15 K and 1 bar). Calculated from  $\Delta_{\text{at}}H^o(298.15\text{ K})$  adopting standard enthalpies of formation of Ti and C atoms of  $472.9973$  kJ mol<sup>-1</sup> and  $716.6759$  kJ mol<sup>-1</sup>, respectively (Goos, Burcat, & Ruscic). <sup>g</sup> Experimental value from Sevy et al. (2018). <sup>h</sup> Experimental value from Stearns & Kohl (1974). <sup>i</sup> DFT calculation by Muñoz et al. (1999).

**Table B.2.** Equilibrium geometries of  $Ti_xC_y$  clusters.

	$x$ (Å)	$y$ (Å)	$z$ (Å)
TiC			
C	0.000000	0.000000	-1.252485
Ti	0.000000	0.000000	0.341587
TiC <sub>2</sub>			
C	0.000000	0.643420	-1.208026
C	0.000000	-0.643420	-1.208026
Ti	0.000000	0.000000	0.658923
TiC <sub>3</sub>			
C	0.000000	1.221729	-0.707597
C	0.000000	-1.221729	-0.707597
C	0.000000	0.000000	-1.233465
Ti	0.000000	0.000000	0.722361
TiC <sub>4</sub>			
C	0.000000	1.724976	-0.390031
C	0.000000	-1.724976	-0.390031
C	0.000000	-0.686718	-1.131017
C	0.000000	0.686718	-1.131017
Ti	0.000000	0.000000	0.829663
Ti <sub>2</sub> C			
C	0.000000	0.000000	1.229519
Ti	0.000000	1.180152	-0.167662
Ti	0.000000	-1.180152	-0.167662
Ti <sub>2</sub> C <sub>2</sub>			
C	0.000000	+1.281401	0.000000
C	0.000000	-1.281401	0.000000
Ti	0.000000	0.000000	+1.313328
Ti	0.000000	0.000000	-1.313328
Ti <sub>2</sub> C <sub>3</sub>			
C	-0.680075	0.000000	-1.146577
C	0.680075	0.000000	-1.146577
C	0.000000	0.000000	1.371677
Ti	0.000000	1.361154	0.125656
Ti	0.000000	-1.361154	0.125656
Ti <sub>2</sub> C <sub>4</sub>			
C	0.433100	-0.890678	1.962981
C	0.433100	-0.890678	-1.962981
C	0.433100	0.307324	1.539292
C	0.433100	0.307324	-1.539292
Ti	-0.190324	-1.058004	0.000000
Ti <sub>3</sub> C			
C	-1.049036	-0.514780	0.000000
Ti	0.095367	1.229089	0.000000
Ti	0.095367	-0.544347	1.489014
Ti	0.095367	-0.544347	-1.489014
Ti <sub>3</sub> C <sub>2</sub>			
C	1.337492	0.000000	0.190605
C	-1.337492	0.000000	0.190605
Ti	0.000000	1.136286	-0.808495
Ti	0.000000	0.000000	1.513023
Ti	0.000000	-1.136286	-0.808495
Ti <sub>3</sub> C <sub>3</sub>			
C	1.642467	0.576947	0.000000
C	-0.888601	-1.048677	0.000000
C	0.505108	1.274912	0.000000
Ti	0.505108	-0.527135	1.263766
Ti	0.505108	-0.527135	-1.263766
Ti	-1.353573	0.835220	0.000000
Ti <sub>3</sub> C <sub>4</sub>			
C	0.000000	1.380871	-1.073725
C	0.000000	1.320965	0.280292
C	0.000000	-1.320965	0.280292
C	0.000000	-1.380871	-1.073725
Ti	-1.383702	0.000000	-0.628512
Ti	1.383702	0.000000	-0.628512
Ti	0.000000	0.000000	1.689805

**Table B.2.** Continued

	$x$ (Å)	$y$ (Å)	$z$ (Å)
Ti <sub>4</sub> C			
C	1.684138	-0.077493	0.000000
Ti	0.395001	-0.915142	1.180567
Ti	0.395001	-0.915142	-1.180567
Ti	0.395001	1.435395	0.000000
Ti	-1.644313	0.416023	0.000000
Ti <sub>4</sub> C <sub>2</sub>			
6	0.000000	1.395898	-0.818963
6	0.000000	-1.395898	-0.818963
22	-1.310110	0.000000	-0.944194
22	1.310110	0.000000	-0.944194
22	0.000000	-1.126550	1.167548
22	0.000000	1.126550	1.167548
Ti <sub>4</sub> C <sub>3</sub>			
C	-1.109805	1.070447	0.000000
C	0.055800	-0.984249	1.379937
C	0.055800	-0.984249	-1.379937
Ti	-1.292939	-0.916643	0.000000
Ti	1.453577	-0.687631	0.000000
Ti	0.055800	0.924599	1.534723
Ti	0.055800	0.924599	-1.534723
Ti <sub>4</sub> C <sub>4</sub>			
C	0.971811	0.971811	0.971811
C	-0.971811	-0.971811	0.971811
C	0.971811	-0.971811	-0.971811
C	-0.971811	0.971811	-0.971811
Ti	-0.979854	-0.979854	-0.979854
Ti	0.979854	-0.979854	0.979854
Ti	-0.979854	0.979854	0.979854
Ti	0.979854	0.979854	-0.979854
Ti <sub>3</sub> C <sub>8</sub>			
C	-0.000330	-0.000405	-0.811826
C	-0.496859	2.961680	-0.000222
Ti	0.843006	-1.546210	0.000001
Ti	-1.760751	0.042519	0.000159
Ti	0.917099	1.502814	-0.000101
C	-0.000199	-0.000350	0.811948
C	2.674793	0.218626	-0.000419
C	-2.316426	-1.911570	0.000118
C	-1.525237	2.206854	-0.000029
C	-1.148762	-2.424656	0.000069
C	2.813356	-1.049053	-0.000398
Ti <sub>4</sub> C <sub>8</sub>			
C	0.752641	-1.956386	-0.001655
Ti	-1.217718	-1.441533	-0.000276
C	2.016170	1.691519	0.003061
Ti	1.204968	0.009068	-1.163398
Ti	1.204958	0.005541	1.163430
C	-0.686096	-0.006059	1.643238
C	0.720086	1.966051	0.001699
Ti	-1.243660	1.426431	0.000247
C	-0.685962	-0.003842	-1.643241
C	-1.979030	-0.012806	1.317373
C	-1.978981	-0.012437	-1.317427
C	2.044562	-1.664058	-0.003051

Table B.2. Continued

	$x$ (Å)	$y$ (Å)	$z$ (Å)
Ti <sub>6</sub> C <sub>13</sub>			
Ti	-2.065543	-1.427553	-1.139204
Ti	0.233151	0.044000	-1.635614
C	-1.079408	1.644746	-1.163851
C	1.148345	-1.740708	-0.954883
C	-1.834590	0.550348	-1.402548
C	-0.145894	-2.025830	-1.219164
C	-1.808092	2.420988	2.030903
C	3.133953	-1.369837	1.701950
C	1.970242	1.174304	-1.488979
C	-2.251422	-1.414429	0.849118
C	0.432695	0.337527	0.596146
C	-0.782991	2.844192	1.409118
Ti	2.354521	-0.422576	0.090879
Ti	-1.563569	0.781951	0.832819
Ti	0.029000	-1.593864	0.952159
Ti	0.559053	2.271346	-0.099558
C	1.959424	-1.855597	1.774769
C	2.664581	1.785284	-0.601139
C	-1.759559	-1.092692	2.000598
Ti <sub>7</sub> C <sub>13</sub>			
Ti	-0.464988	2.563063	-0.978601
Ti	-2.014016	0.783756	-1.151130
C	0.284008	2.008628	0.786075
C	-0.047150	0.643683	-1.734093
Ti	1.725495	1.468196	-0.460973
C	-1.124677	1.643146	0.784335
C	1.139599	-0.168092	-1.756440
C	-2.673948	-1.088343	-0.713594
C	-1.545656	0.963542	1.922755
C	2.880019	0.257918	0.936496
C	1.434143	-1.439387	-2.252467
Ti	-0.449532	-1.572886	-1.056378
Ti	0.672986	0.261419	1.878044
C	-2.424589	-2.290367	-0.285906
Ti	-1.677773	-1.303445	1.364457
C	-1.459066	0.099908	2.884558
Ti	1.942788	-1.315217	-0.088346
C	2.736683	0.272091	2.217901
C	1.507097	-2.668603	-1.839279
C	0.200498	-1.434989	0.863725
Ti <sub>8</sub> C <sub>12</sub>			
C	-0.010224	-0.658245	-2.573184
C	-0.003833	0.684662	-2.566554
Ti	-0.017130	-2.419320	-1.723205
Ti	0.007582	2.436993	-1.698905
Ti	1.443003	-0.002206	-1.020257
Ti	-1.448452	0.012455	-1.012105
C	1.473589	-2.162833	-0.484184
C	1.495822	2.152339	-0.463166
C	-1.498448	-2.147583	-0.476339
C	-1.476163	2.167683	-0.454397
C	2.151382	-1.497996	0.465359
C	2.166341	1.471515	0.480152
C	-2.163776	-1.476377	0.477575
C	-2.148555	1.493111	0.492101
Ti	-0.004706	-1.451640	1.021043
Ti	0.010415	1.441388	1.035470
Ti	2.431811	-0.020936	1.715594
Ti	-2.422232	0.003655	1.729195
C	0.678868	-0.016554	2.582253
C	-0.664475	-0.009332	2.585976

Table B.2. Continued

	$x$ (Å)	$y$ (Å)	$z$ (Å)
Ti <sub>9</sub> C <sub>15</sub>			
Ti	0.000543	0.000289	-1.225500
Ti	-2.586230	1.811839	-1.014003
C	-2.397501	-0.077244	-1.045225
C	-0.580749	-2.224080	-1.445109
C	-0.730783	2.211305	-1.375106
C	0.731832	-2.210641	-1.376045
C	0.581726	2.224440	-1.443769
C	2.398612	0.077870	-1.043989
Ti	-2.445902	-1.980120	-1.043796
Ti	2.587090	-1.811233	-1.014182
Ti	2.446752	1.980753	-1.041296
C	-2.287412	-2.299596	0.926994
C	-2.443943	2.198580	0.958404
C	2.443349	-2.199080	0.957800
C	2.286979	2.299213	0.929686
Ti	0.024346	-2.028221	0.859059
Ti	-0.025096	2.027885	0.859993
Ti	-1.965407	-0.009575	1.107698
Ti	1.965115	0.009061	1.108527
C	-0.000077	-0.000149	0.823805
C	-1.873925	-1.892626	2.087552
C	-1.745372	2.113455	2.045197
C	1.744580	-2.114153	2.044474
C	1.872955	1.891398	2.089623
Ti <sub>13</sub> C <sub>22</sub>			
C	3.213061	-2.692279	0.525858
C	3.037349	0.549848	2.832567
C	3.196959	-0.423904	-2.732313
C	3.157639	2.822189	-0.342014
Ti	2.086362	-1.028134	1.731843
Ti	2.126215	1.080298	-1.675545
Ti	2.136512	-1.670010	-1.029389
Ti	2.044443	1.734115	1.112675
C	2.115887	0.037224	0.034824
C	2.058985	-3.147072	0.835421
C	1.850802	0.821407	3.226136
C	2.068047	-0.835435	-3.167910
C	2.037909	3.194126	-0.828415
Ti	-0.028766	0.007252	-0.008213
Ti	0.020922	-0.736335	-2.810079
C	-0.020522	-1.139065	1.874161
C	0.000774	-1.923342	-1.144800
C	-0.062185	1.947498	1.119323
C	0.008376	1.130385	-1.945792
Ti	0.014174	-2.817765	0.694098
Ti	-0.173672	0.676607	2.812652
Ti	-0.006235	2.811426	-0.768197
C	-2.023761	-3.198831	0.792462
C	-2.117078	0.066831	3.653211
C	-2.014377	-0.832355	-3.187119
C	-2.024816	3.207680	-0.939022
Ti	-2.102304	-1.061286	1.747713
Ti	-2.146819	1.018652	-1.760114
Ti	-2.153323	-1.717624	-1.024059
Ti	-2.149929	1.802367	0.937736
C	-2.179120	0.012986	-0.017381
C	-3.194569	-2.705365	0.659437
C	-2.436889	0.964097	2.788236
C	-3.190999	-0.692201	-2.705061
C	-3.198611	2.719855	-0.798541

**Table B.3.** Thermochemical properties of TiC at 1 bar.

$T$ (K)	$C_p^o$	$S^o$	$-[G^o - H^o(298.15\text{ K})]/T$	$H^o - H^o(298.15\text{ K})$	$\Delta_f H^o$	$\Delta_f G^o$	$\log K_f$
	$\text{J K}^{-1} \text{ mol}^{-1}$			$\text{kJ mol}^{-1}$			
100	29.102	183.974	242.724	-5.875	826.055	808.579	-Infinity
200	29.461	204.216	218.981	-2.953	826.734	790.753	-206.519
298.15	30.776	216.211	216.211	0.000	826.670	773.089	-135.439
300	30.805	216.401	216.211	0.057	826.664	772.756	-134.546
400	32.334	225.483	217.438	3.218	826.189	754.850	-98.571
500	33.561	232.842	219.806	6.518	825.422	737.099	-77.003
600	34.455	239.048	222.510	9.923	824.424	719.525	-62.639
700	35.096	244.414	225.264	13.405	823.245	702.133	-52.393
800	35.562	249.136	227.960	16.941	821.935	684.918	-44.720
900	35.906	253.348	230.550	20.518	820.486	667.877	-38.762
1000	36.166	257.148	233.024	24.124	818.848	651.005	-34.004
1100	36.366	260.607	235.376	27.754	816.969	634.311	-30.120
1200	36.522	263.780	237.612	31.401	810.870	617.916	-26.897
1300	36.647	266.710	239.739	35.062	809.252	601.902	-24.184
1400	36.747	269.432	241.765	38.734	807.525	586.016	-21.864
1500	36.830	271.972	243.695	42.416	805.683	570.258	-19.858
1600	36.898	274.352	245.536	46.105	803.712	554.627	-18.106
1700	36.955	276.593	247.299	49.800	801.602	539.120	-16.565
1800	37.003	278.708	248.986	53.500	799.342	523.748	-15.198
1900	37.044	280.711	250.603	57.205	796.920	508.500	-13.979
2000	37.080	282.613	252.156	60.914	779.638	493.842	-12.898
2200	37.137	286.152	255.088	68.341	772.561	465.604	-11.055
2400	37.180	289.388	257.814	75.778	765.428	438.013	-9.533
2600	37.215	292.367	260.359	83.222	758.239	411.019	-8.257
2800	37.242	295.128	262.745	90.673	751.001	384.582	-7.174
3000	37.264	297.700	264.990	98.129	743.713	358.663	-6.245
3200	37.282	300.107	267.111	105.588	736.377	333.231	-5.439
3400	37.297	302.369	269.119	113.051	728.995	308.262	-4.736
3600	37.310	304.503	271.026	120.517	721.569	283.726	-4.117
3800	37.321	306.522	272.842	127.985	306.233	278.645	-3.830
4000	37.330	308.438	274.574	135.455	301.023	277.327	-3.621
4500	37.348	312.838	278.585	154.137	286.916	275.194	-3.194
5000	37.360	316.777	282.212	172.827	271.454	274.709	-2.870
6000	37.377	323.594	288.557	210.221	237.457	278.503	-2.425

**Table B.4.** Thermochemical properties of  $\text{TiC}_2$  at 1 bar.

$T$ (K)	$C_p^\circ$	$S^\circ$	$-[G^\circ - H^\circ(298.15 \text{ K})]/T$	$H^\circ - H^\circ(298.15 \text{ K})$	$\Delta_f H^\circ$	$\Delta_f G^\circ$	$\log K_f$
	$\text{J K}^{-1} \text{ mol}^{-1}$			$\text{kJ mol}^{-1}$			
100	33.417	221.573	294.093	-7.252	762.349	741.208	–Infinity
200	36.434	245.483	264.408	-3.785	763.247	719.629	-187.944
298.15	40.569	260.825	260.825	0.000	763.350	698.179	-122.316
300	40.641	261.076	260.826	0.075	763.346	697.774	-121.491
400	44.102	273.270	262.465	4.322	762.934	675.966	-88.270
500	46.818	283.422	265.668	8.877	762.096	654.314	-68.354
600	48.948	292.160	269.372	13.673	760.911	632.864	-55.095
700	50.614	299.841	273.188	18.657	759.461	611.634	-45.640
800	51.917	306.692	276.954	23.790	757.827	590.626	-38.563
900	52.940	312.873	280.609	29.038	756.014	569.831	-33.071
1000	53.750	318.498	284.120	34.378	753.987	549.251	-28.689
1100	54.397	323.656	287.483	39.790	751.696	528.887	-25.114
1200	54.920	328.415	290.697	45.261	745.170	508.861	-22.150
1300	55.347	332.832	293.772	50.778	743.109	489.250	-19.658
1400	55.698	336.949	296.710	56.335	740.927	469.806	-17.528
1500	55.991	340.805	299.523	61.923	738.617	450.519	-15.688
1600	56.236	344.429	302.217	67.539	736.168	431.392	-14.083
1700	56.444	347.847	304.802	73.177	733.569	412.420	-12.672
1800	56.621	351.081	307.284	78.834	730.809	393.611	-11.422
1900	56.773	354.148	309.670	84.508	727.877	374.956	-10.308
2000	56.905	357.066	311.968	90.196	710.075	356.915	-9.321
2200	57.119	362.503	316.318	101.607	701.926	321.993	-7.645
2400	57.285	367.484	320.378	113.055	693.681	287.815	-6.264
2600	57.416	372.078	324.180	124.534	685.342	254.330	-5.109
2800	57.521	376.340	327.756	136.036	676.913	221.493	-4.132
3000	57.607	380.314	331.129	147.556	668.393	189.260	-3.295
3200	57.677	384.037	334.320	159.093	659.787	157.595	-2.572
3400	57.736	387.537	337.348	170.642	651.094	126.477	-1.943
3600	57.785	390.841	340.229	182.202	642.317	95.869	-1.391
3800	57.827	393.969	342.977	193.771	225.590	84.792	-1.166
4000	57.863	396.938	345.601	205.348	218.950	77.554	-1.013
4500	57.933	403.762	351.692	234.317	201.091	60.925	-0.707
5000	57.984	409.873	357.210	263.317	181.627	46.387	-0.485
6000	58.050	420.458	366.896	321.375	138.872	23.282	-0.203

**Table B.5.** Thermochemical properties of  $\text{TiC}_3$  at 1 bar.

$T$ (K)	$C_p^\circ$	$S^\circ$	$-[G^\circ - H^\circ(298.15 \text{ K})]/T$	$H^\circ - H^\circ(298.15 \text{ K})$	$\Delta_f H^\circ$	$\Delta_f G^\circ$	$\log K_f$
	$\text{J K}^{-1} \text{ mol}^{-1}$			$\text{kJ mol}^{-1}$			
100	33.997	221.112	303.592	-8.248	884.024	863.024	-Infinity
200	41.497	246.665	269.255	-4.518	884.859	841.621	-219.804
298.15	50.307	264.929	264.929	0.000	885.030	820.346	-143.718
300	50.459	265.241	264.931	0.093	885.028	819.944	-142.762
400	57.716	280.805	267.002	5.521	884.774	798.277	-104.242
500	63.254	294.317	271.143	11.587	884.121	776.722	-81.142
600	67.408	306.243	276.020	18.134	883.109	755.332	-65.756
700	70.517	316.886	281.112	25.042	881.810	734.136	-54.781
800	72.859	326.469	286.193	32.221	880.301	713.139	-46.562
900	74.645	335.164	291.157	39.606	878.590	692.344	-40.182
1000	76.027	343.109	295.962	47.147	876.641	671.751	-35.088
1100	77.111	350.412	300.584	54.811	874.408	651.370	-30.930
1200	77.973	357.165	305.022	62.572	867.921	631.319	-27.480
1300	78.669	363.439	309.277	70.411	865.883	611.685	-24.577
1400	79.236	369.294	313.357	78.312	863.705	592.213	-22.095
1500	79.705	374.781	317.271	86.265	861.386	572.901	-19.950
1600	80.096	379.941	321.028	94.261	858.912	553.749	-18.078
1700	80.425	384.810	324.638	102.293	856.275	534.754	-16.431
1800	80.704	389.418	328.110	110.355	853.463	515.927	-14.972
1900	80.943	393.791	331.453	118.443	850.466	497.252	-13.670
2000	81.149	397.951	334.675	126.553	832.587	479.199	-12.515
2200	81.484	405.707	340.785	142.829	824.247	444.261	-10.548
2400	81.741	412.813	346.495	159.163	815.765	410.088	-8.925
2600	81.944	419.369	351.852	175.544	807.143	376.630	-7.566
2800	82.106	425.452	356.895	191.960	798.386	343.845	-6.414
3000	82.237	431.125	361.656	208.406	789.496	311.689	-5.427
3200	82.345	436.440	366.166	224.876	780.475	280.123	-4.572
3400	82.435	441.438	370.448	241.365	771.325	249.133	-3.827
3600	82.511	446.155	374.524	257.871	762.049	218.683	-3.173
3800	82.575	450.621	378.413	274.391	344.781	207.795	-2.856
4000	82.630	454.861	382.130	290.922	337.558	200.770	-2.622
4500	82.737	464.606	390.763	332.293	318.062	184.812	-2.145
5000	82.814	473.334	398.592	373.710	296.703	171.143	-1.788
6000	82.915	488.452	412.346	456.634	249.392	150.386	-1.309

**Table B.6.** Thermochemical properties of  $\text{TiC}_4$  at 1 bar.

$T$ (K)	$C_p^\circ$	$S^\circ$	$-[G^\circ - H^\circ(298.15 \text{ K})]/T$	$H^\circ - H^\circ(298.15 \text{ K})$	$\Delta_f H^\circ$	$\Delta_f G^\circ$	$\log K_f$
	$\text{J K}^{-1} \text{ mol}^{-1}$			$\text{kJ mol}^{-1}$			
100	38.860	239.783	349.093	-10.931	934.002	911.231	-Infinity
200	56.171	272.079	302.934	-6.171	935.541	887.836	-231.874
298.15	68.560	297.017	297.017	0.000	936.700	864.161	-151.394
300	68.745	297.442	297.019	0.127	936.716	863.709	-150.382
400	77.014	318.437	299.825	7.445	937.329	839.264	-109.595
500	83.017	336.311	305.379	15.466	937.305	814.741	-85.114
600	87.623	351.882	311.860	24.013	936.715	790.275	-68.798
700	91.219	365.679	318.580	32.969	935.691	765.946	-57.154
800	94.047	378.060	325.255	42.244	934.357	741.783	-48.433
900	96.284	389.279	331.756	51.771	932.753	717.802	-41.659
1000	98.066	399.526	338.028	61.498	930.867	694.017	-36.251
1100	99.499	408.949	344.053	71.386	928.664	670.438	-31.836
1200	100.661	417.664	349.829	81.402	922.181	647.188	-28.171
1300	101.614	425.765	355.362	91.524	920.127	624.355	-25.086
1400	102.402	433.330	360.664	101.733	917.917	601.686	-22.449
1500	103.059	440.423	365.747	112.014	915.552	579.182	-20.168
1600	103.612	447.097	370.625	122.355	913.018	556.837	-18.179
1700	104.081	453.397	375.310	132.748	910.310	534.656	-16.428
1800	104.482	459.362	379.816	143.183	907.414	512.647	-14.876
1900	104.827	465.024	384.152	153.656	904.323	490.796	-13.493
2000	105.125	470.412	388.332	164.161	886.340	469.572	-12.264
2200	105.613	480.463	396.258	185.251	877.758	428.305	-10.169
2400	105.992	489.675	403.664	206.427	868.995	387.829	-8.441
2600	106.290	498.177	410.611	227.671	860.051	348.093	-6.993
2800	106.530	506.068	417.151	248.968	850.933	309.060	-5.765
3000	106.725	513.430	423.327	270.308	841.641	270.678	-4.713
3200	106.886	520.328	429.177	291.684	832.178	232.914	-3.802
3400	107.021	526.816	434.731	313.090	822.548	195.758	-3.007
3600	107.134	532.941	440.019	334.520	812.751	159.167	-2.309
3800	107.230	538.739	445.063	355.970	394.921	142.175	-1.954
4000	107.312	544.245	449.885	377.439	387.099	129.075	-1.686
4500	107.473	556.903	461.087	431.174	365.928	98.056	-1.138
5000	107.589	568.241	471.246	484.976	342.642	69.532	-0.726
6000	107.740	587.884	489.097	592.720	290.729	19.679	-0.171

**Table B.7.** Thermochemical properties of Ti<sub>2</sub>C at 1 bar.

$T$ (K)	$C_p^\circ$	$S^\circ$	$-[G^\circ - H^\circ(298.15\text{ K})]/T$	$H^\circ - H^\circ(298.15\text{ K})$	$\Delta_f H^\circ$	$\Delta_f G^\circ$	$\log K_f$
	J K <sup>-1</sup> mol <sup>-1</sup>			kJ mol <sup>-1</sup>			
100	36.104	237.616	323.426	-8.581	941.618	919.604	-Infinity
200	43.796	265.145	287.965	-4.564	941.475	897.553	-234.412
298.15	48.753	283.647	283.647	0.000	940.670	876.154	-153.495
300	48.825	283.949	283.649	0.090	940.650	875.752	-152.479
400	51.876	298.459	285.604	5.142	939.453	854.293	-111.557
500	53.740	310.260	289.394	10.433	937.936	833.171	-87.039
600	54.922	320.176	293.719	15.874	936.149	812.383	-70.723
700	55.704	328.711	298.122	21.412	934.138	791.912	-59.092
800	56.243	336.192	302.425	27.014	931.969	771.739	-50.388
900	56.628	342.844	306.552	32.663	929.601	751.850	-43.635
1000	56.911	348.830	310.486	38.344	926.917	732.240	-38.248
1100	57.126	354.268	314.223	44.050	923.799	712.920	-33.853
1200	57.291	359.249	317.770	49.775	912.283	694.141	-30.215
1300	57.421	363.844	321.140	55.515	909.764	676.063	-27.164
1400	57.526	368.106	324.344	61.267	907.058	658.188	-24.557
1500	57.611	372.080	327.395	67.027	904.144	640.513	-22.304
1600	57.681	375.803	330.305	72.796	900.998	623.038	-20.340
1700	57.739	379.304	333.086	78.571	897.595	605.766	-18.613
1800	57.788	382.608	335.746	84.351	893.912	588.709	-17.084
1900	57.830	385.736	338.296	90.136	889.922	571.856	-15.721
2000	57.866	388.705	340.743	95.925	886.228	556.136	-14.524
2200	57.923	394.227	345.358	107.512	843.863	526.722	-12.506
2400	57.967	399.272	349.643	119.109	831.443	498.443	-10.848
2600	58.002	403.916	353.642	130.713	818.966	471.198	-9.466
2800	58.029	408.219	357.389	142.324	806.441	444.913	-8.300
3000	58.051	412.226	360.913	153.940	793.865	419.528	-7.304
3200	58.069	415.975	364.238	165.560	781.243	394.987	-6.447
3400	58.084	419.499	367.386	177.183	768.573	371.232	-5.703
3600	58.097	422.821	370.374	188.809	755.860	348.228	-5.053
3800	58.107	425.965	373.218	200.437	-72.628	364.007	-5.004
4000	58.117	428.947	375.930	212.067	-80.821	387.203	-5.056
4500	58.134	435.798	382.209	241.150	-103.277	447.014	-5.189
5000	58.147	441.928	387.880	270.240	-128.179	509.476	-5.322
6000	58.164	452.538	397.799	328.434	-183.345	642.099	-5.590

**Table B.8.** Thermochemical properties of  $\text{Ti}_2\text{C}_2$  at 1 bar.

$T$ (K)	$C_p^\circ$	$S^\circ$	$-[G^\circ - H^\circ(298.15 \text{ K})]/T$	$H^\circ - H^\circ(298.15 \text{ K})$	$\Delta_f H^\circ$	$\Delta_f G^\circ$	$\log K_f$
	$\text{J K}^{-1} \text{ mol}^{-1}$			$\text{kJ mol}^{-1}$			
100	38.772	230.105	329.375	-9.927	1003.943	982.775	-Infinity
200	50.435	260.531	287.881	-5.470	1003.914	961.531	-251.121
298.15	60.453	282.649	282.649	0.000	1003.350	940.843	-164.828
300	60.611	283.024	282.651	0.112	1003.336	940.454	-163.744
400	67.562	301.497	285.122	6.550	1002.502	919.612	-120.087
500	72.016	317.099	289.999	13.550	1001.368	899.014	-93.918
600	74.905	330.512	295.660	20.911	999.923	878.675	-76.494
700	76.842	342.221	301.492	28.510	998.200	858.601	-64.068
800	78.188	352.582	307.245	36.270	996.268	838.786	-54.766
900	79.154	361.856	312.806	44.145	994.091	819.228	-47.546
1000	79.868	370.240	318.137	52.103	991.561	799.931	-41.783
1100	80.409	377.884	323.226	60.124	988.564	780.910	-37.082
1200	80.828	384.904	328.077	68.192	977.140	762.419	-33.187
1300	81.159	391.391	332.701	76.297	974.687	744.625	-29.919
1400	81.424	397.420	337.111	84.432	972.024	727.027	-27.125
1500	81.640	403.049	341.322	92.591	969.135	709.628	-24.711
1600	81.818	408.327	345.346	100.770	965.994	692.428	-22.605
1700	81.966	413.295	349.198	108.965	962.579	675.430	-20.753
1800	82.091	417.987	352.891	117.173	958.867	658.650	-19.113
1900	82.197	422.432	356.436	125.393	954.833	642.074	-17.651
2000	82.288	426.653	359.841	133.623	921.081	626.635	-16.366
2200	82.435	434.508	366.278	150.107	908.557	597.794	-14.193
2400	82.547	441.691	372.267	166.617	895.927	570.101	-12.408
2600	82.635	448.306	377.865	183.146	883.190	543.464	-10.918
2800	82.704	454.437	383.118	199.692	870.358	517.813	-9.660
3000	82.761	460.149	388.066	216.249	857.427	493.080	-8.585
3200	82.807	465.495	392.740	232.817	844.405	469.215	-7.659
3400	82.845	470.520	397.169	249.394	831.292	446.167	-6.854
3600	82.878	475.259	401.377	265.977	818.091	423.895	-6.150
3800	82.905	479.744	405.384	282.567	-10.927	440.437	-6.054
4000	82.928	484.000	409.210	299.161	-19.693	464.419	-6.065
4500	82.973	493.777	418.074	340.665	-43.767	526.333	-6.109
5000	83.006	502.526	426.088	382.188	-70.548	591.102	-6.175
6000	83.048	517.674	440.129	465.272	-130.246	728.930	-6.346

**Table B.9.** Thermochemical properties of  $\text{Ti}_2\text{C}_3$  at 1 bar.

$T$ (K)	$C_p^\circ$	$S^\circ$	$-[G^\circ - H^\circ(298.15 \text{ K})]/T$ $\text{J K}^{-1} \text{ mol}^{-1}$	$H^\circ - H^\circ(298.15 \text{ K})$ $\text{kJ mol}^{-1}$	$\Delta_f H^\circ$	$\Delta_f G^\circ$	$\log K_f$
100	37.417	239.168	350.888	-11.172	1074.359	1052.380	-Infinity
200	57.293	271.006	303.316	-6.462	1074.257	1030.396	-269.107
298.15	73.197	297.084	297.084	0.000	1074.020	1008.920	-176.755
300	73.436	297.538	297.085	0.136	1074.014	1008.515	-175.595
400	83.703	320.197	300.105	8.037	1073.620	986.735	-128.852
500	90.285	339.647	306.115	16.766	1072.889	965.093	-100.821
600	94.655	356.532	313.144	26.033	1071.772	943.632	-82.149
700	97.659	371.372	320.423	35.664	1070.308	922.387	-68.828
800	99.793	384.569	327.633	45.549	1068.580	901.370	-58.852
900	101.352	396.425	334.628	55.617	1066.561	880.585	-51.107
1000	102.520	407.174	341.354	65.820	1064.153	860.046	-44.923
1100	103.415	416.995	347.790	76.126	1061.247	839.774	-39.877
1200	104.115	426.031	353.939	86.510	1049.888	820.022	-35.694
1300	104.671	434.393	359.810	96.958	1047.479	800.964	-32.182
1400	105.119	442.172	365.418	107.455	1044.838	782.100	-29.180
1500	105.486	449.442	370.780	117.993	1041.954	763.434	-26.585
1600	105.789	456.265	375.912	128.564	1038.800	744.965	-24.320
1700	106.043	462.690	380.829	139.163	1035.357	726.702	-22.328
1800	106.258	468.762	385.548	149.786	1031.603	708.660	-20.564
1900	106.440	474.516	390.080	160.428	1027.512	690.822	-18.992
2000	106.597	479.983	394.440	171.087	993.690	674.126	-17.606
2200	106.851	490.162	402.686	192.447	980.986	642.780	-15.261
2400	107.045	499.474	410.369	213.852	968.128	612.602	-13.333
2600	107.197	508.054	417.557	235.291	955.116	583.501	-11.722
2800	107.318	516.009	424.310	256.757	941.962	555.408	-10.361
3000	107.416	523.421	430.673	278.245	928.666	528.262	-9.198
3200	107.497	530.361	436.689	299.751	915.234	502.002	-8.194
3400	107.564	536.884	442.392	321.272	901.668	476.593	-7.322
3600	107.620	543.038	447.814	342.805	887.972	451.983	-6.558
3800	107.668	548.862	452.981	364.348	874.116	428.126	-5.885
4000	107.708	554.390	457.915	385.900	859.600	404.126	-5.307
4500	107.788	567.089	469.353	439.811	807.364	544.275	-6.318
5000	107.845	578.456	479.705	493.756	-5.307	603.678	-6.306
6000	107.919	598.139	497.853	601.713	-69.554	731.380	-6.367

**Table B.10.** Thermochemical properties of  $\text{Ti}_2\text{C}_4$  at 1 bar.

$T$ (K)	$C_p^\circ$	$S^\circ$	$-[G^\circ - H^\circ(298.15 \text{ K})]/T$	$H^\circ - H^\circ(298.15 \text{ K})$	$\Delta_f H^\circ$	$\Delta_f G^\circ$	$\log K_f$
	J K <sup>-1</sup> mol <sup>-1</sup>			kJ mol <sup>-1</sup>			
100	52.387	258.183	412.063	-15.388	1105.814	1082.029	-Infinity
200	79.831	303.534	346.959	-8.685	1107.379	1057.629	-276.219
298.15	95.395	338.659	338.659	0.000	1108.700	1032.916	-180.959
300	95.606	339.250	338.660	0.177	1108.719	1032.445	-179.761
400	104.414	368.084	342.531	10.221	1109.445	1006.891	-131.484
500	110.223	392.060	350.108	20.976	1109.414	981.242	-102.508
600	114.497	412.566	358.849	32.230	1108.706	955.665	-83.196
700	117.779	430.484	367.830	43.858	1107.466	930.251	-69.415
800	120.344	446.397	376.676	55.777	1105.851	905.039	-59.092
900	122.367	460.702	385.230	67.925	1103.877	880.051	-51.076
1000	123.977	473.690	393.437	80.253	1101.471	855.305	-44.676
1100	125.271	485.577	401.281	92.726	1098.538	830.828	-39.452
1200	126.321	496.531	408.768	105.316	1087.134	806.875	-35.122
1300	127.181	506.684	415.914	118.001	1084.663	783.619	-31.486
1400	127.893	516.142	422.739	130.764	1081.948	760.564	-28.376
1500	128.486	524.992	429.263	143.593	1078.981	737.713	-25.689
1600	128.986	533.307	435.510	156.476	1075.734	715.064	-23.344
1700	129.410	541.145	441.495	169.405	1072.189	692.625	-21.281
1800	129.772	548.557	447.239	182.373	1068.323	670.417	-19.455
1900	130.084	555.587	452.758	195.375	1064.113	648.418	-17.826
2000	130.353	562.271	458.068	208.406	1030.164	627.566	-16.390
2200	130.795	574.725	468.116	234.540	1017.178	587.929	-13.959
2400	131.136	586.128	477.481	260.752	1004.004	549.487	-11.959
2600	131.406	596.643	486.249	287.025	990.641	512.150	-10.289
2800	131.623	606.396	494.487	313.346	977.100	475.855	-8.877
3000	131.800	615.489	502.254	339.706	963.380	440.531	-7.670
3200	131.945	624.006	509.600	366.099	949.487	406.121	-6.629
3400	132.066	632.014	516.568	392.518	935.422	372.593	-5.724
3600	132.169	639.570	523.193	418.959	921.189	339.897	-4.932
3800	132.255	646.724	529.508	445.420	91.058	346.076	-4.757
4000	132.330	653.514	535.540	471.896	81.100	359.756	-4.698
4500	132.475	669.119	549.531	538.144	53.692	396.183	-4.599
5000	132.580	683.092	562.201	604.453	23.073	435.863	-4.553
6000	132.717	707.294	584.428	737.196	-45.810	524.742	-4.568

**Table B.11.** Thermochemical properties of Ti<sub>3</sub>C at 1 bar.

$T$ (K)	$C_p^o$	$S^o$	$-[G^o - H^o(298.15\text{ K})]/T$ J K <sup>-1</sup> mol <sup>-1</sup>	$H^o - H^o(298.15\text{ K})$ kJ mol <sup>-1</sup>	$\Delta_f H^o$	$\Delta_f G^o$	$\log K_f$
100	49.719	260.044	383.204	-12.316	1235.152	1211.721	-Infinity
200	63.126	299.107	332.122	-6.603	1234.788	1188.319	-310.351
298.15	70.650	325.870	325.870	0.000	1233.670	1165.736	-204.228
300	70.756	326.308	325.871	0.131	1233.644	1165.313	-202.895
400	75.066	347.325	328.707	7.447	1232.098	1142.761	-149.226
500	77.566	364.380	334.190	15.095	1230.197	1120.639	-117.070
600	79.098	378.677	340.445	22.939	1227.988	1098.931	-95.669
700	80.090	390.958	346.805	30.907	1225.519	1077.614	-80.411
800	80.763	401.707	353.011	38.957	1222.873	1056.662	-68.992
900	81.240	411.255	358.962	47.064	1219.972	1036.056	-60.130
1000	81.588	419.839	364.628	55.211	1216.633	1015.795	-53.059
1100	81.849	427.633	370.007	63.389	1212.672	995.898	-47.290
1200	82.050	434.768	375.110	71.590	1196.137	976.747	-42.516
1300	82.209	441.347	379.955	79.809	1193.117	958.585	-38.516
1400	82.335	447.448	384.561	88.042	1189.833	940.668	-35.096
1500	82.438	453.136	388.945	96.286	1186.253	922.994	-32.141
1600	82.522	458.463	393.125	104.540	1182.337	905.567	-29.563
1700	82.592	463.471	397.117	112.801	1178.047	888.396	-27.297
1800	82.651	468.197	400.936	121.069	1173.349	871.498	-25.290
1900	82.701	472.670	404.595	129.342	1168.199	854.861	-23.501
2000	82.744	476.916	408.106	137.620	1162.502	839.876	-21.935
2200	82.813	484.811	414.726	154.187	1101.669	812.824	-19.299
2400	82.865	492.024	420.871	170.766	1084.784	787.316	-17.135
2600	82.907	498.662	426.603	187.354	1067.843	763.214	-15.333
2800	82.939	504.812	431.973	203.950	1050.856	740.414	-13.812
3000	82.966	510.539	437.022	220.552	1033.818	718.833	-12.516
3200	82.987	515.898	441.786	237.158	1016.735	698.393	-11.400
3400	83.005	520.933	446.295	253.769	999.605	679.022	-10.432
3600	83.020	525.681	450.575	270.382	982.432	660.660	-9.586
3800	83.033	530.173	454.647	286.999	-258.379	700.372	-9.627
4000	83.044	534.435	458.531	303.617	-268.727	751.101	-9.808
4500	83.065	544.224	467.519	345.173	-297.460	880.248	-10.217
5000	83.080	552.982	475.635	386.737	-329.728	1012.812	-10.581
6000	83.100	568.141	489.827	469.883	-401.911	1287.977	-11.213

**Table B.12.** Thermochemical properties of  $\text{Ti}_3\text{C}_2$  at 1 bar.

$T$ (K)	$C_p^\circ$	$S^\circ$	$-[G^\circ - H^\circ(298.15 \text{ K})]/T$	$H^\circ - H^\circ(298.15 \text{ K})$	$\Delta_f H^\circ$	$\Delta_f G^\circ$	$\log K_f$
	J K <sup>-1</sup> mol <sup>-1</sup>			kJ mol <sup>-1</sup>			
100	47.514	255.633	389.673	-13.404	1145.725	1122.830	-Infinity
200	69.004	295.408	333.113	-7.541	1145.185	1100.072	-287.304
298.15	83.328	325.893	325.893	0.000	1144.340	1078.110	-188.877
300	83.532	326.409	325.896	0.154	1144.321	1077.698	-187.640
400	91.952	351.721	329.288	8.973	1143.255	1055.645	-137.850
500	96.895	372.831	335.945	18.443	1141.850	1033.897	-108.008
600	99.945	390.799	343.627	28.303	1140.079	1012.469	-88.142
700	101.929	406.376	351.505	38.410	1137.976	991.362	-73.975
800	103.281	420.089	359.238	48.681	1135.630	970.574	-63.371
900	104.239	432.320	366.690	59.067	1132.973	950.098	-55.141
1000	104.940	443.349	373.815	69.534	1129.831	929.940	-48.574
1100	105.467	453.383	380.598	80.063	1126.027	910.131	-43.218
1200	105.874	462.584	387.052	90.638	1109.615	891.053	-38.786
1300	106.193	471.077	393.193	101.249	1106.688	872.957	-35.075
1400	106.449	478.962	399.041	111.889	1103.471	855.098	-31.903
1500	106.656	486.319	404.618	122.551	1099.935	837.478	-29.163
1600	106.826	493.212	409.941	133.233	1096.042	820.106	-26.773
1700	106.968	499.697	415.032	143.930	1091.756	802.985	-24.672
1800	107.088	505.819	419.908	154.640	1087.043	786.141	-22.813
1900	107.189	511.615	424.583	165.361	1081.862	769.557	-21.156
2000	107.276	517.119	429.073	176.092	1032.119	754.629	-19.709
2200	107.416	527.358	437.551	197.576	1015.147	727.695	-17.277
2400	107.522	536.715	445.430	219.084	998.068	702.321	-15.285
2600	107.605	545.331	452.788	240.612	980.882	678.369	-13.628
2800	107.672	553.313	459.687	262.154	963.599	655.747	-12.233
3000	107.725	560.748	466.179	283.708	946.217	634.364	-11.045
3200	107.769	567.707	472.310	305.272	928.744	614.142	-10.025
3400	107.805	574.246	478.115	326.844	911.178	595.019	-9.141
3600	107.836	580.413	483.629	348.423	893.526	576.931	-8.371
3800	107.861	586.248	488.878	370.007	-347.810	616.945	-8.480
4000	107.883	591.784	493.885	391.596	-358.724	668.008	-8.723
4500	107.926	604.502	505.483	445.585	-389.063	798.109	-9.264
5000	107.957	615.883	515.965	499.592	-423.200	931.820	-9.734
6000	107.997	635.583	534.309	607.643	-499.900	1209.884	-10.533

**Table B.13.** Thermochemical properties of  $\text{Ti}_3\text{C}_3$  at 1 bar.

$T$ (K)	$C_p^\circ$	$S^\circ$	$-[G^\circ - H^\circ(298.15 \text{ K})]/T$	$H^\circ - H^\circ(298.15 \text{ K})$	$\Delta_f H^\circ$	$\Delta_f G^\circ$	$\log K_f$
	J K <sup>-1</sup> mol <sup>-1</sup>			kJ mol <sup>-1</sup>			
100	47.450	261.284	408.364	-14.708	1171.092	1147.727	-Infinity
200	76.035	303.138	345.648	-8.502	1170.569	1124.527	-293.691
298.15	95.415	337.469	337.469	0.000	1170.020	1102.050	-193.071
300	95.690	338.060	337.470	0.177	1170.008	1101.627	-191.807
400	107.207	367.327	341.382	10.378	1169.301	1078.933	-140.891
500	114.298	392.087	349.113	21.487	1168.209	1056.459	-110.365
600	118.924	413.377	358.092	33.171	1166.684	1034.247	-90.037
700	122.083	431.974	367.347	45.239	1164.769	1012.321	-75.539
800	124.320	448.441	376.473	57.574	1162.566	990.689	-64.684
900	125.954	463.193	385.304	70.100	1160.014	969.352	-56.259
1000	127.179	476.539	393.771	82.768	1156.950	948.326	-49.535
1100	128.117	488.714	401.857	95.543	1153.198	927.641	-44.049
1200	128.851	499.902	409.567	108.402	1136.819	907.683	-39.510
1300	129.435	510.246	416.918	121.326	1133.906	888.705	-35.708
1400	129.906	519.863	423.933	134.302	1130.685	869.963	-32.458
1500	130.291	528.845	430.631	147.321	1127.132	851.463	-29.650
1600	130.610	537.270	437.035	160.376	1123.207	833.210	-27.201
1700	130.877	545.202	443.167	173.459	1118.875	815.211	-25.048
1800	131.103	552.694	449.046	186.567	1114.103	797.494	-23.142
1900	131.295	559.792	454.689	199.696	1108.851	780.039	-21.444
2000	131.460	566.536	460.114	212.843	1059.025	764.243	-19.960
2200	131.727	579.087	470.369	239.180	1041.850	735.590	-17.465
2400	131.932	590.565	479.913	265.565	1024.525	708.517	-15.420
2600	132.092	601.139	488.837	291.985	1007.046	682.888	-13.719
2800	132.220	610.939	497.212	318.435	989.429	658.617	-12.286
3000	132.323	620.071	505.102	344.907	971.669	635.606	-11.067
3200	132.408	628.620	512.558	371.398	953.775	613.781	-10.019
3400	132.479	636.655	519.624	397.905	935.747	593.085	-9.111
3600	132.538	644.234	526.338	424.424	917.590	573.452	-8.320
3800	132.588	651.406	532.734	450.955	-324.291	611.953	-8.412
4000	132.631	658.212	538.838	477.494	-335.792	661.528	-8.639
4500	132.715	673.850	552.989	543.876	-367.777	788.043	-9.147
5000	132.775	687.845	565.786	610.294	-403.815	918.380	-9.594
6000	132.853	712.076	588.209	743.200	-485.082	1190.292	-10.362

**Table B.14.** Thermochemical properties of  $\text{Ti}_3\text{C}_4$  at 1 bar.

$T$ (K)	$C_p^\circ$	$S^\circ$	$-[G^\circ - H^\circ(298.15 \text{ K})]/T$	$H^\circ - H^\circ(298.15 \text{ K})$	$\Delta_f H^\circ$	$\Delta_f G^\circ$	$\log K_f$
	J K <sup>-1</sup> mol <sup>-1</sup>			kJ mol <sup>-1</sup>			
100	49.256	261.892	421.362	-15.947	1218.524	1195.194	-Infinity
200	82.370	306.123	352.983	-9.372	1218.044	1172.021	-306.095
298.15	106.529	343.928	343.928	0.000	1217.700	1149.516	-201.386
300	106.879	344.589	343.929	0.198	1217.693	1149.091	-200.071
400	121.810	377.573	348.325	11.699	1217.263	1126.282	-147.074
500	131.338	405.871	357.075	24.398	1216.435	1103.624	-115.293
600	137.719	430.434	367.301	37.880	1215.130	1081.178	-94.123
700	142.154	452.031	377.894	51.896	1213.390	1058.986	-79.021
800	145.332	471.244	388.384	66.288	1211.323	1037.065	-67.712
900	147.672	488.515	398.566	80.954	1208.876	1015.423	-58.932
1000	149.436	504.180	408.357	95.823	1205.890	994.082	-51.925
1100	150.794	518.499	417.728	110.848	1202.194	973.076	-46.207
1200	151.858	531.676	426.683	125.992	1185.849	952.791	-41.473
1300	152.707	543.874	435.234	141.232	1182.953	933.486	-37.507
1400	153.393	555.224	443.403	156.549	1179.733	914.418	-34.117
1500	153.956	565.834	451.216	171.927	1176.165	895.590	-31.187
1600	154.422	575.792	458.694	187.357	1172.210	877.010	-28.631
1700	154.812	585.172	465.860	202.830	1167.836	858.688	-26.384
1800	155.142	594.036	472.737	218.338	1163.007	840.650	-24.395
1900	155.424	602.438	479.345	233.877	1157.686	822.876	-22.622
2000	155.666	610.422	485.701	249.443	1107.780	806.768	-21.070
2200	156.057	625.287	497.725	280.637	1090.406	777.502	-18.460
2400	156.358	638.889	508.930	311.901	1072.837	749.831	-16.319
2600	156.593	651.422	519.415	343.218	1055.070	723.632	-14.538
2800	156.781	663.042	529.264	374.577	1037.120	698.813	-13.036
3000	156.933	673.871	538.548	405.970	1018.985	675.281	-11.757
3200	157.057	684.010	547.326	437.390	1000.672	652.960	-10.658
3400	157.161	693.541	555.649	468.833	982.183	631.796	-9.706
3600	157.248	702.533	563.562	500.295	963.524	611.721	-8.876
3800	157.322	711.042	571.101	531.774	-278.901	649.815	-8.932
4000	157.385	719.119	578.303	563.266	-290.986	699.006	-9.128
4500	157.508	737.676	595.000	642.043	-324.615	824.703	-9.573
5000	157.597	754.287	610.112	720.873	-362.553	954.417	-9.971
6000	157.712	783.051	636.611	878.638	-448.383	1225.689	-10.670

**Table B.15.** Thermochemical properties of Ti<sub>4</sub>C at 1 bar.

$T$ (K)	$C_p^\circ$	$S^\circ$	$-[G^\circ - H^\circ(298.15 \text{ K})]/T$	$H^\circ - H^\circ(298.15 \text{ K})$	$\Delta_f H^\circ$	$\Delta_f G^\circ$	$\log K_f$
	J K <sup>-1</sup> mol <sup>-1</sup>			kJ mol <sup>-1</sup>			
100	56.425	272.031	426.841	-15.481	1433.256	1409.453	-Infinity
200	80.219	319.392	361.942	-8.510	1432.233	1385.953	-Infinity
298.15	91.748	353.859	353.859	0.000	1430.670	1363.562	-238.886
300	91.898	354.427	353.860	0.170	1430.636	1363.144	-237.340
400	97.833	381.785	357.550	9.694	1428.685	1340.933	-175.104
500	101.110	404.016	364.690	19.663	1426.364	1319.255	-137.819
600	103.068	422.651	372.841	29.886	1423.709	1298.077	-113.005
700	104.318	438.650	381.126	40.267	1420.765	1277.369	-95.317
800	105.159	452.648	389.211	50.750	1417.627	1257.094	-82.078
900	105.750	465.078	396.961	61.305	1414.183	1237.231	-71.806
1000	106.181	476.251	404.342	71.909	1410.180	1217.778	-63.609
1100	106.503	486.393	411.347	82.551	1405.368	1198.765	-56.923
1200	106.751	495.678	417.993	93.222	1383.808	1180.701	-51.394
1300	106.945	504.236	424.302	103.914	1380.281	1163.917	-46.766
1400	107.100	512.172	430.298	114.623	1376.414	1147.419	-42.810
1500	107.225	519.571	436.006	125.347	1372.164	1131.209	-39.391
1600	107.328	526.499	441.448	136.082	1367.474	1115.293	-36.410
1700	107.414	533.013	446.644	146.827	1362.295	1099.684	-33.789
1800	107.486	539.159	451.615	157.579	1356.578	1084.407	-31.468
1900	107.547	544.976	456.377	168.338	1350.266	1069.448	-29.401
2000	107.600	550.497	460.946	179.102	1284.563	1056.663	-27.597
2200	107.684	560.764	469.561	200.646	1263.259	1034.899	-24.571
2400	107.748	570.142	477.557	222.203	1241.905	1015.091	-22.092
2600	107.798	578.775	485.016	243.773	1220.498	997.054	-20.031
2800	107.838	586.770	492.002	265.351	1199.046	980.668	-18.294
3000	107.870	594.216	498.571	286.936	1177.543	965.818	-16.816
3200	107.896	601.184	504.769	308.527	1155.998	952.408	-15.546
3400	107.918	607.730	510.635	330.123	1134.405	940.347	-14.446
3600	107.937	613.903	516.202	351.723	1112.772	929.557	-13.487
3800	107.952	619.743	521.499	373.326	-540.365	996.127	-13.692
4000	107.965	625.284	526.551	394.933	-552.867	1077.321	-14.068
4500	107.991	638.011	538.243	448.958	-587.881	1283.120	-14.894
5000	108.009	649.398	548.799	502.995	-627.516	1493.099	-15.598
6000	108.033	669.105	567.257	611.089	-716.720	1925.446	-16.762

**Table B.16.** Thermochemical properties of  $\text{Ti}_4\text{C}_2$  at 1 bar.

$T$ (K)	$C_p^\circ$	$S^\circ$	$-[G^\circ - H^\circ(298.15 \text{ K})]/T$	$H^\circ - H^\circ(298.15 \text{ K})$	$\Delta_f H^\circ$	$\Delta_f G^\circ$	$\log K_f$
	J K <sup>-1</sup> mol <sup>-1</sup>			kJ mol <sup>-1</sup>			
100	53.151	263.864	426.574	-16.271	1343.127	1320.235	-Infinity
200	84.348	310.990	357.445	-9.291	1341.787	1297.803	-Infinity
298.15	103.078	348.538	348.538	0.000	1340.340	1276.529	-223.638
300	103.337	349.177	348.540	0.191	1340.311	1276.132	-222.190
400	113.847	380.512	352.740	11.109	1338.731	1254.973	-163.880
500	119.854	406.638	360.982	22.828	1336.834	1234.245	-128.938
600	123.503	428.853	370.490	35.018	1334.568	1213.935	-105.680
700	125.853	448.093	380.233	47.502	1331.954	1194.032	-89.098
800	127.443	465.020	389.795	60.180	1329.090	1174.520	-76.687
900	128.565	480.109	399.007	72.992	1325.868	1155.387	-67.056
1000	129.383	493.708	407.808	85.900	1322.046	1136.644	-59.371
1100	129.998	506.078	416.188	98.879	1317.377	1118.323	-53.104
1200	130.470	517.418	424.158	111.912	1295.928	1100.940	-47.922
1300	130.841	527.883	431.739	124.987	1292.485	1084.830	-43.588
1400	131.137	537.597	438.958	138.095	1288.677	1068.999	-39.884
1500	131.377	546.659	445.839	151.230	1284.464	1053.453	-36.684
1600	131.575	555.150	452.408	164.387	1279.791	1038.201	-33.893
1700	131.739	563.137	458.689	177.562	1274.610	1023.253	-31.440
1800	131.877	570.676	464.703	190.752	1268.874	1008.641	-29.269
1900	131.994	577.815	470.471	203.954	1262.526	994.343	-27.336
2000	132.094	584.592	476.008	217.167	1196.773	982.225	-25.653
2200	132.256	597.198	486.461	243.621	1175.323	961.804	-22.836
2400	132.379	608.719	496.176	270.103	1153.771	943.351	-20.531
2600	132.475	619.326	505.247	296.606	1132.112	926.691	-18.617
2800	132.551	629.153	513.750	323.127	1110.361	911.704	-17.008
3000	132.613	638.307	521.753	349.661	1088.511	898.272	-15.640
3200	132.663	646.873	529.309	376.206	1066.572	886.306	-14.467
3400	132.705	654.922	536.463	402.761	1044.541	875.717	-13.453
3600	132.740	662.513	543.256	429.324	1022.426	866.427	-12.571
3800	132.770	669.696	549.724	455.892	-631.238	934.522	-12.846
4000	132.796	676.511	555.894	482.467	-644.309	1017.271	-13.284
4500	132.845	692.166	570.183	548.922	-680.932	1227.086	-14.243
5000	132.880	706.174	583.094	615.398	-722.440	1441.280	-15.057
6000	132.927	730.421	605.689	748.393	-816.165	1882.653	-16.390

**Table B.17.** Thermochemical properties of  $\text{Ti}_4\text{C}_3$  at 1 bar.

$T$ (K)	$C_p^\circ$	$S^\circ$	$-[G^\circ - H^\circ(298.15 \text{ K})]/T$	$H^\circ - H^\circ(298.15 \text{ K})$	$\Delta_f H^\circ$	$\Delta_f G^\circ$	$\log K_f$
	J K <sup>-1</sup> mol <sup>-1</sup>			kJ mol <sup>-1</sup>			
100	53.997	272.972	448.402	-17.543	1307.526	1283.819	-Infinity
200	90.784	322.103	373.308	-10.241	1306.182	1260.592	-Infinity
298.15	115.657	363.434	363.434	0.000	1305.020	1238.479	-216.972
300	116.011	364.151	363.438	0.214	1304.998	1238.064	-215.562
400	130.568	399.737	368.190	12.619	1303.882	1215.920	-158.780
500	139.042	429.883	377.593	26.145	1302.466	1194.085	-124.743
600	144.239	455.747	388.517	40.338	1300.625	1172.575	-102.080
700	147.605	478.267	399.764	54.952	1298.368	1151.409	-85.917
800	149.892	498.148	410.843	69.844	1295.797	1130.586	-73.818
900	151.508	515.913	421.549	84.928	1292.812	1110.107	-64.428
1000	152.689	531.951	431.800	100.151	1289.182	1089.994	-56.934
1100	153.577	546.557	441.579	115.476	1284.665	1070.287	-50.823
1200	154.261	559.960	450.893	130.880	1263.336	1051.505	-45.770
1300	154.797	572.338	459.766	146.344	1259.983	1033.986	-41.545
1400	155.226	583.833	468.221	161.857	1256.240	1016.743	-37.934
1500	155.574	594.562	476.290	177.408	1252.069	999.781	-34.815
1600	155.861	604.619	484.000	192.990	1247.416	983.107	-32.095
1700	156.099	614.082	491.377	208.599	1242.237	966.738	-29.704
1800	156.299	623.016	498.444	224.230	1236.485	950.708	-27.588
1900	156.469	631.477	505.225	239.879	1230.105	934.993	-25.704
2000	156.614	639.512	511.740	255.543	1164.304	921.458	-24.066
2200	156.848	654.460	524.045	286.912	1142.713	898.214	-21.326
2400	157.027	668.125	535.491	318.321	1120.965	876.950	-19.086
2600	157.167	680.708	546.184	349.762	1099.059	857.501	-17.227
2800	157.277	692.367	556.214	381.228	1077.011	839.747	-15.665
3000	157.367	703.228	565.657	412.713	1054.816	823.573	-14.339
3200	157.440	713.394	574.577	444.215	1032.486	808.883	-13.203
3400	157.501	722.947	583.026	475.731	1010.019	795.598	-12.223
3600	157.552	731.957	591.052	507.257	987.422	783.637	-11.370
3800	157.595	740.482	598.694	538.793	-666.766	849.096	-11.671
4000	157.632	748.572	605.988	570.337	-680.405	929.231	-12.134
4500	157.704	767.155	622.883	649.225	-718.634	1132.648	-13.147
5000	157.755	783.785	638.156	728.143	-762.012	1340.638	-14.005
6000	157.822	812.573	664.900	886.040	-860.257	1770.197	-15.411

**Table B.18.** Thermochemical properties of  $\text{Ti}_4\text{C}_4$  at 1 bar.

$T$ (K)	$C_p^\circ$	$S^\circ$	$-[G^\circ - H^\circ(298.15 \text{ K})]/T$	$H^\circ - H^\circ(298.15 \text{ K})$	$\Delta_f H^\circ$	$\Delta_f G^\circ$	$\log K_f$
			$\text{J K}^{-1} \text{ mol}^{-1}$	$\text{kJ mol}^{-1}$			
100	45.073	248.232	421.762	-17.353	1175.377	1154.239	-Infinity
200	89.948	293.078	346.183	-10.621	1173.137	1133.969	-296.156
298.15	123.665	335.836	335.836	0.000	1171.690	1115.089	-195.355
300	124.152	336.603	335.840	0.229	1171.667	1114.736	-194.089
400	144.319	375.370	340.988	13.753	1170.647	1095.917	-143.109
500	156.171	408.981	351.305	28.838	1169.464	1077.366	-112.549
600	163.478	438.170	363.405	44.859	1167.873	1059.089	-92.200
700	168.225	463.769	375.953	61.471	1165.841	1041.114	-77.687
800	171.455	486.471	388.376	78.476	1163.462	1023.453	-66.823
900	173.742	506.818	400.425	95.754	1160.636	1006.115	-58.392
1000	175.415	525.227	412.000	113.227	1157.133	989.126	-51.666
1100	176.674	542.019	423.068	130.846	1152.716	972.533	-46.181
1200	177.643	557.445	433.632	148.576	1131.462	956.856	-41.650
1300	178.404	571.705	443.711	166.392	1128.162	942.438	-37.867
1400	179.013	584.958	453.332	184.276	1124.450	928.290	-34.634
1500	179.507	597.335	462.525	202.215	1120.293	914.423	-31.842
1600	179.914	608.941	471.317	220.198	1115.636	900.844	-29.409
1700	180.252	619.866	479.737	238.219	1110.437	887.570	-27.271
1800	180.536	630.184	487.811	256.271	1104.649	874.638	-25.381
1900	180.778	639.958	495.564	274.349	1098.219	862.022	-23.698
2000	180.984	649.242	503.017	292.449	1032.355	851.591	-22.241
2200	181.317	666.520	517.109	328.705	1010.595	834.560	-19.815
2400	181.571	682.318	530.227	365.019	988.629	819.530	-17.836
2600	181.769	696.870	542.493	401.379	966.457	806.333	-16.199
2800	181.927	710.355	554.008	437.773	944.095	794.858	-14.828
3000	182.054	722.920	564.855	474.196	921.542	784.982	-13.667
3200	182.158	734.680	575.104	510.642	898.808	776.619	-12.677
3400	182.245	745.734	584.820	547.106	875.892	769.683	-11.825
3600	182.317	756.160	594.053	583.587	852.805	764.101	-11.087
3800	182.379	766.025	602.846	620.081	-801.917	835.970	-11.491
4000	182.431	775.388	611.241	656.587	-816.131	922.541	-12.047
4500	182.533	796.896	630.698	747.890	-855.984	1142.178	-13.258
5000	182.606	816.144	648.297	839.237	-901.245	1366.595	-14.276
6000	182.701	849.469	679.133	1022.017	-1004.029	1829.597	-15.928

**Table B.19.** Thermochemical properties of  $\text{Ti}_3\text{C}_8$  at 1 bar.

$T$ (K)	$C_p^\circ$	$S^\circ$	$-[G^\circ - H^\circ(298.15 \text{ K})]/T$	$H^\circ - H^\circ(298.15 \text{ K})$	$\Delta_f H^\circ$	$\Delta_f G^\circ$	$\log K_f$
		$\text{J K}^{-1} \text{ mol}^{-1}$		$\text{kJ mol}^{-1}$			
100	99.795	320.515	610.135	-28.962	799.173	770.361	-Infinity
200	149.339	405.885	487.680	-16.359	803.417	739.907	-193.240
298.15	181.112	472.012	472.012	0.000	807.400	707.873	-124.014
300	181.569	473.135	472.015	0.336	807.467	707.253	-123.141
400	200.983	528.284	479.404	19.552	810.660	673.336	-87.927
500	213.659	574.614	493.938	40.338	812.615	638.757	-66.729
600	222.621	614.430	510.780	62.190	813.368	603.898	-52.573
700	229.250	649.293	528.129	84.815	813.145	568.994	-42.458
800	234.282	680.269	545.246	108.018	812.205	534.170	-34.877
900	238.169	708.116	561.822	131.665	810.599	499.500	-28.990
1000	241.217	733.390	577.734	155.656	808.243	465.053	-24.291
1100	243.639	756.514	592.951	179.919	805.009	430.886	-20.461
1200	245.588	777.814	607.481	204.400	788.997	397.402	-17.298
1300	247.174	797.550	621.352	229.058	786.323	364.876	-14.661
1400	248.479	815.929	634.601	253.859	783.227	332.573	-12.408
1500	249.563	833.122	647.269	278.779	779.705	300.506	-10.464
1600	250.473	849.269	659.395	303.799	775.720	268.685	-8.771
1700	251.243	864.487	671.015	328.903	771.249	237.124	-7.286
1800	251.899	878.877	682.168	354.077	766.258	205.860	-5.974
1900	252.462	892.521	692.883	379.313	760.718	174.866	-4.807
2000	252.950	905.492	703.191	404.601	710.538	145.554	-3.801
2200	253.744	929.656	722.698	455.308	692.453	89.921	-2.135
2400	254.359	951.776	740.878	506.155	673.975	35.957	-0.783
2600	254.844	972.169	757.896	557.111	655.107	-16.450	0.330
2800	255.233	991.083	773.885	608.154	635.873	-67.378	1.257
3000	255.549	1008.715	788.959	659.267	616.274	-116.926	2.036
3200	255.809	1025.227	803.215	710.438	596.320	-165.168	2.696
3400	256.026	1040.753	816.737	761.656	576.018	-212.139	3.259
3600	256.209	1055.402	829.592	812.915	555.376	-257.907	3.742
3800	256.364	1069.268	841.845	864.207	-689.204	-245.391	3.373
4000	256.497	1082.430	853.548	915.527	-703.609	-221.661	2.895
4500	256.757	1112.677	880.693	1043.930	-743.768	-159.097	1.847
5000	256.944	1139.757	905.268	1172.444	-789.270	-91.710	0.958
6000	257.188	1186.659	948.377	1429.692	-893.305	57.311	-0.499

**Table B.20.** Thermochemical properties of  $\text{Ti}_4\text{C}_8$  at 1 bar.

$T$ (K)	$C_p^\circ$	$S^\circ$	$-[G^\circ - H^\circ(298.15 \text{ K})]/T$	$H^\circ - H^\circ(298.15 \text{ K})$	$\Delta_f H^\circ$	$\Delta_f G^\circ$	$\log K_f$
			$\text{J K}^{-1} \text{ mol}^{-1}$	$\text{kJ mol}^{-1}$			
100	92.081	304.405	616.355	-31.195	544.209	517.834	-270.484
200	163.550	391.968	482.688	-18.144	546.984	490.503	-128.104
298.15	201.652	465.272	465.272	0.000	550.400	462.053	-80.948
300	202.157	466.522	465.275	0.374	550.458	461.503	-80.353
400	223.064	527.842	473.495	21.739	553.187	431.409	-56.335
500	236.467	579.185	489.639	44.773	554.649	400.772	-41.868
600	245.966	623.213	508.321	68.935	554.887	369.957	-32.207
700	253.000	661.708	527.541	93.917	554.133	339.185	-25.310
800	258.327	695.878	546.487	119.513	552.661	308.570	-20.147
900	262.427	726.572	564.821	145.576	550.480	278.176	-16.145
1000	265.628	754.412	582.409	172.003	547.439	248.075	-12.958
1100	268.162	779.870	599.220	198.715	543.339	218.331	-10.367
1200	270.193	803.309	615.264	225.654	522.290	189.476	-8.248
1300	271.841	825.018	630.574	252.777	519.101	161.869	-6.504
1400	273.193	845.228	645.193	280.049	515.417	134.527	-5.019
1500	274.314	864.128	659.165	307.444	511.220	107.468	-3.742
1600	275.253	881.875	672.536	334.942	506.458	80.700	-2.635
1700	276.045	898.597	685.346	362.527	501.095	54.245	-1.667
1800	276.720	914.406	697.637	390.184	495.084	28.146	-0.817
1900	277.299	929.393	709.443	417.905	488.381	2.374	-0.065
2000	277.799	943.639	720.800	445.679	422.195	-21.195	0.554
2200	278.613	970.174	742.283	501.360	399.636	-64.454	1.530
2400	279.242	994.461	762.300	557.186	376.690	-105.636	2.299
2600	279.737	1016.847	781.030	613.123	353.355	-144.886	2.911
2800	280.133	1037.607	798.625	669.149	329.657	-182.315	3.401
3000	280.456	1056.958	815.209	725.246	305.594	-218.044	3.796
3200	280.721	1075.079	830.891	781.402	281.178	-252.169	4.116
3400	280.942	1092.116	845.761	837.606	256.414	-284.744	4.374
3600	281.128	1108.190	859.898	893.852	231.312	-315.852	4.583
3800	281.286	1123.405	873.371	950.131	-1425.593	-269.394	3.703
4000	281.421	1137.846	886.236	1006.440	-1442.152	-208.112	2.718
4500	281.685	1171.031	916.072	1147.314	-1488.590	-51.178	0.594
5000	281.875	1200.740	943.080	1288.301	-1541.459	111.341	-1.163
6000	282.123	1252.190	990.440	1570.500	-1662.512	452.980	-3.943

**Table B.21.** Thermochemical properties of  $\text{Ti}_6\text{C}_{13}$  at 1 bar.

$T$ (K)	$C_p^\circ$	$S^\circ$	$-[G^\circ - H^\circ(298.15 \text{ K})]/T$	$H^\circ - H^\circ(298.15 \text{ K})$	$\Delta_f H^\circ$	$\Delta_f G^\circ$	$\log K_f$
	J K <sup>-1</sup> mol <sup>-1</sup>			kJ mol <sup>-1</sup>			
100	142.231	347.170	842.360	-49.519	461.748	433.225	-226.289
200	259.543	485.256	629.836	-28.916	466.611	403.045	-105.263
298.15	322.656	602.049	602.049	0.000	472.770	370.542	-64.916
300	323.511	604.049	602.056	0.598	472.878	369.903	-64.405
400	359.039	702.485	615.235	34.900	478.203	334.732	-43.711
500	381.637	785.250	641.186	72.032	481.651	298.431	-31.176
600	397.410	856.351	671.261	111.054	483.209	261.615	-22.775
700	408.963	918.565	702.239	151.428	483.206	224.667	-16.764
800	417.658	973.805	732.797	192.806	482.061	187.795	-12.261
900	424.329	1023.433	762.380	234.948	479.802	151.127	-8.771
1000	429.531	1068.451	790.771	277.680	476.209	114.787	-5.996
1100	433.646	1109.618	817.913	320.876	470.993	78.889	-3.746
1200	436.944	1147.522	843.822	364.440	440.324	44.240	-1.926
1300	439.622	1182.628	868.550	408.302	436.419	11.389	-0.458
1400	441.819	1215.313	892.165	452.407	431.750	-21.132	0.788
1500	443.642	1245.880	914.739	496.712	426.293	-53.290	1.856
1600	445.168	1274.581	936.340	541.185	419.971	-85.064	2.777
1700	446.458	1301.627	957.040	585.798	412.730	-116.424	3.577
1800	447.556	1327.195	976.901	630.530	404.503	-147.291	4.274
1900	448.498	1351.435	995.981	675.363	395.221	-177.716	4.886
2000	449.312	1374.476	1014.334	720.285	296.704	-204.874	5.351
2200	450.639	1417.394	1049.055	810.346	264.349	-253.483	6.018
2400	451.664	1456.677	1081.410	900.641	231.363	-299.111	6.510
2600	452.471	1492.886	1111.687	991.118	197.747	-341.958	6.870
2800	453.118	1526.465	1140.130	1081.739	163.540	-382.177	7.129
3000	453.644	1557.766	1166.940	1172.478	128.743	-419.942	7.312
3200	454.077	1587.078	1192.293	1263.312	93.371	-455.391	7.433
3400	454.438	1614.636	1216.335	1354.225	57.435	-488.585	7.506
3600	454.742	1640.637	1239.191	1445.205	20.948	-519.653	7.540
3800	454.999	1665.247	1260.973	1536.240	-2463.285	-434.427	5.971
4000	455.220	1688.607	1281.776	1627.324	-2487.040	-327.032	4.271
4500	455.651	1742.286	1330.019	1855.200	-2554.171	-53.166	0.617
5000	455.961	1790.343	1373.691	2083.259	-2631.208	228.812	-2.390
6000	456.367	1873.569	1450.278	2539.746	-2809.021	817.061	-7.113

**Table B.22.** Thermochemical properties of  $\text{Ti}_7\text{C}_{13}$  at 1 bar.

$T$ (K)	$C_p^\circ$	$S^\circ$	$-[G^\circ - H^\circ(298.15 \text{ K})]/T$	$H^\circ - H^\circ(298.15 \text{ K})$	$\Delta_f H^\circ$	$\Delta_f G^\circ$	$\log K_f$
	J K <sup>-1</sup> mol <sup>-1</sup>			kJ mol <sup>-1</sup>			
100	163.124	367.228	904.358	-53.713	643.823	614.120	-320.777
200	280.673	520.499	675.099	-30.920	648.959	582.590	-152.154
298.15	342.862	645.457	645.457	0.000	654.770	548.771	-96.140
300	343.727	647.582	645.462	0.636	654.869	548.109	-95.432
400	380.433	751.979	659.449	37.012	659.655	511.755	-66.827
500	404.363	839.670	686.960	76.355	662.573	474.410	-49.560
600	421.084	915.007	718.839	117.701	663.630	436.652	-38.013
700	433.230	980.921	751.670	160.476	663.140	398.845	-29.762
800	442.280	1039.429	784.050	204.303	661.519	361.185	-23.582
900	449.160	1091.972	815.395	248.919	658.743	323.788	-18.792
1000	454.483	1139.615	845.472	294.143	654.521	286.783	-14.980
1100	458.667	1183.165	874.220	339.839	648.490	250.291	-11.885
1200	462.003	1223.249	901.658	385.909	612.832	215.250	-9.369
1300	464.699	1260.364	927.841	432.280	608.456	182.293	-7.324
1400	466.905	1294.909	952.841	478.895	603.238	149.705	-5.585
1500	468.729	1327.207	976.733	525.711	597.142	117.524	-4.092
1600	470.253	1357.529	999.596	572.693	590.074	85.768	-2.800
1700	471.537	1386.096	1021.498	619.816	581.970	54.480	-1.674
1800	472.629	1413.098	1042.511	667.057	572.749	23.742	-0.689
1900	473.565	1438.695	1062.695	714.400	562.329	-6.501	0.179
2000	474.372	1463.023	1082.108	761.829	447.827	-32.957	0.861
2200	475.686	1508.330	1118.828	856.904	411.038	-79.272	1.882
2400	476.699	1549.793	1153.038	952.211	373.617	-122.199	2.660
2600	477.496	1588.008	1185.048	1047.697	335.562	-161.982	3.254
2800	478.134	1623.442	1215.111	1143.326	296.916	-198.790	3.708
3000	478.652	1656.470	1243.447	1239.070	257.676	-232.830	4.054
3200	479.078	1687.396	1270.237	1334.909	217.862	-264.250	4.313
3400	479.433	1716.470	1295.639	1430.825	177.481	-293.140	4.503
3600	479.732	1743.901	1319.788	1526.806	136.548	-319.648	4.638
3800	479.986	1769.863	1342.799	1622.843	-2759.995	-210.571	2.894
4000	480.203	1794.505	1364.774	1718.926	-2785.894	-75.722	0.989
4500	480.626	1851.129	1415.729	1959.300	-2859.277	267.269	-3.102
5000	480.930	1901.818	1461.847	2199.854	-2943.659	619.141	-6.468
6000	481.328	1989.599	1542.712	2681.322	-3138.460	1349.504	-11.748

**Table B.23.** Thermochemical properties of  $\text{Ti}_8\text{C}_{12}$  at 1 bar.

$T$ (K)	$C_p^\circ$	$S^\circ$	$-[G^\circ - H^\circ(298.15 \text{ K})]/T$	$H^\circ - H^\circ(298.15 \text{ K})$	$\Delta_f H^\circ$	$\Delta_f G^\circ$	$\log K_f$
	$\text{J K}^{-1} \text{ mol}^{-1}$			$\text{kJ mol}^{-1}$			
100	138.419	352.081	850.201	-49.812	-346.678	-374.135	195.424
200	260.531	488.293	635.548	-29.451	-345.565	-401.864	104.954
298.15	332.379	607.145	607.145	0.000	-342.910	-430.027	75.338
300	333.382	609.206	607.153	0.616	-342.862	-430.573	74.968
400	375.669	711.471	620.806	36.266	-340.392	-460.204	60.095
500	402.608	798.457	647.863	75.297	-339.201	-490.322	51.223
600	420.917	873.630	679.368	116.557	-339.477	-520.539	45.316
700	433.862	939.586	711.929	159.360	-341.054	-550.605	41.086
800	443.281	998.206	744.119	203.270	-343.596	-580.382	37.894
900	450.301	1050.877	775.327	247.995	-347.219	-609.782	35.390
1000	455.646	1098.642	805.307	293.335	-352.323	-638.697	33.361
1100	459.793	1142.301	833.986	339.146	-359.360	-667.005	31.673
1200	463.065	1182.481	861.376	385.326	-400.152	-693.644	30.193
1300	465.686	1219.678	887.525	431.799	-405.107	-717.905	28.845
1400	467.815	1254.292	912.500	478.509	-410.949	-741.747	27.674
1500	469.566	1286.652	936.377	525.412	-417.734	-765.140	26.644
1600	471.021	1317.025	959.228	572.475	-425.571	-788.056	25.727
1700	472.243	1345.637	981.125	619.671	-434.543	-810.455	24.902
1800	473.278	1372.678	1002.134	666.980	-444.742	-832.250	24.151
1900	474.162	1398.308	1022.316	714.385	-456.269	-853.491	23.464
2000	474.923	1422.665	1041.729	761.872	-586.706	-870.428	22.733
2200	476.156	1468.021	1078.453	857.049	-627.785	-896.830	21.293
2400	477.105	1509.522	1112.671	952.442	-669.444	-919.452	20.011
2600	477.849	1547.767	1144.689	1048.004	-711.686	-938.580	18.856
2800	478.443	1583.226	1174.762	1143.700	-754.470	-954.418	17.805
3000	478.925	1616.274	1203.107	1239.502	-797.804	-967.190	16.840
3200	479.321	1647.217	1229.907	1335.392	-841.666	-977.068	15.949
3400	479.650	1676.305	1255.319	1431.354	-886.052	-984.166	15.120
3600	479.926	1703.747	1279.476	1527.376	-930.946	-988.643	14.345
3800	480.161	1729.719	1302.495	1623.450	-4239.272	-838.283	11.523
4000	480.362	1754.370	1324.478	1719.567	-4266.743	-658.575	8.600
4500	480.753	1811.010	1375.452	1960.012	-4344.766	-203.065	2.357
5000	481.034	1861.712	1421.587	2200.623	-4434.619	261.881	-2.736
6000	481.401	1949.509	1502.479	2682.178	-4641.880	1220.138	-10.622

**Table B.24.** Thermochemical properties of  $\text{Ti}_9\text{C}_{15}$  at 1 bar.

$T$ (K)	$C_p^\circ$	$S^\circ$	$-[G^\circ - H^\circ(298.15 \text{ K})]/T$	$H^\circ - H^\circ(298.15 \text{ K})$	$\Delta_f H^\circ$	$\Delta_f G^\circ$	$\log K_f$
	$\text{J K}^{-1} \text{ mol}^{-1}$			$\text{kJ mol}^{-1}$			
100	187.713	387.111	1038.781	-65.167	37.229	7.381	-3.855
200	342.131	570.092	759.447	-37.871	42.382	-24.182	6.316
298.15	420.650	723.112	723.112	0.000	49.110	-58.278	10.210
300	421.709	725.719	723.119	0.780	49.227	-58.950	10.264
400	465.730	853.694	740.269	45.370	54.955	-95.922	12.526
500	493.570	960.889	773.969	93.460	58.486	-134.091	14.008
600	512.755	1052.735	812.960	143.865	59.796	-172.760	15.040
700	526.602	1132.925	853.064	195.903	59.247	-211.495	15.782
800	536.886	1203.994	892.573	249.137	57.341	-250.061	16.327
900	544.687	1267.743	930.776	303.270	54.030	-288.311	16.733
1000	550.713	1325.495	967.406	358.089	48.915	-326.093	17.033
1100	555.445	1378.250	1002.393	413.443	41.524	-363.250	17.249
1200	559.215	1426.780	1035.763	469.220	-3.919	-398.574	17.349
1300	562.260	1471.695	1067.590	525.336	-9.108	-431.256	17.328
1400	564.748	1513.485	1097.965	581.728	-15.347	-463.495	17.293
1500	566.805	1552.547	1126.982	638.347	-22.688	-495.250	17.246
1600	568.523	1589.209	1154.738	695.154	-31.251	-526.488	17.188
1700	569.971	1623.743	1181.320	752.119	-41.123	-557.160	17.119
1800	571.202	1656.379	1206.814	809.217	-52.407	-587.160	17.039
1900	572.256	1687.312	1231.297	866.429	-65.212	-616.552	16.950
2000	573.165	1716.708	1254.838	923.740	-211.814	-641.108	16.744
2200	574.643	1771.446	1299.353	1038.604	-257.822	-681.832	16.188
2400	575.784	1821.531	1340.811	1153.728	-304.566	-718.321	15.634
2600	576.680	1867.686	1379.588	1269.055	-352.046	-750.883	15.085
2800	577.398	1910.478	1415.999	1384.542	-400.212	-779.741	14.546
3000	577.981	1950.362	1450.309	1500.159	-449.067	-805.149	14.019
3200	578.460	1987.704	1482.741	1615.882	-498.587	-827.291	13.504
3400	578.859	2022.809	1513.488	1731.692	-548.764	-846.295	13.001
3600	579.195	2055.928	1542.712	1847.576	-599.578	-862.335	12.512
3800	579.480	2087.272	1570.556	1963.522	-4321.820	-704.159	9.679
4000	579.724	2117.021	1597.141	2079.520	-4353.164	-512.944	6.698
4500	580.200	2185.378	1658.778	2369.702	-4442.317	-27.795	0.323
5000	580.542	2246.567	1714.550	2660.086	-4545.173	468.162	-4.891
6000	580.989	2352.527	1812.317	3241.260	-4783.050	1492.566	-12.994

**Table B.25.** Thermochemical properties of  $\text{Ti}_{13}\text{C}_{22}$  at 1 bar.

$T$ (K)	$C_p^\circ$	$S^\circ$	$-[G^\circ - H^\circ(298.15 \text{ K})]/T$	$H^\circ - H^\circ(298.15 \text{ K})$		$\Delta_f H^\circ$	$\Delta_f G^\circ$	$\log K_f$
				kJ mol <sup>-1</sup>				
100	254.409	428.612	1353.172	-92.456	-619.327	-649.355	Infinity	
200	487.167	685.061	955.591	-54.106	-613.070	-681.331	177.942	
298.15	601.555	903.651	903.651	0.000	-604.170	-716.723	125.564	
300	603.058	907.380	903.663	1.115	-604.018	-717.430	124.913	
400	664.119	1090.172	928.172	64.800	-596.808	-756.403	98.774	
500	701.434	1242.769	976.259	133.255	-593.158	-796.790	83.238	
600	726.914	1373.128	1031.806	204.793	-593.061	-837.575	72.916	
700	745.413	1486.718	1088.854	278.505	-595.899	-878.132	65.526	
800	759.304	1587.270	1144.991	353.823	-600.868	-918.141	59.947	
900	769.969	1677.406	1199.228	430.360	-607.984	-957.410	55.566	
1000	778.297	1759.033	1251.191	507.842	-617.781	-995.736	52.011	
1100	784.897	1833.584	1300.797	586.066	-630.920	-1032.915	49.048	
1200	790.198	1902.160	1348.091	664.883	-699.060	-1067.221	46.454	
1300	794.506	1965.628	1393.183	744.178	-709.083	-1097.502	44.097	
1400	798.047	2024.681	1436.207	823.864	-720.644	-1126.949	42.046	
1500	800.988	2079.880	1477.297	903.874	-733.812	-1155.510	40.238	
1600	803.454	2131.690	1516.594	984.153	-748.758	-1183.155	38.625	
1700	805.538	2180.496	1554.226	1064.659	-765.605	-1209.822	37.173	
1800	807.315	2226.622	1590.312	1145.358	-784.499	-1235.365	35.849	
1900	808.841	2270.342	1624.962	1226.222	-805.597	-1259.883	34.636	
2000	810.160	2311.893	1658.280	1307.227	-1019.966	-1277.284	33.359	
2200	812.310	2389.266	1721.270	1469.592	-1091.657	-1299.575	30.855	
2400	813.973	2460.068	1779.928	1632.336	-1164.430	-1315.272	28.626	
2600	815.284	2525.318	1834.789	1795.376	-1238.284	-1324.859	26.616	
2800	816.335	2585.817	1886.299	1958.650	-1313.145	-1328.688	24.786	
3000	817.189	2642.206	1934.834	2122.115	-1389.016	-1327.153	23.107	
3200	817.893	2695.005	1980.713	2285.734	-1465.864	-1320.555	21.555	
3400	818.480	2744.640	2024.204	2449.483	-1543.673	-1309.080	20.111	
3600	818.974	2791.469	2065.542	2613.339	-1622.418	-1293.014	18.761	
3800	819.393	2835.790	2104.925	2777.286	-7004.351	-1025.009	14.089	
4000	819.753	2877.857	2142.529	2941.311	-7054.999	-708.999	9.258	
4500	820.454	2974.517	2229.707	3351.647	-7197.271	92.463	-1.073	
5000	820.959	3061.046	2308.590	3762.280	-7359.422	911.033	-9.517	
6000	821.619	3210.888	2446.863	4584.147	-7730.436	2599.098	-22.627	